
Einstein Fields: A Neural Perspective To Computational General Relativity

Sandeep S. Cranganore*¹

Andrei Bodnar*²

Arturs Berzins*¹

Johannes Brandstetter^{1,3}

*Equal contribution

¹LIT AI Lab, Institute for Machine Learning, JKU Linz, Austria

²University of Manchester, United Kingdom

³Emmi AI GmbH, Linz, Austria

{cranganore, berzins, brandstetter}@ml.jku.at
andrei.bodnar@student.manchester.ac.uk

Abstract

We introduce **Einstein Fields**, a neural representation that is designed to compress computationally intensive four-dimensional numerical relativity simulations into compact implicit neural network weights. By modeling the *metric*, which is the core tensor field of general relativity, **Einstein Fields** enable the derivation of physical quantities via automatic differentiation. However, unlike conventional neural fields (e.g., signed distance, occupancy, or radiance fields), **Einstein Fields** are *Neural Tensor Fields* with the key difference that when encoding the spacetime geometry of general relativity into neural field representations, dynamics emerge naturally as a byproduct. **Einstein Fields** show remarkable potential, including continuum modeling of four-dimensional spacetime, mesh-agnosticity, storage efficiency, derivative accuracy, and ease of use. We demonstrate these properties on several canonical test beds of general relativity and release an open-source JAX-based library, paving the way for more scalable and expressive approaches to numerical relativity. Code is made available at <https://github.com/AndreiB137/EinFields>.

1 Introduction

General relativity (GR) describes gravity as the curvature of spacetime, encoded in the metric tensor and governed by the Einstein field equations (EFEs), a system of coupled, nonlinear hyperbolic-elliptic PDEs. Exact solutions are often impossible for complicated astrophysical phenomena, so numerical relativity (NR) has become essential for accurate modeling of astrophysical events. Notable successes of NR include the high-precision modeling of black hole mergers [1–3], binary neutron star mergers [4], and neutron star–black hole systems [5]. NR was also central to the confirmation of gravitational waves (GWs) detected by LIGO and Virgo interferometers, leading to Nobel-prize-winning discoveries.

Recent progress in machine learning for scientific computing has shown the potential of neural PDE surrogates for spatiotemporal dynamics and forecasting algorithms [6–12]. On the other hand, neural fields (NeFs) [13–15] have emerged as an ubiquitous toolkit for implicit, compact, and continuous representations of high-dimensional explicit data, which includes images, shapes/geometries, and physical fields. This raises the question of whether such hybrid approaches can advance next-generation computational GR workflows, which are highly data-intensive, particularly when handling tensorial quantities and their derivatives defined on high-resolution grids with adaptively refined meshes.

39th Conference on Neural Information Processing Systems (NeurIPS 2025) Workshop: Einstein Fields: A Neural Perspective To Computational General Relativity.

Main contributions: We present EinFields (short for Einstein Fields) – compact, implicit neural network representations encoding four-dimensional (4D) spacetime geometries. Unlike existing neural field applications, EinFields *overfit* on the **metric tensor** – falling under the class of *neural tensor fields*, satisfying the properties enlisted in Eqs.((38), (44)). These are smooth, differentiable neural networks allowing (i) memory-efficient compression, (ii) discretization-free evaluation at arbitrary resolution, and, (iii) accurate automatic differentiation of differential geometric quantities. Our models achieve up to E-7 – E-9 relative agreement with ground truth metric, while being upto **five orders of magnitude** more accurate than finite-differencing methods on tensor derivative downstream tasks (for e.g. curvature tensors and scalars – see Appendix (B.3.6) for details) in FLOAT32. Our methodology reconstructs hallmark relativistic phenomena with high fidelity, including perihelion precession around Schwarzschild solutions, geodesics around Kerr blackholes, and gravitational wave signatures, such as an oscillating ring of particles and Weyl scalars reconstruction associated with outgoing GWs radiation field . We further provide a fully JAX-based [16] differential geometry library supporting tensor algebra, covariant derivatives, and geodesic equation solvers.

Together, these novel contributions demonstrate neural implicits as being a powerful paradigm for compact, accurate, and physically consistent modeling of NR simulations. The EinFields pipeline is detailed in Figure (1).

2 Background

We stress the three key properties that pertain to our work: (i) GR is a field theory of tensor-valued quantities whose arena is a Hausdorff manifold \mathcal{M} with a *Lorentzian* (pseudo-Riemannian) signature $(-, +, +, +)$, (ii) GR is intrinsically coordinate independent (diffeomorphism invariant – B.4.1), and (iii) gravitational physics is entirely encapsulated in the metric and its first two derivatives. We present a condensed version of the relevant concepts from differential geometry and general relativistic physics in Appendix F, while referring to Appendix B and the sources therein for an extremely detailed exposition.

Tensors. A rank (r, s) tensor T at a point $x \in \mathcal{M}$ is the multilinear map from r covectors and s vectors to a real number:

$$T : \underbrace{\mathcal{V}^* \times \dots \times \mathcal{V}^*}_{r-\text{copies}} \times \underbrace{\mathcal{V} \times \dots \times \mathcal{V}}_{s-\text{copies}} \rightarrow \mathbb{R}. \quad (1)$$

The r vectors and s covectors pair with the respective r covariant and s contravariant components of the tensor. As such, a tensor is an element that lives in a tensor product of *vector* and *dual spaces*, i.e., $T \in (\mathcal{V})^{\otimes r} \otimes (\mathcal{V}^*)^{\otimes s}$. A tensor in a particular choice of *basis* $\{e_{\alpha_n}\}_{1 \leq n \leq r} \in \mathcal{V}$ and $\{\vartheta^{\beta_n}\}_{1 \leq n \leq s} \in \mathcal{V}^*$ is given by $T = T^{\alpha_1 \alpha_2 \dots \alpha_r}_{\beta_1 \beta_2 \dots \beta_s} e_{\alpha_1} \otimes \dots \otimes e_{\alpha_r} \otimes \vartheta^{\beta_1} \otimes \dots \otimes \vartheta^{\beta_s}$, where $T^{\alpha_1 \alpha_2 \dots \alpha_r}_{\beta_1 \beta_2 \dots \beta_s} \equiv T(\vartheta^{\alpha_1}, \dots, \vartheta^{\alpha_r}, e_{\beta_s}, \dots, e_{\beta_s})$ are the *components* of the tensor in this particular basis and transforms as shown in Eq.(20). A **tensor field**, on the other hand, assigns to each point $x \in \mathcal{M}$ a multilinear map $T_x \in \mathcal{V}_x^{\otimes p} \otimes (\mathcal{V}^*)_x^{\otimes q}$, with components $T^{\alpha_1 \dots \alpha_r}_{\beta_1 \dots \beta_s}(x)$ that vary smoothly across the manifold.

General relativity formulated by Albert Einstein, extends Newtonian gravity with a geometric interpretation of gravity, where *mass and energy tell spacetime how to curve, and curved spacetime tells objects how to move* [17]. This is formalized by Einstein’s field equations (EFEs)

$$G_{\alpha\beta} + \Lambda g_{\alpha\beta} = 8\pi G T_{\alpha\beta}. \quad (2)$$

EFEs are a set of 10 coupled non-linear, tensor-valued, second-order partial differential equations and can be viewed as a tensorial generalization of the Newton-Poisson equation for gravity $\nabla^2 \Phi(r) = -4\pi G \rho(r)$ [17, 18]. In EFEs, $G_{\alpha\beta} = R_{\alpha\beta} - \frac{1}{2}Rg_{\alpha\beta}$ is the *Einstein tensor*, formed from the metric tensor field $g_{\alpha\beta}(x^\mu)$, which are solutions of the EFEs and tensorial generalization of the gravitational potential Φ . The Ricci curvature tensor $R_{\alpha\beta}$, and the Ricci curvature scalar R are related by second-derivatives $g_{\alpha\beta}$. Thus, the left-hand side of EFEs is entirely described by the metric and its derivatives, with Λ being the cosmological constant. The right-hand side depends on the stress-energy tensor $T_{\alpha\beta}$ describing the matter distribution, with G being Newton’s constant. The backbone of these highly complicated field equations is tensors, and the mathematical formalism is *differential geometry*.

Metric tensor and its derivatives. The metric is a rank $(0, 2)$ symmetric bilinear form $g : T_x \mathcal{M} \times T_x \mathcal{M} \rightarrow \mathbb{R}$ that generalizes the notion of an inner product on the tangent space $T_x \mathcal{M}$

of a differentiable manifold \mathcal{M} [19]. It enables the computation of angles between vector fields and a means to compute distances via the line element: $ds^2 = g_{\alpha\beta}(x^\mu) dx^\alpha dx^\beta$. In GR, the components $g_{\alpha\beta}$ in a particular coordinate system can be seen as a 4×4 symmetric matrix with *ten* independent components. The metric defines the causal structure and contains all geometric information of spacetime. Importantly, its partial derivatives ∂ yield the **Christoffel symbols** $\Gamma_{\alpha\beta\gamma}(x^\mu)$ (see Appendix (B.3.4) and Eq.(50)), which describe the notion of parallel transport (see Def.12) on the Lorentzian manifolds defining a *covariant derivative* operation $\nabla_\alpha = \partial_\alpha + \Gamma_\alpha$ (see Appendices (B.3.3) for details). The connection's derivatives (i.e., metric second-derivatives) yields the **Riemann curvature tensor** $R_{\alpha\beta\gamma}^\delta(x^\mu)$ (see Eqs.((56), (57))), which encodes tidal forces of gravity. The trace part of $R_{\alpha\beta\gamma}^\delta$ (index contraction w.r.t. metric: Tr_g – see Eq.(44)) is the **Ricci tensor** $R_{\alpha\beta}$, also a symmetric rank $(0, 2)$ tensor. Its subsequent contraction yields the **Ricci scalar** R (see Eqs.((60), (61))). This can be summarized schematically as follows (a more detailed pictorial version is available in Figure 8):

$$g_{\alpha\beta} \xrightarrow{\partial} \Gamma_{\alpha\beta}^\gamma \xrightarrow{\nabla} R_{\alpha\beta\gamma}^\delta \xrightarrow{\text{Tr}_g} R_{\alpha\beta} \xrightarrow{\text{Tr}_g} R. \quad (3)$$

Finite-difference (FD) methods with adaptive mesh refinement (AMR) [20] have long underpinned tensor calculus in NR, discretizing space and time with high-order stencils (Appendix D). An n -th order stencil yields truncation errors of $\mathcal{O}(h^n)$, where h is the grid spacing. Widely used fourth- or sixth-order schemes improve accuracy but incur larger communication costs due to broader stencil footprints. Yet, despite their effectiveness for smooth fields, FD schemes remain vulnerable to Gibbs-like oscillations [21] near discontinuities (e.g., neutron star surfaces or shocks), limiting convergence. In contrast, modern NR increasingly employs (*pseudo-*)*spectral methods* [22–24], which represent fields globally through polynomial bases such as Chebyshev or Legendre-Gauss-Lobatto (LGL) [25]. Spectral methods are ultimately bounded only by double-precision arithmetic, achieving orders-of-magnitude gains in both accuracy and efficiency—up to $1000\text{--}5000\times$ faster on CPUs than FD approaches on GPUs at comparable accuracy [26].

Neural fields. NeF also known as implicit neural representations (INR) or coordinate-based neural networks are multi-layer perceptrons (MLP) that are memory-efficient, implicit, continuous, infinitely differentiable ($\mathcal{C}^\infty(\mathbb{R})$) maps of discrete representations, capable of capturing high-fidelity detail across complex domains [27]. These properties have motivated their primary development and adoption in computer vision domains for representation, generation, and inversion tasks. Examples include scene reconstruction and rendering [28, 29], shape generation [13–15]. NeFs have proven to be highly versatile models for compressing large-scale data accompanied by ease of query at varying resolutions (see Appendix E).

3 EinFields

Consider the four-dimensional spacetime, a *Hausdorff* manifold equipped with a Lorentzian metric (\mathcal{M}, g) , corresponding to an exact or numerical solution of the EFEs¹: $G_{\alpha\beta} = 8\pi G T_{\alpha\beta}$. An **EinField** models the 10 independent components of the metric tensor field as a compact NeF, ultimately mapping the spacetime coordinates $x \equiv (x^0, x^1, x^2, x^3)$ to the symmetric rank $(0, 2)$ metric tensor field (see Definition 8):

$$\hat{g} : x \in \mathcal{M} \rightarrow g_{\alpha\beta}(x) \in \text{Sym}^2(T_x^* \mathcal{M}), \quad (4)$$

We deploy an MLP \hat{g}_θ with parameters θ , denoted \hat{g} (implicit representation of metric tensor field) for simplicity, to over-fit on the ground truth signal. Methodologically, this enables directly compressing the entire geometric information into storage-cheap NN weights, yielding continuous access (different from the training grid points) at high-resolution of the metric and its non-trivial tensor differentiation (for e.g. Lie derivative or covariant derivatives) information devoid of mesh (re)construction on curvilinear manifolds. This generalizes to an arbitrary rank (r, s) tensor field $T_{\beta_1 \dots \beta_s}^{\alpha_1 \dots \alpha_r}(x^\mu)$.

Thus, **EinFields** posit a neural alternative to address one or more of the challenges associated with traditional methods (typically utilizing higher-order finite differencing schemes) in NR by not relying on costly spatio-temporal discretizations. Our framework should be considered as a special case of *Neural Tensor Fields*.

¹From now on, we omit the cosmological constant term $\Lambda g_{\alpha\beta}$.

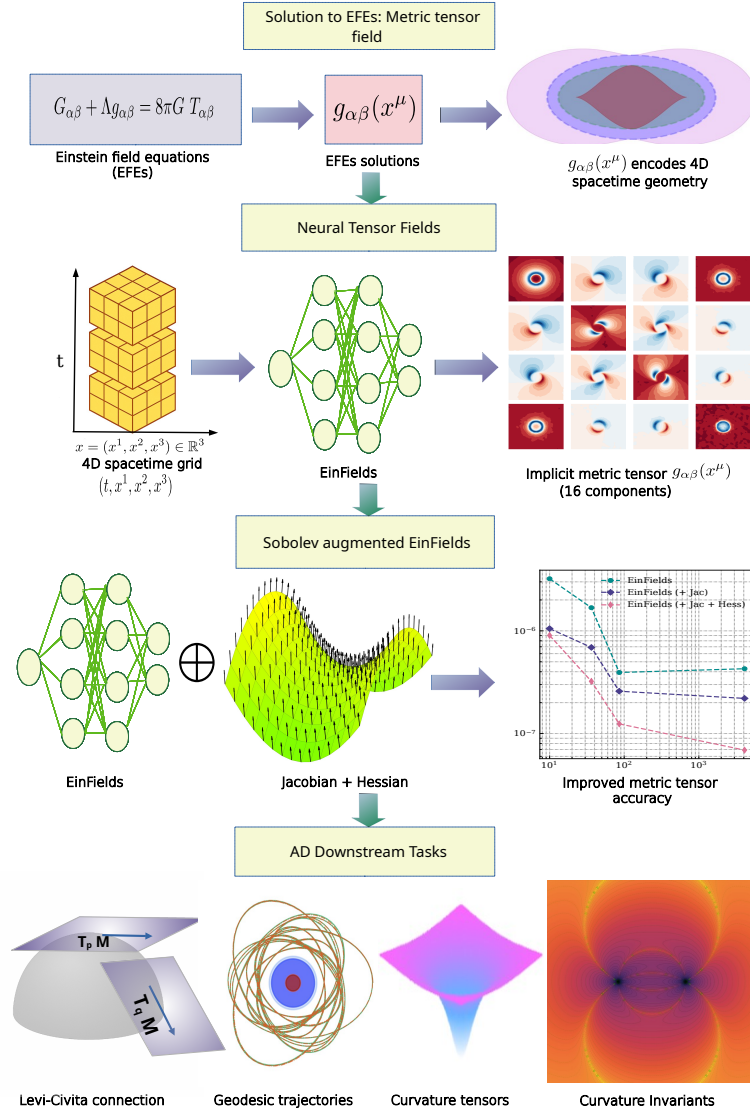


Figure 1: A conceptual overview of EinFields training and downstream pipeline. (i) **Premise:** The Einstein field equations (EFEs) in Equation (2) are highly non-linear partial differential equations defined on a 4D spacetime manifold, describing the geometric nature of gravitation. Their solutions define the metric tensor field $g_{\alpha\beta}(x^\mu)$, which encodes the full spacetime geometry and serves as a tensorial generalization of the gravitational potential. In this work, we parametrize $g_{\alpha\beta}(x^\mu)$ using a neural network. (ii) **Training:** The training is conducted on the metric tensor fields defined on a 4D spacetime grid. EinFields instead fit a continuous signal on these discrete representations, thus modeling 4D spacetime as a continuum, and returning the metric tensor field for a 4D spacetime query coordinate $p \equiv (t, x) \in \mathcal{M}$ at arbitrary resolution. (iii) **Sobolev supervision:** The reconstruction quality of the metric and its derivatives is improved by augmenting Sobolev losses, i.e., metric Jacobian (neighborhood structure) and Hessian (curvatures). (iv) **Validation and downstream tasks:** Sobolev improved EinFields' AD-based derivatives enable accurate point-wise retrieval of differential geometric quantities, such as the Levi-Civita connection (covariant derivative), geodesics, curvature tensors, and their invariants.

3.1 Distortion

We define the *distortion* as the algebraic deviation of the spacetime metric from flat space,

$$\Delta_{\alpha\beta} = g_{\alpha\beta} - \eta_{\alpha\beta}, \quad (5)$$

with the Minkowski background $\eta_{\alpha\beta}$ in that particular coordinate system. From a learning perspective, this decomposition acts as a preprocessing step that removes the offset (fixed background metric). Flat contributions, that may even dominate numerically (e.g., $g_{tt} \sim 1/r$, $g_{\theta\theta} \sim r^2$), are removed, leaving only the non-trivial geometric content: curvature, horizons, and rotation. Thus, the network focuses its representational capacity on meaningful deviations rather than redundantly relearning flat-space structure. This improves scaling, accelerates convergence, and emphasizes the dynamic, physically relevant features of the metric during training.

3.2 Retrieving physics via neural tensor field derivatives

Beyond the metric tensor itself, its first- and second-order derivatives are central to GR, as they govern geodesic motion, tidal forces, and curvature invariants. Accurate recovery of these quantities requires point-wise precise evaluation of Christoffel symbols and Riemann tensors, making their high-fidelity extraction from `EinFields` essential for reliable downstream analysis. This is facilitated by *Sobolev training* [30, 31], a loss formulation that explicitly incorporates derivatives (see Section G.2 for details). The supervision on the metric Jacobian $\partial_\mu g_{\alpha\beta}$ (40 independent components) and Hessian $\partial_\mu \partial_\nu g_{\alpha\beta}$ (100 independent components) rectifies irregularities in the metric field and its derivatives, yielding substantial accuracy gains and consequentially improving the precision of point-wise Christoffel symbols $\Gamma_{\alpha\beta}^\gamma(x^\mu)$ and Riemann tensors $R_{\alpha\beta\gamma}^\mu(x^\mu)$ queries by up to “two orders” of magnitude. This is given by the modified loss function:

$$\mathcal{L}_{\text{Sob}}^g(\theta) = \mathbb{E}_x \left[\lambda_0 \|g_{\alpha\beta}(x) - \hat{g}_{\alpha\beta}(x)\|^2 + \sum_{j=1}^2 \lambda_j \left\| \partial_x^{(j)} g_{\alpha\beta}(x) - \partial_x^{(j)} \hat{g}_{\alpha\beta}(x) \right\|^2 \right]. \quad (6)$$

We use the succinct notation $\partial_x^{(1)} \equiv \partial_\mu$ and $\partial_x^{(2)} \equiv \partial_\nu \partial_\mu$. The expected losses in Algorithm 1 $\mathcal{L}(\partial_x^{(j)} g, \partial_x^{(j)} \hat{g})$ are short-hand for $\mathbb{E}_x \left\| \partial_x^{(j)} g_{\alpha\beta}(x) - \partial_x^{(j)} \hat{g}_{\alpha\beta}(x) \right\|^2$. Instead of implementing higher-order FD methods, our framework enables access to exact higher-order tensor derivatives via automatic differentiation (AD) [32]. This is illustrated in the AD workflow for differential geometry in Figure 2.

Reconstructing dynamics. Free-fall trajectories follow the geodesic equation (Eq.(55)), which depends on Christoffel symbols $\Gamma(g, \partial g)$. These enter the covariant derivative $\nabla_\alpha = \partial_\alpha + \Gamma_\alpha$, governing parallel transport (Appendix B.3.3). In our AD-based workflow (Figure 2), `EinFields` reconstruct $\hat{\Gamma}(\hat{g}, \partial \hat{g})$ with Jacobian supervision, enabling $\nabla_\alpha = \partial_\alpha + \hat{\Gamma}_\alpha$ and, thus, accurate modeling of geodesics and direct evaluation of curvature objects, such as the Riemann tensor ($\nabla \Gamma$, see Appendix B.3.6).

Characterizing intrinsic geometry. Beyond dynamics, `EinFields` must reproduce the intrinsic geometry encoded in curvature tensors: Riemann $R_{\alpha\beta\gamma\delta}$, Weyl $C_{\alpha\beta\gamma\delta}$, Ricci $R_{\alpha\beta}$, scalar curvature R , and invariants such as the Kretschmann scalar (Figure 2). With Jacobian- and Hessian-level supervision, the learned fields achieve strong agreement with analytic solutions across the domain, except near singular regions where curvature diverges. Detailed comparisons of curvature tensors and invariants appear in Appendix B.3.6.

4 Experiments

The performance of `EinFields` is assessed along two axes: (i) *compression*, i.e., the reduction in storage requirements for implicit representations of NR tensor-valued grids with high-accuracy – including the metric (10 independent components) and higher-order derivatives (20–100 components) across millions of collocation points, and (ii) *reconstruction fidelity*, evaluated through key GR benchmarks: geodesic dynamics around compact objects (Section F) and curvature diagnostics such as the curvature scalars or invariants (see Appendix B.3.6). The evaluation criteria used are either

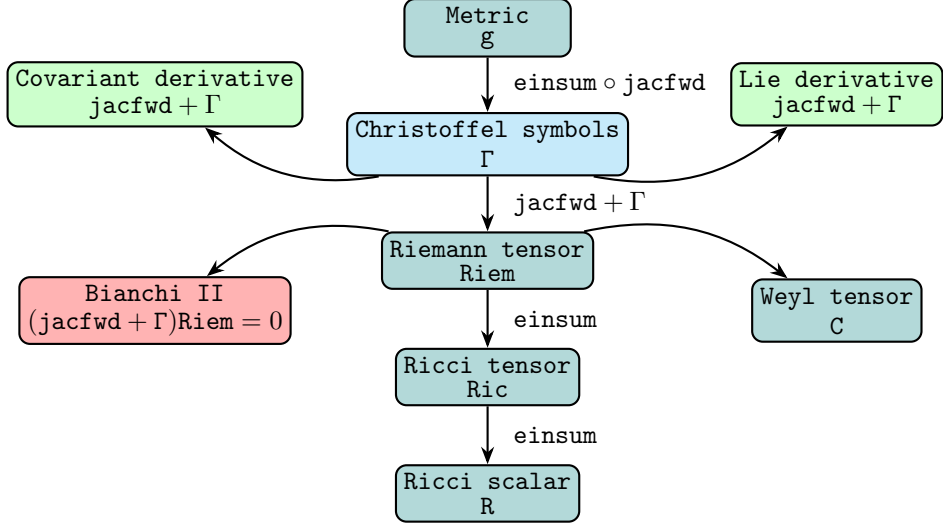


Figure 2: The directed-acyclic graph (DAG) for computing the differential geometric quantities from the metric tensor g in analogy to Figure 8 and Eq. (??). The transformations include repeated differentiation implemented via forward-mode Jacobian jacfwd and tensor index contractions implemented via einsum . Branches compute the Weyl tensor C and enforce Bianchi identities $(\text{jacfwd} + \Gamma)\text{Riem} = 0$. This framework leverages automatic differentiation and tensor algebra to enable scalable symbolic-numeric computations in geometric deep learning and physics-informed models.

mean absolute error (MAE) or relative ℓ_2 (Rel. ℓ_2) between the ground truth and NeF parametrized tensors (see Eqs. (104a, 104b)).

4D training and validation grid. We overfit the NeFs over synthetic data generated from exact analytic solutions of the Einstein field equations (2): (i) Schwarzschild (69) (static, spherically symmetric), (ii) Kerr (79) (rotating (spin parameter $a > 0$), oblate spheroidal), and (iii) linearized gravitational waves (85). Grid resolution, parameter ranges utilized to generate the distortion-part of the metric tensor grid, i.e., Eq. (5) are detailed in Appendix G.1.

Training specifics. For our tasks, the most effective architectures are MLPs with SiLU activations [33], which excel under derivative-based supervision. Given the sensitivity of training dynamics to the choice of optimizer [34], we employ SOAP [35], a scalable quasi-Newton method shown to enhance gradient alignment in PINNs [36]. We adopt a GradNorm-based scheme [37], enforcing unit-norm gradients mitigating gradient imbalances induced by Sobolev supervision. The explored models span widths and depths from 64×3 to 512×8 , totaling less than 1.9×10^6 parameters (~ 7 MiB). The NeF training (NVIDIA H200 SXM GPU) ranges between 100s (w/o Sobolev training) to 2000s (Sobolev training including metric Hessian).

Accuracy and storage efficiency of EinFields: metric and its covariant-derivatives. Furthermore,

Representation	Rel. ℓ_2	MAE	Storage	Compression
EinFields	2.37E-7	3.93E-7	85 KiB	4035
EinFields (+ Jac)	1.51E-7	2.20E-7	1.1 MiB	311
EinFields (+ Jac + Hess)	1.40E-7	6.89E-8	202 KiB	1698
Explicit grid	—	—	343 MiB	—

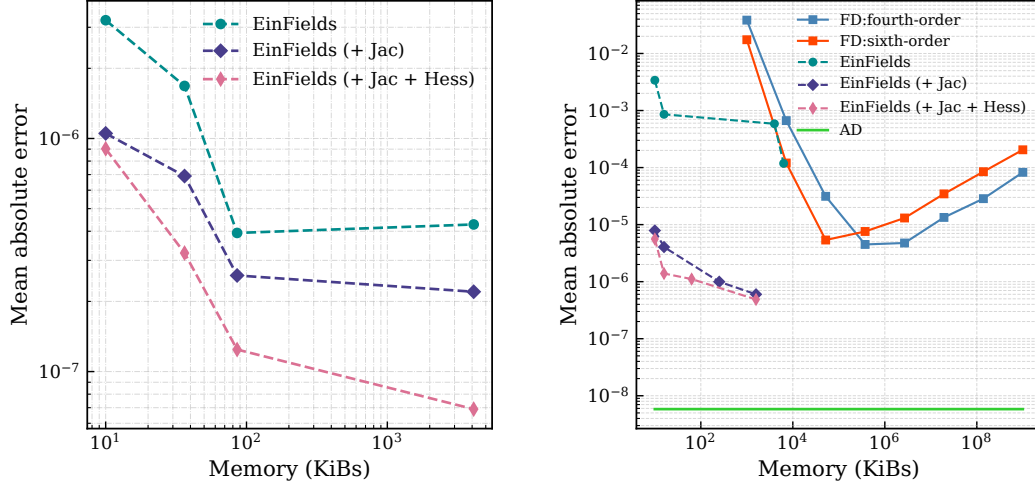
Table 1: Performance evaluation (measured in Rel. ℓ_2 and MAE metrics) and storage efficiency of EinFields parametrized metric tensor fields under different representations (i.e., with and w/o Sobolev trainings). The model with the lowest MAE is selected in each row.

accurate reconstruction of higher-rank tensors from neural tensor fields is critical for recovering geodesics, tidal forces, and related physical quantities. We evaluate EinFields by comparing accuracy–memory tradeoffs for the metric (Figure 3a) and Christoffel symbols (Figure 3b), using the setup of Table 1. Against higher-order FD baselines in FLOAT32, EinFields achieves systematically lower mean absolute error (MAE), avoiding truncation and instability issues that limit FD stencils at small

h. Through AD, we compute Christoffel symbols (Eq.(50)), tensor covariant derivatives (Eq.(49)), Riemann tensor (Eq.(57)), and contracted quantities (Weyl, Ricci tensors, Ricci scalar, Kretschmann invariant; Sec. B.3.6). Table 2 shows that EinFields outperforms FD stencils by $10-10^5$ in accuracy across these quantities, while all being unpacked merely from the implicit NN weights.

Geometric quantity	Storage [GiB]		MAE		
	Full	Sym.	GT (FD)	EinFields (AD)	GT (AD)
Christoffel symbol	26	16	5.37E-6	4.87E-7	5.83E-9
Riemann tensor	103	8.0	1.78E-2	2.53E-7	2.86E-8
Weyl tensor	103	4.0	1.72E-2	5.71E-7	5.89E-8
Ricci tensor	6.5	4.0	4.81E-2	1.02E-6	9.02E-8
Ricci scalar	0.4	0.4	5.35E-2	5.66E-5	1.31E-8
Kretschmann invariant	0.4	0.4	1.33E-2	1.71E-5	3.32E-8

Table 2: Performance evaluation of EinFields reconstructed differential geometric quantities for the Schwarzschild geometry in spherical coordinates. Columns 2–3 report memory usage for full and symmetry-reduced components. Columns 4–6 report MAE relative to analytical solutions: FD stencils for $h = 0.01$ on the ground-truth (GT (FD)), EinFields via AD, and AD applied directly to the analytic solution (GT (AD)).

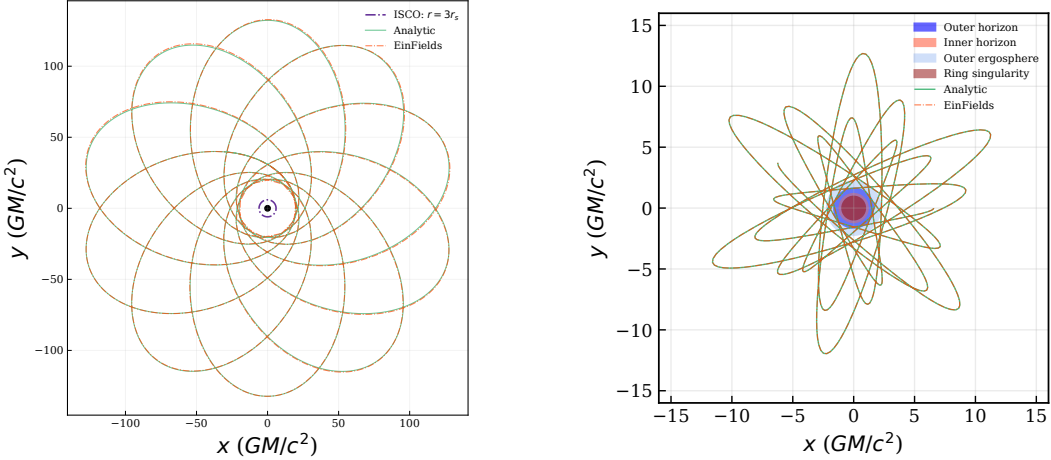


(a) Accuracy of EinFields for different NN sizes (measured in KiBs required to store all FLOAT32 parameters) as trendlines for different training schemes. Each metric tensor component has MAE values ranging from $1E-6$ to $1E-8$. Apart from high accuracy, one additionally acquires $\sim 1000 - 4000$ times compression factors in storage memory gain, as detailed in Table 1.

(b) Accuracy of EinFields' Christoffel symbols derived from the metric tensor, shown as trendlines in FLOAT32 (KiBs). The trendlines show different training schemes (with and without Sobolev training) with MAE values ranging from $1E-4$ to $1E-7$. We benchmark against fourth-order and sixth-order stencils with truncation errors $\mathcal{O}(h^5)$ and $\mathcal{O}(h^7)$, respectively. Our framework outperforms FD stencils by more than an order of magnitude in accuracy.

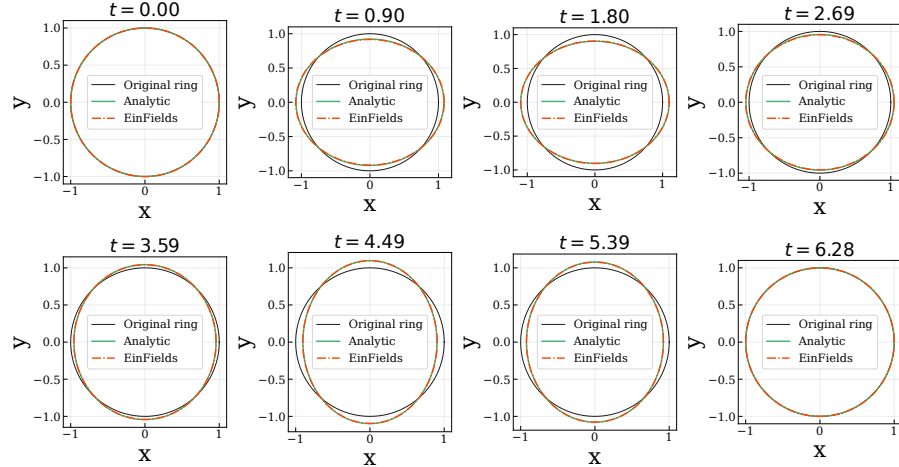
Figure 3: Trendlines of accuracy versus storage memory (KiB) requirement for the metric tensor and Christoffel symbols. For the explicit grid storage this is computed as `num of grid collocation points` $\times 4$, with 4 bytes for single precision (FLOAT32). For the NeFs, this corresponds to the storage memory of the compact implicit NN weights.

Reconstructing seminal tests of GR. As a part of validation, we demonstrate here the reconstruction quality of EinFields for recovering seminal tests associated with general relativistic dynamics on curved manifolds, i.e., geodesics motion – refer Eq.(55) around Schwarzschild – Fig.(4a) and Kerr solutions – Fig.(4b) (see Appendices G.7.1 and G.7.2 for details) and geodesic deviation – Eq.(59) describing oscillating ring of test particles due to gravitational wave distortions – refer Eq.(108) and Appendix G.9 for details. Each of these use-cases shows excellent agreement with the analytic



(a) Schwarzschild metric: perihelion precession.

(b) Kerr metric ($a = 0.95$): Zackiger orbits.



(c) Stretching and squeezing of a circular ring of test particles due to “+” polarization of weak gravitational wave strains detected at *future null-infinity* \mathcal{J}^+ (i.e. extraction at $r \rightarrow \infty$, at fixed retarded time).

results, although, are subject to accumulated temporal rollout errors (see Appendix (G.8)) and heavily affected by floating-point errors requiring FLOAT64 precision.

Curvature tensor and scalar reconstruction. EinFields enable high-fidelity retrieval of curvature tensors and scalars (necessitate Hessian-augmented Sobolev training). This includes the Kretschmann invariant \mathcal{K} for the Kerr geometry – a ring curvature singularity (true singularity corresponding to infinite curvature) analytically defined by Eq.(83). This ring singularity is also captured by our NeFs in Figs. (17b, 17c). Similarly, Weyl scalar $\Psi_4(t, r)$ – Eq.(109), a primary scalar quantity used for observable GW signals extraction from simulations are shown in Fig. 20b (Rel. $\ell_2 \approx \text{E-}5$).

5 Conclusion

EinFields provide an efficient and continuous representation of 4-dimensional spacetime. By combining *neural tensor fields* with the exactness of automatic differentiation, it yields a scalable, discretization-free, and resolution-invariant framework that faithfully captures the underlying physics. Our framework enables achieving E-7–E-9 decimal digit accuracy with a compression factor on the order of 1000–4,000 relative to explicit grids in numerical relativity, while supporting training across diverse coordinate charts, thereby enhancing its applicability to general relativistic simulations. Our framework is validated across several canonical test beds of GR. Compared to finite-difference schemes, EinFields deliver up to five orders of magnitude improvement in the accuracy of the tensor derivative (in FLOAT32), positioning it as a compelling neural alternative for current and next-generation NR simulation workflows.

Acknowledgments

We sincerely thank Nils Deppe for valuable feedback on several numerical relativity-related aspects of the paper.

The ELLIS Unit Linz, the LIT AI Lab, the Institute for Machine Learning, are supported by the Federal State Upper Austria. We thank the projects FWF AIRI FG 9-N (10.55776/FG9), AI4GreenHeatingGrids (FFG- 899943), Stars4Waters (HORIZON-CL6-2021-CLIMATE-01-01). We thank NXAI GmbH, Audi AG, Silicon Austria Labs (SAL), Merck Healthcare KGaA, GLS (Univ. Waterloo), TÜV Holding GmbH, Software Competence Center Hagenberg GmbH, dSPACE GmbH, TRUMPF SE + Co. KG.

Sandeep S. Cranganore was supported by the FWF Bilateral Artificial Intelligence initiative under Grant Agreement number 10.55776/COE12.

References

- [1] B. P. Abbott et al. Observation of gravitational waves from a binary black hole merger. *Phys. Rev. Lett.*, 116:061102, Feb 2016. doi: 10.1103/PhysRevLett.116.061102.
- [2] B. P. Abbott et al. Gw150914: The advanced ligo detectors in the era of first discoveries. *Phys. Rev. Lett.*, 116:131103, Mar 2016. doi: 10.1103/PhysRevLett.116.131103.
- [3] B. P. Abbott et al. Properties of the binary black hole merger gw150914. *Phys. Rev. Lett.*, 116:241102, Jun 2016. doi: 10.1103/PhysRevLett.116.241102.
- [4] Kota Hayashi, Kenta Kiuchi, Koutarou Kyutoku, Yuichiro Sekiguchi, and Masaru Shibata. Jet from binary neutron star merger with prompt black hole formation. *Phys. Rev. Lett.*, 134:211407, May 2025. doi: 10.1103/PhysRevLett.134.211407.
- [5] B. P. Abbott et al. Multi-messenger observations of a binary neutron star merger*. *The Astrophysical Journal Letters*, 848(2):L12, oct 2017. doi: 10.3847/2041-8213/aa91c9.
- [6] Nils Thuerey, Philipp Holl, Maximilian Mueller, Patrick Schnell, Felix Trost, and Kiwon Um. Physics-based deep learning. *arXiv preprint arXiv:2109.05237*, 2021.
- [7] Xuan Zhang, Limei Wang, Jacob Helwig, Youzhi Luo, Cong Fu, Yaochen Xie, Meng Liu, Yuchao Lin, Zhao Xu, Keqiang Yan, et al. Artificial intelligence for science in quantum, atomistic, and continuum systems. *arXiv preprint arXiv:2307.08423*, 2023.
- [8] Steven L Brunton, Bernd R Noack, and Petros Koumoutsakos. Machine learning for fluid mechanics. *Annual review of fluid mechanics*, 52(1):477–508, 2020.
- [9] Zongyi Li, Nikola Borislavov Kovachki, Kamyar Azizzadenesheli, Burigede Liu, Kaushik Bhattacharya, Andrew M. Stuart, and Anima Anandkumar. Fourier neural operator for parametric partial differential equations. In *9th International Conference on Learning Representations, ICLR 2021, Virtual Event, Austria, May 3-7, 2021*. OpenReview.net, 2021.
- [10] Johannes Brandstetter, Daniel E. Worrall, and Max Welling. Message passing neural PDE solvers. In *The Tenth International Conference on Learning Representations, ICLR 2022, Virtual Event, April 25-29, 2022*. OpenReview.net, 2022.
- [11] Cristian Bodnar, Wessel P Bruinsma, Ana Lucic, Megan Stanley, Anna Allen, Johannes Brandstetter, Patrick Garvan, Maik Riechert, Jonathan A Weyn, Haiyu Dong, Jayesh K Gupta, Kit Thambiratnam, Alexander T Archibald, Chun-Chieh Wu, Elizabeth Heider, Max Welling, Richard E Turner, and Paris Perdikaris. A foundation model for the earth system. *Nature*, 641(8065):1180–1187, May 2025.
- [12] Johannes Brandstetter. Envisioning better benchmarks for machine learning PDE solvers. *Nat. Mac. Intell.*, 7(1):2–3, 2025. doi: 10.1038/S42256-024-00962-Z.
- [13] Jeong Joon Park, Peter Florence, Julian Straub, Richard Newcombe, and Steven Lovegrove. DeepSDF: Learning continuous signed distance functions for shape representation. In *Proceedings of the IEEE/CVF Conference on Computer Vision and Pattern Recognition*, pages 165–174, 2019.
- [14] Zhiqin Chen and Hao Zhang. Learning implicit fields for generative shape modeling. In *Proceedings of the IEEE/CVF Conference on Computer Vision and Pattern Recognition*, pages 5939–5948, 2019.

[15] Lars Mescheder, Michael Oechsle, Michael Niemeyer, Sebastian Nowozin, and Andreas Geiger. Occupancy networks: Learning 3d reconstruction in function space. In *Proceedings of the IEEE/CVF Conference on Computer Vision and Pattern Recognition*, pages 4460–4470, 2019.

[16] James Bradbury, Roy Frostig, Peter Hawkins, Matthew James Johnson, Chris Leary, Dougal Maclaurin, George Necula, Adam Paszke, Jake VanderPlas, Skye Wanderman-Milne, and Qiao Zhang. JAX: composable transformations of Python+NumPy programs, 2018.

[17] C.W. Misner, K.S. Thorne, J.A. Wheeler, and D.I. Kaiser. *Gravitation*. Princeton University Press, 2017. ISBN 9780691177793.

[18] Eric Poisson. *A Relativist’s Toolkit: The Mathematics of Black-Hole Mechanics*. Cambridge University Press, 2004.

[19] Jürgen Jost. *Riemannian Geometry and Geometric Analysis*. Universitext. Springer Berlin, Heidelberg, Berlin, Heidelberg, 5th edition, 2008. ISBN 978-3-540-77341-2. doi: 10.1007/978-3-540-77341-2.

[20] Marsha J Berger and Joseph Oliger. Adaptive mesh refinement for hyperbolic partial differential equations. *Journal of Computational Physics*, 53(3):484–512, 1984. ISSN 0021-9991. doi: [https://doi.org/10.1016/0021-9991\(84\)90073-1](https://doi.org/10.1016/0021-9991(84)90073-1).

[21] Geoffrey Lovelace. Computational challenges in numerical relativity in the gravitational-wave era. *Nature Computational Science*, 1(7):450–452, July 2021.

[22] Mark A. Scheel et al. The sxs collaboration’s third catalog of binary black hole simulations, 2025.

[23] Michael Boyle, Keefe Mitman, Mark Scheel, and Leo Stein. The sxs package, May 2025.

[24] Roland Haas, Christian D. Ott, Bela Szilagyi, Jeffrey D. Kaplan, Jonas Lippuner, Mark A. Scheel, Kevin Barkett, Curran D. Muhlberger, Tim Dietrich, Matthew D. Duez, Francois Foucart, Harald P. Pfeiffer, Lawrence E. Kidder, and Saul A. Teukolsky. Simulations of inspiraling and merging double neutron stars using the spectral einstein code. *Phys. Rev. D*, 93:124062, Jun 2016. doi: 10.1103/PhysRevD.93.124062.

[25] Bengt Fornberg. *Introduction*, page 1–3. Cambridge Monographs on Applied and Computational Mathematics. Cambridge University Press, 1996.

[26] Alireza Rashti, Rossella Gamba, Koustav Chandra, David Radice, Boris Daszuta, William Cook, and Sebastiano Bernuzzi. Binary black hole waveforms from high-resolution gr-athena++ simulations. *Phys. Rev. D*, 111:104078, May 2025. doi: 10.1103/n5pz-qv3x.

[27] Yiheng Xie, Towaki Takikawa, Shunsuke Saito, Or Litany, Shiqin Yan, Numair Khan, Federico Tombari, James Tompkin, Vincent Sitzmann, and Srinath Sridhar. Neural fields in visual computing and beyond. *CoRR*, abs/2111.11426, 2021.

[28] Ben Mildenhall, Pratul P Srinivasan, Matthew Tancik, Jonathan T Barron, Ravi Ramamoorthi, and Ren Ng. Nerf: Representing scenes as neural radiance fields for view synthesis. *Communications of the ACM*, 65(1):99–106, 2021.

[29] Thomas Müller, Alex Evans, Christoph Schied, and Alexander Keller. Instant neural graphics primitives with a multiresolution hash encoding. *ACM Transactions on Graphics*, 41(4):1–15, July 2022. ISSN 1557-7368. doi: 10.1145/3528223.3530127.

[30] Wojciech Marian Czarnecki, Simon Osindero, Max Jaderberg, Grzegorz Swirszcz, and Razvan Pascanu. Sobolev training for neural networks. In *Proceedings of the 31st International Conference on Neural Information Processing Systems*, NIPS’17, page 4281–4290, Red Hook, NY, USA, 2017. Curran Associates Inc. ISBN 9781510860964.

[31] Hwijae Son, Jin Woo Jang, Woo Jin Han, and Hyung Ju Hwang. Sobolev training for physics informed neural networks, 2021.

[32] A. Griewank and A. Walther. *Evaluating Derivatives: Principles and Techniques of Algorithmic Differentiation, Second Edition*. Other Titles in Applied Mathematics. Society for Industrial and Applied Mathematics, 2008. ISBN 9780898716597.

[33] Stefan Elfwing, Eiji Uchibe, and Kenji Doya. Sigmoid-weighted linear units for neural network function approximation in reinforcement learning. *Neural Networks*, 107:3–11, 2018. doi: 10.1016/J.NEUNET.2017.12.012.

[34] Sifan Wang, Ananyae Kumar Bhartari, Bowen Li, and Paris Perdikaris. Gradient alignment in physics-informed neural networks: A second-order optimization perspective, 2025.

[35] Nikhil Vyas, Depen Morwani, Rosie Zhao, Mujin Kwun, Itai Shapira, David Brandfonbrener, Lucas Janson, and Sham Kakade. Soap: Improving and stabilizing shampoo using adam, 2025.

[36] M. Raissi, P. Perdikaris, and G.E. Karniadakis. Physics-informed neural networks: A deep learning framework for solving forward and inverse problems involving nonlinear partial differential equations. *Journal of Computational Physics*, 378:686–707, 2019. ISSN 0021-9991. doi: <https://doi.org/10.1016/j.jcp.2018.10.045>.

[37] Zhao Chen, Vijay Badrinarayanan, Chen-Yu Lee, and Andrew Rabinovich. Gradnorm: Gradient normalization for adaptive loss balancing in deep multitask networks. In *International conference on machine learning*, pages 794–803. PMLR, 2018.

[38] S. Kobayashi and K. Nomizu. *Foundations of Differential Geometry*. Number Bd. 1 in Foundations of Differential Geometry. Interscience Publishers, 1963. ISBN 9780470496480.

[39] C.J. Isham. *Modern Differential Geometry for Physicists*. World Scientific lecture notes in physics. World Scientific, 1999. ISBN 9789810235628.

[40] J. Lee. *Introduction to Smooth Manifolds*. Graduate Texts in Mathematics. Springer New York, 2012. ISBN 9781441999825.

[41] S. Carroll, S.M. Carroll, and Addison-Wesley. *Spacetime and Geometry: An Introduction to General Relativity*. Addison Wesley, 2004. ISBN 9780805387322.

[42] Michael M. Bronstein, Joan Bruna, Taco Cohen, and Petar Velickovic. Geometric deep learning: Grids, groups, graphs, geodesics, and gauges. *CoRR*, abs/2104.13478, 2021.

[43] Maurice Weiler, Patrick Forré, Erik Verlinde, and Max Welling. *Equivariant and Coordinate Independent Convolutional Networks*. 2023.

[44] Raoul Bott and Loring W. Tu. *de Rham Theory*, pages 13–88. Springer New York, New York, NY, 1982. ISBN 978-1-4757-3951-0. doi: 10.1007/978-1-4757-3951-0_2.

[45] Terence Tao. What is a gauge?, 2008.

[46] G.D. Birkhoff and R.E. Langer. *Relativity and Modern Physics*. Harvard University Press, 1923.

[47] R P Kerr and A Schild. Republication of: A new class of vacuum solutions of the einstein field equations. *General Relativity and Gravitation*, 41(10):2485–2499, October 2009.

[48] S. Chandrasekhar. *The Mathematical Theory of Black Holes*, pages 5–26. Springer Netherlands, Dordrecht, 1984. ISBN 978-94-009-6469-3. doi: 10.1007/978-94-009-6469-3_2.

[49] V. Frolov and I. Novikov. *Black Hole Physics: Basic Concepts and New Developments*. Fundamental Theories of Physics. Springer Netherlands, 1998. ISBN 9780792351450.

[50] Saul A. Teukolsky. The kerr metric. *Classical and Quantum Gravity*, 32(12):124006, jun 2015. doi: 10.1088/0264-9381/32/12/124006.

[51] Robert H. Boyer and Richard W. Lindquist. Maximal analytic extension of the kerr metric. *Journal of Mathematical Physics*, 8(2):265–281, 02 1967. ISSN 0022-2488. doi: 10.1063/1.1705193.

[52] Matt Visser. The kerr spacetime: A brief introduction, 2008.

[53] Andrzej Krasiński. Ellipsoidal space-times, sources for the kerr metric. *Annals of Physics*, 112(1):22–40, 1978. ISSN 0003-4916. doi: [https://doi.org/10.1016/0003-4916\(78\)90079-9](https://doi.org/10.1016/0003-4916(78)90079-9).

[54] Ezra Newman and Roger Penrose. An approach to gravitational radiation by a method of spin coefficients. *Journal of Mathematical Physics*, 3(3):566–578, 05 1962. ISSN 0022-2488. doi: 10.1063/1.1724257.

[55] Ian Ruchlin, Zachariah B. Etienne, and Thomas W. Baumgarte. SENR/NRPy+: Numerical relativity in singular curvilinear coordinate systems. *Phys. Rev. D*, 97:064036, Mar 2018. doi: 10.1103/PhysRevD.97.064036.

[56] Kurt Hornik, Maxwell Stinchcombe, and Halbert White. Universal approximation of an unknown mapping and its derivatives using multilayer feedforward networks. *Neural Networks*, 3(5):551–560, 1990. ISSN 0893-6080. doi: [https://doi.org/10.1016/0893-6080\(90\)90005-6](https://doi.org/10.1016/0893-6080(90)90005-6).

[57] Tero Karras, Miika Aittala, Samuli Laine, Erik Härkönen, Janne Hellsten, Jaakko Lehtinen, and Timo Aila. Alias-free generative adversarial networks. In M. Ranzato, A. Beygelzimer, Y. Dauphin, P.S. Liang, and J. Wortman Vaughan, editors, *Advances in Neural Information Processing Systems*, volume 34, pages 852–863. Curran Associates, Inc., 2021.

[58] Vincent Sitzmann, Julien N. P. Martel, Alexander W. Bergman, David B. Lindell, and Gordon Wetzstein. Implicit neural representations with periodic activation functions. In Hugo Larochelle, Marc'Aurelio Ranzato, Raia Hadsell, Maria-Florina Balcan, and Hsuan-Tien Lin, editors, *Advances in Neural Information Processing Systems 33: Annual Conference on Neural Information Processing Systems 2020, NeurIPS 2020, December 6-12, 2020, virtual*, 2020.

[59] Amer Essakine, Yanqi Cheng, Chun-Wun Cheng, Lipei Zhang, Zhongying Deng, Lei Zhu, Carola-Bibiane Schönlieb, and Angelica I Aviles-Rivero. Where do we stand with implicit neural representations? a technical and performance survey. *arXiv preprint arXiv:2411.03688*, 2024.

[60] Samuele Papa, Riccardo Valperga, David Knigge, Miltiadis Kofinas, Phillip Lippe, Jan-Jakob Sonke, and Efstratios Gavves. How to train neural field representations: A comprehensive study and benchmark, 2024.

[61] Jörg Behler and Michele Parrinello. Generalized neural-network representation of high-dimensional potential-energy surfaces. *Phys. Rev. Lett.*, 98:146401, Apr 2007. doi: 10.1103/PhysRevLett.98.146401.

[62] Albert Reed, Thomas Blanford, Daniel C. Brown, and Suren Jayasuriya. Implicit neural representations for deconvolving sas images, 2021.

[63] Yuan Yin, Matthieu Kirchmeyer, Jean-Yves Franceschi, Alain Rakotomamonjy, and Patrick Gallinari. Continuous pde dynamics forecasting with implicit neural representations. In *International Conference on Learning Representations*, 2023.

[64] George Em Karniadakis, Ioannis G Kevrekidis, Lu Lu, Paris Perdikaris, Sifan Wang, and Liu Yang. Physics-informed machine learning. *Nature Reviews Physics*, 3(6):422–440, June 2021.

[65] Sifan Wang, Shyam Sankaran, Hanwen Wang, and Paris Perdikaris. An expert’s guide to training physics-informed neural networks, 2023.

[66] Guandao Yang, Serge Belongie, Bharath Hariharan, and Vladlen Koltun. Geometry processing with neural fields. In M. Ranzato, A. Beygelzimer, Y. Dauphin, P.S. Liang, and J. Wortman Vaughan, editors, *Advances in Neural Information Processing Systems*, volume 34, pages 22483–22497. Curran Associates, Inc., 2021.

[67] Tiago Novello, Guilherme Schardong, Luiz Schirmer, Vinícius da Silva, Hélio Lopes, and Luiz Velho. Exploring differential geometry in neural implicits. *Computers & Graphics*, 108:49–60, 2022. ISSN 0097-8493. doi: <https://doi.org/10.1016/j.cag.2022.09.003>.

[68] Arturs Berzins, Andreas Radler, Eric Volkmann, Sebastian Sanokowski, Sepp Hochreiter, and Johannes Brandstetter. Geometry-informed neural networks. In *Forty-second International Conference on Machine Learning*, 2025.

[69] Dario Izzo and Pablo Gómez. Geodesy of irregular small bodies via neural density fields. *Communications Engineering*, 1(1):48, December 2022.

[70] Luke Thomas Smith, Tom Horrocks, Naveed Akhtar, Eun-Jung Holden, and Daniel Wedge. Implicit neural representation for potential field geophysics. *Scientific Reports*, 15(1):9799, March 2025.

[71] Raimon Luna, Juan Calderón Bustillo, Juan José Seoane Martínez, Alejandro Torres-Forné, and José A. Font. Solving the teukolsky equation with physics-informed neural networks. *Phys. Rev. D*, 107:064025, Mar 2023. doi: 10.1103/PhysRevD.107.064025.

[72] Zhi-Han Li, Chen-Qi Li, and Long-Gang Pang. Solving einstein equations using deep learning, 2023.

[73] Aditya Chetan, Guandao Yang, Zichen Wang, Steve Marschner, and Bharath Hariharan. Accurate differential operators for neural fields, 2024.

[74] Tianhe Yu, Saurabh Kumar, Abhishek Gupta, Sergey Levine, Karol Hausman, and Chelsea Finn. Gradient surgery for multi-task learning, 2020.

[75] Bo Liu, Xingchao Liu, Xiaojie Jin, Peter Stone, and Qiang Liu. Conflict-averse gradient descent for multi-task learning, 2021.

[76] Guangyuan Shi, Qimai Li, Wenlong Zhang, Jiaxin Chen, and Xiao-Ming Wu. Recon: Reducing conflicting gradients from the root for multi-task learning, 2023.

[77] Qiang Lui, Mengyu Chu, and Nils Thuerey. Config: Towards conflict-free training of physics informed neural networks, 2025.

[78] Youngsik Hwang and Dong-Young Lim. Dual cone gradient descent for training physics-informed neural networks, 2025.

[79] Fuerst, S. V. and Wu, K. Radiation transfer of emission lines in curved space-time*. *A&A*, 424(3):733–746, 2004. doi: 10.1051/0004-6361:20035814.

[80] C. W. F. Everitt, D. B. DeBra, B. W. Parkinson, J. P. Turneaure, J. W. Conklin, M. I. Heifetz, G. M. Keiser, A. S. Silbergleit, T. Holmes, J. Kolodziejczak, M. Al-Meshari, J. C. Mester, B. Muhlfelder, V. G. Solomonik, K. Stahl, P. W. Worden, W. Bencze, S. Buchman, B. Clarke, A. Al-Jadaan, H. Al-Jibreel, J. Li, J. A. Lipa, J. M. Lockhart, B. Al-Suwaidan, M. Taber, and S. Wang. Gravity probe b: Final results of a space experiment to test general relativity. *Phys. Rev. Lett.*, 106:221101, May 2011. doi: 10.1103/PhysRevLett.106.221101.

[81] V. Venkatraman Krishnan, M. Bailes, W. van Straten, N. Wex, P. C. C. Freire, E. F. Keane, T. M. Tauris, P. A. Rosado, N. D. R. Bhat, C. Flynn, A. Jameson, and S. Osłowski. Lense–thirring frame dragging induced by a fast-rotating white dwarf in a binary pulsar system. *Science*, 367(6477):577–580, 2020. doi: 10.1126/science.aax7007.

[82] Michael Boyle et al. The sxs collaboration catalog of binary black hole simulations. *Classical and Quantum Gravity*, 36(19):195006, sep 2019. doi: 10.1088/1361-6382/ab34e2.

[83] Vishwanath Saragadam, Daniel LeJeune, Jasper Tan, Guha Balakrishnan, Ashok Veeraraghavan, and Richard G. Baraniuk. Wire: Wavelet implicit neural representations, 2023.

A Technical Appendices and Supplementary Material

B Introduction to General Relativity

This appendix provides the mathematical background and intuition on differential geometry (covering every aspect of the paper and the library), and general relativity. We remark that the reader may appreciate several related works, such as [19, 38–40] for mathematically rigorous coverage of differential geometry. For more physics-oriented readers, the following books extensively cover general relativity and numerical relativity [17, 41, 18] as alternative resources. Additionally, the Geometric Deep Learning (GDL) community can also find more ML-centric introduction to differential geometry in the following work [42, 43].

Table 3: Table of notations

Symbol	Description
\mathcal{M}	Arbitrary manifold
\mathcal{M}	4-dimensional spacetime manifold
$\eta_{\mu\nu}$	Flat Lorentzian metric
x^μ	Original coordinates
\bar{x}^μ	Transformed coordinates
e_μ	Basis set
ϑ^μ	Dual basis set
\bar{e}_μ	Transformed basis set
$\bar{\vartheta}^\mu$	Transformed dual basis set
$\frac{\partial}{\partial x^\mu}$	Coordinate basis (equivalent to partial derivative operator)
$T_p \mathcal{M}$	Tangent space at point p
$T_p^* \mathcal{M}$	Cotangent space at point p
$\Omega^1(\mathcal{M})$	Space of one-forms
$\Gamma(T\mathcal{M})$	Smooth sections of a tangent bundle (collection of vector fields)
$\Gamma(T^*\mathcal{M})$	Smooth sections of a cotangent bundle (collection of one-forms)
Φ^*	Pullback operation
Φ_*	Pushforward operation
$\text{Riem}(\mathcal{M})$	Set of (pseudo-)Riemannian metrics on \mathcal{M}
$\text{Diff}(\mathcal{M})$	Set of diffeomorphism maps on \mathcal{M}
\times	Cartesian (tensor) product
\otimes	Kronecker (tensor) product
\mathcal{D}_v	Directional derivative
\mathcal{L}_v	Lie derivative with respect to vector field v
∇_μ	Covariant derivative
δ_ν^μ	Kronecker delta (identity matrix)
c	Speed of light
G	Newton's constant

B.1 Fundamental concepts of differential geometry & and tensor calculus

The main concepts covered in this appendix are:

1. *Fundamental concepts of differential geometry and tensor calculus*: We introduce contravariance and covariance, and further vector and dual vector spaces. This allows us to define tangent and cotangent spaces.
2. *Tensors and tensor fields*: Next, we define tensors and tensor fields, operations on tensor fields, and the Lie derivative as a generalization of the directional derivative for tensor fields.
3. *Riemannian and Lorentzian geometry*: This is the meat of Appendix B. We introduce 4-dimensional spacetime as a continuous differentiable manifold. Via the metric, we can define Riemannian manifolds, and finally Lorentzian manifolds as a pseudo-Riemannian manifold. Next, we discuss connections, covariant derivatives, and Christoffel symbols. This is all mathematical background that is required to introduce parallel transport, geodesics, the Riemann curvature tensor, the Ricci tensor, the Ricci scalar, the Weyl tensor, and finally curvature invariants and the stress-energy-momentum tensor. We end with Einstein field equations, reflecting back on the coordinate-independency of GR.

B.1.1 Contravariant and covariant components

Loosely speaking, an n -dimensional vector $v \in \mathbb{R}^n$ can be expanded in its basis as $v = v^1 e_1 + v^2 e_2 + \dots + v^n e_n$, or $v = v^i e_i$ if we use Einstein sum convention. In general relativity, we write $v = v^\mu e_\mu$, where Greek indices indicate 4-dimensional space-time. Thus, in this non-Euclidean setting, it is necessary to distinguish objects that carry an upper index (contravariant) versus objects that carry a lower index (covariant), since they satisfy different geometric properties and transformation laws.

Definition 1 (Contravariance of vector components): Let $X \subset \mathbb{R}^n$ be a coordinate system (frame) that is spanned by a coordinate basis set $\{e_\mu\}_{1 \leq \mu \leq n}$, i.e., each basis vector can be expressed as $e_\mu = \frac{\partial}{\partial x^\mu}$. A vector $v \in X$ can be expanded in its coordinate basis as $v = v^\mu(x) e_\mu := v^\mu(x) \frac{\partial}{\partial x^\mu}$. When transforming the vector

v to a new coordinate system, spanned by another coordinate basis set $\{\bar{e}_\nu\}_{1 \leq \nu \leq n}$, i.e., $\bar{e}_\nu = \frac{\partial}{\partial \bar{x}^\nu}$, one can express the vector components in the new coordinate system $\bar{v}^\nu = \bar{v}^\nu(\bar{x})$ as

$$\bar{v}^\nu(\bar{x}) = \sum_\mu \frac{\partial \bar{x}^\nu}{\partial x^\mu} v^\mu(x). \quad (7)$$

The ratio of change of the vector components is the inverse of the ratio of the base components. In other words, vector components transform inversely – or contravariantly – with respect to basis transformations, i.e., transform in the opposite way to the change in the coordinate system. Most contravariant objects represent physical quantities like displacement, velocity, and momentum, which must adjust when the coordinate basis changes.

Definition 2 (Covariance of basis set): Let $X \subset \mathbb{R}^n$ be a coordinate system (frame) that is spanned by a coordinate basis set $\{e_\mu\}_{1 \leq \mu \leq n}$, i.e., each basis vector can be expressed as $e_\mu = \frac{\partial}{\partial x^\mu}$. A vector $v \in X$ can be expanded in its coordinate basis as $v = v^\mu(x) e_\mu := v^\mu(x) \frac{\partial}{\partial x^\mu}$. When transforming the vector v to a new coordinate system, spanned by another coordinate basis set $\{\bar{e}_\nu\}_{1 \leq \nu \leq n}$, i.e., $\bar{e}_\nu = \frac{\partial}{\partial \bar{x}^\nu}$, then, the basis set itself transforms as,

$$\frac{\partial}{\partial \bar{x}^\nu} = \sum_\mu \frac{\partial x^\mu}{\partial \bar{x}^\nu} \frac{\partial}{\partial x^\mu}. \quad (8)$$

Note that we have introduced the concept of contravariant and covariant transformation by the example of vector components and the respective basis set. In general, we speak of contravariant w.r.t. their corresponding basis sets. I.e., contravariant components have covariant basis sets and covariant components have contravariant basis sets. As we introduce next, an object with covariant components is an object of the dual space. These covariant vectors, or covectors, typically represent gradients, such as the gradient of a function. A gradient represents the change w.r.t. an infinitesimal change in a direction. It is intuitive that if we make the direction larger, the change becomes larger as well. In other words, if we change the basis vectors in which we measure this change, the gradient transforms covariantly w.r.t. the basis vectors.

B.1.2 Dual space

While the concept of a vector space is well known in the machine learning community, there is a closely associated concept of a *dual vector space* (succinctly called dual space), which is an algebraic dual to the vector space itself with the same dimensions.

Definition 2 (Dual vector space): Let $(\mathcal{V}, +, \cdot)$ be a vector space over a field F (e.g., \mathbb{R}, \mathbb{C}). The (algebraic) dual space $(\mathcal{V}^*, +, \cdot)$ is a vector space of linear functionals (maps) $\mathcal{V}^* := \{v^* | v^*(v) = c \forall v \in \mathcal{V}, \forall c \in F\}$, satisfying:

$$(v^* + w^*)(v) = v^*(v) + w^*(v) \quad (9)$$

$$v^*(\alpha v + \beta w) = \alpha v^*(v) + \beta w^*(w) \quad (10)$$

$$(cv^*)(v) = c(v^*(v)) \quad (11)$$

for all $v^*, w^* \in \mathcal{V}^*$, $v, w \in \mathcal{V}$, $\alpha, \beta, c \in F$. Elements of the dual space \mathcal{V}^* are sometimes referred to as *covectors* or *one-forms* [44].²

For example, suppose, we are given a basis $\{e_1, \dots, e_n\}$ of a vector space \mathcal{V} . Then, one can introduce a dual basis set $\{\vartheta^1, \dots, \vartheta^n\}$ of the dual space \mathcal{V}^* . Let $v = (\alpha_1 e_1 + \alpha_2 e_2 + \dots + \alpha_n e_n) \in \mathcal{V}$, $\forall \{\alpha_i\}_{1 \leq i \leq n} \in F$. Thus, the action of the linear functionals ϑ^i on the vector reads: $\vartheta^i(v) = \vartheta^i(\alpha_1 e_1 + \alpha_2 e_2 + \dots + \alpha_n e_n) = \alpha_i \vartheta^i(e_i) = \alpha^i$, $i = 1, \dots, n$ and $\vartheta^i(e_j) = \delta_j^i$, where we have used the orthonormality condition, and δ_j^i is the Kronecker delta symbol. Conceptually, the covector ϕ is a (complex-conjugated if $F = \mathbb{C}$) row-vector, which acts on a column vector v to produce $\alpha \in F$. Colloquially speaking, an element of the dual space \mathcal{V}^* “eats up” an element of the vector space \mathcal{V} and returns a scalar (duality pairing).

B.1.3 Tangent and cotangent spaces

Definition 1 (Tangent space): Let \mathcal{M} be a smooth (C^∞) manifold of dimension n . The tangent space $T_p \mathcal{M}$ at point $p \in \mathcal{M}$ is a set of d -dimensional vectors (called tangent vectors) attached at point p , defined as $T_p \mathcal{M} := \{(p, v) : v \in \mathbb{R}^d\}$, and carries the structure of a real vector space. Every tangent space is spanned by an ordered basis $\{e_\mu|_p\}_{1 \leq \mu \leq n} = \left\{ \frac{\partial}{\partial x^1} \Big|_p, \dots, \frac{\partial}{\partial x^n} \Big|_p \right\} \in T_p \mathcal{M}$, and vectors can be expanded in this basis as:

²A finite dimensional vector space is isomorphic to its double dual, i.e. $\mathcal{V} \cong (\mathcal{V}^*)^*$.

$$v|_p = v^\mu(x) \frac{\partial}{\partial x^\mu} \Big|_p, \quad (12)$$

where $v^\mu(x)$ are the components of the vector in this basis $\{e_\mu|_p\}_{1 \leq \mu \leq n}$ of the tangent space $T_p\mathcal{M}$.

It is worth noting that $\dim(T_p\mathcal{M}) = \dim(\mathcal{M})$. With this setup, we can now formally introduce the definition of tangent vectors.

Definition 2 (Tangent vector): A vector $v|_p \in T_p\mathcal{M}$ is called as a tangent vector if it acts as a derivation, i.e., a linear map acting on smooth functions $f \in C^\infty(\mathcal{M})$ at a point $p \in \mathcal{M}$. Specifically, the map $v|_p : C^\infty(\mathcal{M}, \mathbb{R}) \rightarrow \mathbb{R}$ satisfies³:

- i) $v(f+g) = v(f) + v(g) \quad \forall f, g \in C^\infty(\mathcal{M}, \mathbb{R})$ (linearity)
- ii) $v(f) = 0$, when f is a constant function, i.e., v acts trivially on constants.
- iii) $v(fg) = f(p)v(g) + g(p)v(f) \quad \forall f, g \in C^\infty(\mathcal{M}, \mathbb{R})$ (Leibniz product rule)

From the definition above, it follows that tangent vectors should be regarded as derivation maps. This is equivalent to the notion of a “directional derivative” [39]

$$(\mathcal{D}_v f)(p) := \frac{d}{dt} f(p + tv|_p) \Big|_{t=0} = v^\mu(x) \frac{\partial f}{\partial x^\mu} \Big|_p, \quad \forall v = v^\mu(x) \frac{\partial}{\partial x^\mu} \Big|_p \in T_p\mathcal{M}, \quad \forall f \in C^\infty(\mathcal{M}, \mathbb{R}). \quad (13)$$

Directional derivatives are traditionally defined only for scalar-valued functions. This shall be revisited rigorously for a more generalized concept called the “Lie-derivatives”, which operates on general tensors, c.f. Section B.2.3.

Thus, $T_p\mathcal{M}$ is the space of directional derivatives. The disjoint union of all the tangent spaces at every point $p \in \mathcal{M}$ forms a structure called *tangent bundles* [39]:

$$T\mathcal{M} = \bigsqcup_{p \in \mathcal{M}} T_p\mathcal{M} = \bigcup_{p \in \mathcal{M}} \{(p, v|_p) : v|_p \in T_p\mathcal{M}\}. \quad (14)$$

Tangent vectors as vector fields. In physics, quantities that vary spatiotemporally as a continuum representation are defined as *fields*, featuring in domains such as electrodynamics, gravity, fluid dynamics, or continuum mechanics.

A *vector field* V is a smooth assignment of a tangent vector $v|_p$ to each point $p \in \mathcal{M}$. Thus, a vector field is a map $V : C^\infty(\mathcal{M}) \rightarrow C^\infty(\mathcal{M})$, and is defined as:

$$(V(f))(p) = v|_p(f). \quad (15)$$

Theorem 1 (Cotangent space): Let \mathcal{M} be a smooth (C^∞)-manifold (differentiable). The cotangent space $T_p^*\mathcal{M} := \{(p, v^*|_p) | \langle v^*|_p, v|_p \rangle = \kappa, \forall p \in \mathcal{M}, v|_p \in T_p\mathcal{M}, \kappa \in \mathbb{R}\}$ at point $p \in \mathcal{M}$ is the set of all linear maps $v^*|_p : T_p\mathcal{M} \rightarrow \mathbb{R}$, i.e., dual to the tangent space. The cotangent space $T_p^*\mathcal{M}$ is spanned by an ordered basis set $\{dx^1|_p, dx^2|_p, \dots, dx^d|_p\}$. Thus, any $v^*|_p \in T_p^*\mathcal{M}$ can be expanded as:

$$v^*|_p = v_\mu^*(x) dx^\mu = v_\mu^*(x) dx^\mu \Big|_p. \quad (16)$$

It follows that $dx^\mu \Big|_p \left(\frac{\partial}{\partial x^\nu} \Big|_p \right) := \left(\frac{\partial x^\mu}{\partial x^\nu} \Big|_p \right) = \delta_\nu^\mu$, and $\dim T_p^*\mathcal{M} = \dim T_p\mathcal{M} = \dim \mathcal{M}$. The disjoint union of all the cotangent spaces at every point $p \in \mathcal{M}$ are known as *cotangent bundles* [39]:

$$T^*\mathcal{M} = \bigsqcup_{p \in \mathcal{M}} T_p^*\mathcal{M} = \bigcup_{p \in \mathcal{M}} \{(p, v^*|_p) : v^*|_p \in T_p^*\mathcal{M}\}. \quad (17)$$

One can also construct fields of cotangent vectors (*cotangent fields*) by picking up an element of $T_p^*(\mathcal{M}) \quad \forall p \in \mathcal{M}$ in a smooth manner. I.e., by assigning one cotangent vector smoothly at each point of the manifold, one obtains a cotangent field (i.e., a smooth section of the cotangent bundle). These cotangent fields are known in mathematical literature as *one-forms*. The set of all smooth one-forms on \mathcal{M} is commonly denoted as $\Omega^1(\mathcal{M})$.

³For sake of ease, we will drop $|_p$ whenever possible.

B.2 Tensors and tensor fields

Definition 3 (Tensors): A rank (r, s) tensor T at a point $p \in \mathcal{M}$ is described as a multilinear map:

$$T : \underbrace{\mathcal{V}^* \times \dots \times \mathcal{V}^*}_{r-\text{copies}} \times \underbrace{\mathcal{V} \times \dots \times \mathcal{V}}_{s-\text{copies}} \rightarrow \mathbb{R}, \quad (18)$$

where \times denotes the *Cartesian* product and the resultant tensor has a total rank of $r + s$. A tensor takes in r covectors and s vectors, returning a real number, in a multilinear way (linear in each argument separately). The r and s input vectors and covectors pair with the r and s being the covariant and contravariant components, respectively. Equivalently, a tensor is an element that lives in a tensor product of vector and dual spaces, i.e., $T \in (\mathcal{V})^{\otimes r} \otimes (\mathcal{V}^*)^{\otimes s}$. A tensor in a particular basis choice $\{e_{\alpha_n}\}_{1 \leq n \leq r} \in \mathcal{V}$ and $\{\vartheta^{\beta_n}\}_{1 \leq n \leq s} \in \mathcal{V}^*$ is given by

$$T = T^{\alpha_1 \alpha_2 \dots \alpha_r}_{\beta_1 \beta_2 \dots \beta_s} e_{\alpha_1} \otimes \dots \otimes e_{\alpha_r} \otimes \vartheta^{\beta_1} \otimes \dots \otimes \vartheta^{\beta_s}, \quad (19)$$

where $T^{\alpha_1 \alpha_2 \dots \alpha_r}_{\beta_1 \beta_2 \dots \beta_s} := T(\vartheta^{\alpha_1}, \dots, \vartheta^{\alpha_r}, e_{\beta_s}, \dots, e_{\beta_s})$ are the coefficients of the tensor w.r.t. the basis set.

B.2.1 Tensor transformation properties

A pivotal criterion for an object to be classified as a tensor(field) is that it transforms according to a well-defined rule under changes of coordinates. Let $\{e_{\alpha_n}\}_{1 \leq n \leq r} \in \mathcal{V}$, $\{\vartheta^{\beta_n}\}_{1 \leq n \leq s} \in \mathcal{V}^*$, and $\{\bar{e}_{\alpha_n}\}_{1 \leq n \leq r} \in \mathcal{V}$, $\{\bar{\vartheta}^{\beta_n}\}_{1 \leq n \leq s} \in \mathcal{V}^*$ be two coordinate systems on a smooth manifold \mathcal{M} , related by a smooth invertible map. Consider a tensor field of type (r, s) with components $T^{\alpha_1 \dots \alpha_r}_{\beta_1 \dots \beta_s}$ in the original coordinate system $\{e_{\alpha_n}\}_{1 \leq n \leq r} \in \mathcal{V}$, $\{\vartheta^{\beta_n}\}_{1 \leq n \leq s} \in \mathcal{V}^*$. Under a change of coordinate systems, the components in the new coordinate system $\{\bar{e}_{\alpha_n}\}_{1 \leq n \leq r} \in \mathcal{V}$, $\{\bar{\vartheta}^{\beta_n}\}_{1 \leq n \leq s} \in \mathcal{V}^*$ transform according to the following tensor transformation law:

$$\bar{T}^{\mu_1 \dots \mu_r}_{\nu_1 \dots \nu_s}(\bar{x}) = \mathcal{J}_{\alpha_1}^{\mu_1} \dots \mathcal{J}_{\alpha_r}^{\mu_r} T^{\alpha_1 \dots \alpha_r}_{\beta_1 \dots \beta_s}(x) (\mathcal{J}^{-1})_{\nu_1}^{\beta_1} \dots (\mathcal{J}^{-1})_{\nu_s}^{\beta_s}, \quad (20)$$

where $\mathcal{J}_{\alpha_k}^{\mu_k} \equiv \frac{\partial \bar{x}^{\mu_k}}{\partial x^{\alpha_k}}$ and $(\mathcal{J}^{-1})_{\nu_l}^{\beta_l} \equiv \frac{\partial x^{\beta_l}}{\partial \bar{x}^{\nu_l}}$ are the Jacobian and Jacobian inverse matrices in the coordinate basis, respectively. $\mathcal{J}_{\alpha_k}^{\mu_k}$ is the contravariant transformation of the contravariant components of $T^{\alpha_1 \dots \alpha_r}_{\beta_1 \dots \beta_s}$, whereas $(\mathcal{J}^{-1})_{\nu_l}^{\beta_l}$ is the covariant transformation of the covariant components of $T^{\alpha_1 \dots \alpha_r}_{\beta_1 \dots \beta_s}$. The indices μ_k, ν_l label components in the new coordinates and α_k, β_l are dummy indices summed over the old coordinates. A key feature of a tensor is that, if it is zero in one coordinate system, it is zero in every other coordinate system. This transformation law ensures that the tensorial nature of the object is preserved independent of the coordinate chart chosen.

Tensor fields. A tensor field is a collection of tensor-valued rank quantities (r, s) such that at each point $p \in \mathcal{M}$, the multilinear function associates a value $T_p \in \mathcal{V}_p^{\otimes r} \otimes (\mathcal{V}_p^*)^{\otimes s}$. Thus, the components $T^{\alpha_1 \dots \alpha_r}_{\beta_1 \dots \beta_s}(p)$ are functions of the points of the manifold.

By definition, some known examples of tensor fields in physics and machine learning are:

- Rank 0 tensor, e.g., temperature field $\varphi : \mathbb{R}^m \rightarrow \mathbb{R}$ (scalar field)
- Rank $(1, 0)$ tensor, e.g., (velocity, momentum, displacement) vector fields $v : \mathbb{R}^m \rightarrow \mathbb{R}^n$ (contravariant vector field). These rank $(1, 0)$ tensors have one component that transforms contravariantly, and “eats up” a covariant component, e.g., v^T to produce a scalar.
- Rank $(0, 1)$ tensor, e.g., gradient vector fields $\nabla : \mathbb{R} \rightarrow \mathbb{R}^m$ (covariant vector field). These rank $(0, 1)$ tensors have one component that transforms covariantly, and “eat up” a contravariant component to produce a scalar.
- Rank $(0, 2)$ tensor, e.g., a matrix representing a bilinear form that takes in two vectors and outputs a scalar. We will see the metric tensor $g_{\mu\nu}$ as an example. In continuum and structural mechanics, a known example is the *strain* tensor ϵ_{ij} representing the deformation of a crystal (body) caused by external forces such as stress.
- Rank $(2, 0)$ tensor, e.g., a matrix as a multilinear map that takes in two covectors and outputs a scalar. An example for a rank $(2, 0)$ tensor is the outer product of two vectors. An example is the *Cauchy stress tensor* σ^{ij} from structural mechanics, which represents the internal forces per unit area acting

inside a material body. The stress tensor takes in two vectors, i.e., the normal vector to the surface (describing orientation), and the direction vector along which the force acts (projection), and returns a scalar (force per unit area in that direction).

B.2.2 Operations on tensor fields

For multiple tensors of the same type (r, s) , the algebraic operations such as addition, subtraction or multiplication by functions are straightforward. Here, we address multiplication of tensors of different ranks.

Let T be a rank (r, s) tensor and S a rank (p, q) tensor. One can construct a *tensor product* $T \otimes S$ resulting in a new tensor of rank $(r + p, s + q)$, defined by

$$T \otimes S(e_{\alpha_1}, \dots, e_{\alpha_r}, e_{\eta_1}, \dots, e_{\eta_p}, \varphi^{\beta_1}, \dots, \varphi^{\beta_s}, \varphi^{\delta_1}, \dots, \varphi^{\delta_q}) \quad (21)$$

$$= T(e_{\alpha_1}, \dots, e_{\alpha_r}, e_{\eta_1}, \dots, e_{\eta_p}) S(\varphi^{\beta_1}, \dots, \varphi^{\beta_s}, \varphi^{\delta_1}, \dots, \varphi^{\delta_q}), \quad (22)$$

and the components of this composite tensor read,

$$(T \otimes S)^{\alpha_1 \dots \alpha_r \eta_1 \dots \eta_p}_{\beta_1 \dots \beta_s \delta_1 \dots \delta_q} := T^{\alpha_1 \dots \alpha_r}_{\beta_1 \dots \beta_s} S^{\eta_1 \dots \eta_p}_{\delta_1 \dots \delta_q}. \quad (23)$$

Another useful rule is that of contracting over repeated index/indices each from the vector and dual space respectively. Consider a rank (r, s) tensor

$$T^{\alpha_1 \dots \alpha_p \dots \alpha_r}_{\beta_1 \dots \beta_p \dots \beta_s} = T^{\alpha_1 \dots \alpha_r}_{\beta_1 \dots \beta_s}. \quad (24)$$

I.e., α_p is summed-over in the contravariant and covariant indices, and, thus it gets contracted. The resulting tensor is of rank $(r - 1, s - 1)$.

B.2.3 Lie derivative: Generalizing the notion of directional derivatives for tensor fields

Directional derivatives are of great importance and often appear in domains such as fluid dynamics, where a scalar field is differentiated with respect to a vector flow field, capturing infinitesimal dragging of scalar fields along flows generated by a vector field. Flows can be viewed as “diffeomorphisms” [18] induced by these vector fields.

However, generalizing the notion of directional derivatives require defining derivatives of a set of tensor fields of arbitrary rank (r, s) w.r.t. a set of vector fields. This is often not possible on arbitrary manifolds, and requires a concept of differentiating in a tensorial setting. Geometrically, to compare tensors at infinitesimally separated points on a manifold \mathcal{V} , say at points $p, q \in \mathcal{M}$ requires to “drag” the tensor from p to q (also called parallel transporting, c.f. Section ??).

Alternatively, a simpler approach to describe the dragging is via coordinate transformation from p to q . This is the idea behind the *Lie derivative*. The Lie derivative along a vector field $v|_p \in T_p \mathcal{M}$ measures by how much the changes in a tensor along v differ from a mere infinitesimal passive coordinate transformation of the tensor generated by v . In other words, the Lie derivative compares the actual rate of change of the tensor as you move along v against the change you’d get if everything were just shifted passively via a coordinate transformation. We provide a rough sketch of the derivation, but detailed explanations can be found here [40, 18].

Consider an infinitesimal coordinate transformation which maps the vector with coordinates $x^\mu|_p$ at point p to $\bar{x}^\mu|_q$ at point q :

$$\bar{x}^\mu|_q = x^\mu|_p + \delta\xi v^\mu(x)|_p. \quad (25)$$

It is to explicitly note that the original coordinates $x^\mu|_p$ and the transformed coordinates $\bar{x}^\mu|_q$ are components of the same set of basis vectors. Such transformations fall under the category of *active coordinate transformations* that map points (or tensors at those points) at old locations to new locations in the old coordinate system – in this case by “moving” a small amount $\delta\xi$ along the vector field $v|_p \in T_p \mathcal{M}$. In other words, an active coordinate transformation maps points (and tensors) to new locations in the old coordinate system keeping the basis set intact. Whereas, passive transformations assign new coordinates to the old points (and tensors) by transforming the basis set itself.

Assuming a coordinate basis, one can differentiate the transformation w.r.t. the original coordinates, which yields

$$\frac{\partial \bar{x}^\mu}{\partial x^\nu} = \delta^\mu_\nu + \delta\xi \frac{\partial v^\mu(x)}{\partial x^\nu}. \quad (26)$$

The result contains the identity matrix δ^μ_ν and a small correction due to the flow field $v^\mu(x)$. To the first order, the inverse of the above Jacobian is $\frac{\partial x^\nu}{\partial \bar{x}^\mu} = \delta^\nu_\mu - \delta\xi \frac{\partial v^\mu(x)}{\partial x^\nu}$.

The Lie-derivative of a tensor field T_ν^μ with respect to v^μ follows a similar pattern and is defined via the limes:

$$\mathcal{L}_v T_\nu^\mu = \lim_{\delta\xi \rightarrow 0} \frac{T_\nu^\mu(\bar{x}) - \bar{T}_\nu^\mu(\bar{x})}{\delta\xi}. \quad (27)$$

In this scheme, it is important to distinguish three distinct tensor field evaluations: a) $T_\nu^\mu(x)$ (original tensor in untransformed coordinates), b) $\bar{T}_\nu^\mu(\bar{x})$ (transformed tensor in the transformed coordinates) and c) $T_\nu^\mu(\bar{x})$ (original tensor in transformed coordinates).

In order to compute Equation (27), we need two important concepts from differential geometry called *push-forward* and *pull-back* operations. We direct the interested readers to more advanced literature [39, 40, 38]

These three separate tensors fields can be related in the following manner: Firstly, the tensor mapped to the new set of coordinates $\bar{T}_\nu^\mu(\bar{x})$ can be obtained via Equation(20),

$$\bar{T}_\nu^\mu(\bar{x}) = (\mathcal{J}^{-1})_\rho^\mu \mathcal{J}_\nu^\sigma T_\sigma^\rho(x) \equiv T_\nu^\mu(x) + \delta\xi \left(\frac{\partial v^\mu}{\partial x^\sigma} T_\nu^\sigma(x) - \frac{\partial v^\sigma}{\partial x^\nu} T_\sigma^\mu(x) \right) + \mathcal{O}(\delta\xi^2). \quad (28)$$

Secondly, the original tensor in transformed coordinates $T_\nu^\mu(\bar{x})$ can be evaluated at q , by a Taylor expansion:

$$T_\nu^\mu(\bar{x}) = T_\nu^\mu(\bar{x}^\sigma) = T_\nu^\mu(x^\sigma + \delta\xi v^\sigma) = T_\nu^\mu(x) + \delta\xi v^\sigma \frac{\partial T_\nu^\mu}{\partial x^\sigma} + \mathcal{O}(\delta\xi^2). \quad (29)$$

Substituting Equations (28) (29) into the Lie-derivative definition of Equation (27), and $\delta\xi \rightarrow 0$ one finds the following final expression:

$$\mathcal{L}_v T_\nu^\mu = v^\sigma \frac{\partial T_\nu^\mu}{\partial x^\sigma} - \underbrace{\frac{\partial v^\mu}{\partial x^\sigma} T_\nu^\sigma(x)}_{\text{pullback}} + \underbrace{\frac{\partial v^\sigma}{\partial x^\nu} T_\sigma^\mu(x)}_{\text{pushforward}}. \quad (30)$$

The pushforward and pullback operations drag the transformed tensor field onto the original point, where differences can be computed.

Thus, tensors are being compared in the same tangent/cotangent space. Mathematically, for smooth maps⁴ (diffeomorphisms) $\Phi : \mathcal{M} \rightarrow \mathcal{N}$ the pushforward $\Phi_* : T_p \mathcal{M} \rightarrow T_{\Phi(p)} \mathcal{N}$ pushes vector fields forward from one tangent space of a domain $T_p \mathcal{M}$ to the tangent space of another tangent space $T_{\Phi(p)} \mathcal{N}$. The pullback, a dual linear map to pushforward, drags covectors (one-forms) living in cotangent spaces $(\Phi_*)^* \equiv \Phi^* : T_{\Phi(p)}^* \mathcal{N} \rightarrow T_p^* \mathcal{M}$ in the reverse direction to the domain. Hence, the contributions from the pushforward on the vector field components and pullback on the covector field components jointly determine the structure of the Lie derivative of a mixed tensor field, as expressed in Equation (30). These operations offer a coherent mathematical framework for transitioning between tangent and cotangent bundles mapped onto other tangent and cotangent bundles via smooth maps, acting appropriately on vector fields and one-forms, respectively.

For any arbitrary rank (r, s) tensor, Equation (30) can be generalized to:

$$(\mathcal{L}_v T)^{\mu_1 \dots \mu_r}_{\nu_1 \dots \nu_s} = v^\sigma \frac{\partial}{\partial x^\sigma} T^{\mu_1 \dots \mu_r}_{\nu_1 \dots \nu_s} - \sum_{i=1}^r T^{\mu_1 \dots \sigma \dots \mu_r}_{\nu_1 \dots \nu_s} \frac{\partial v^{\mu_i}}{\partial x^\sigma} + \sum_{j=1}^s T^{\mu_1 \dots \mu_r}_{\nu_1 \dots \sigma \dots \nu_s} \frac{\partial v^\sigma}{\partial x^{\nu_j}}. \quad (31)$$

Lie-derivatives do not require the notion of a connection. Connections will be introduced in detail in Section B.3.3 and intuitively stating, connects two distinct Tangent spaces at different points, which is not to be confused with a pullback operation. Here, is an instructive comparison table for that compares different differentiation schemes:

Feature	Directional derivative	Covariant derivative	Lie derivative
Input function	Scalar fields	Tensor fields	Tensor fields
Connection dependence	✗	✓ (Explicit)	✗
Captures curvature	✗	✓	✗
Measures	Scalar changes	Intrinsic curvature	Diffeomorphisms (flows)

Table 4: Comparison between actions of directional, covariant, and Lie derivatives.

B.3 Riemannian and Lorentzian Geometry

B.3.1 Four dimensional spacetime as a continuous differentiable manifold

The fabric of spacetime according to general relativity is a combination of three-dimensional space and a strictly positively progressing time direction into a single four-dimensional continuum. Thus, space and time mix between each other through special orthogonal transformations $\text{SO}(1, 3)$ called the *Lorentz transformations*. In order to rigorously define the four-dimensional spacetime, it is necessary to define the following:

⁴for e.g., dragging of coordinates as in Equation (25) due to flows induced by vector fields.

Definition 4 (Manifold): A n -dimensional manifold \mathcal{M} is a space, that, locally resembles the n -dimensional Euclidean space \mathbb{R}^n . However, combining these local patches together, globally, the space deviates from \mathbb{R}^n .

Definition 5 (Hausdorff space): Let \mathcal{K} be a topological space. Then \mathcal{K} is said to be a Hausdorff space if: For every pair of distinct points $x, y \in \mathcal{K}$ with $x \neq y$, there exist open sets $U, V \subset \mathcal{K}$ such that:

$$x \in U, \quad y \in V, \quad \text{and} \quad U \cap V = \emptyset. \quad (32)$$

Definition 6 (Differentiable manifold): An n -dimensional differentiable manifold is a Hausdorff topological space \mathcal{K} such that:

i) Locally \mathcal{K} is homeomorphic to \mathbb{R}^n . Thus, $\forall p \in \mathcal{K}$ there is an open set \mathcal{U} such that $p \in \mathcal{U}$ and a homeomorphism $\phi : \mathcal{U} \rightarrow \mathcal{Z}$ with \mathcal{Z} an open subset of \mathbb{R}^n .

ii) For two subsets \mathcal{U}_α and \mathcal{U}_β with $\mathcal{U}_\alpha \cap \mathcal{U}_\beta \neq \emptyset$, the homeomorphisms (topologically isomorphic) $\phi_\alpha : \mathcal{U}_\alpha \rightarrow \mathcal{Z}_\alpha$ and $\phi_\beta : \mathcal{U}_\beta \rightarrow \mathcal{Z}_\beta$ are compatible, i.e., the map $\phi_\beta \circ \phi_\alpha^{-1} : \phi_\alpha(\mathcal{U}_\alpha \cap \mathcal{U}_\beta) \rightarrow \phi_\beta(\mathcal{U}_\beta \cap \mathcal{U}_\alpha)$ is smooth (infinitely differentiable \mathcal{C}^∞), and so is its inverse map.

The ϕ_α are often called charts and a collection (union) of them $\bigcup_\alpha \phi_\alpha$ is called an *atlas*. These charts provides a coordinate system, labeling $\mathcal{U}_\alpha \subset \mathcal{K}$. The coordinate associated to $p \in \mathcal{U}_\alpha$ is:

$$\phi_\alpha(p) = (x^1(p), x^2(p), \dots, x^n(p))$$

Mathematically, the spacetime continuum denoted as \mathcal{M} , is a *differentiable manifold* with the structure of an *Hausdorff* topological space.

To summarize, a differentiable manifold is a space that may be curved or complicated globally, but looks like Euclidean space up close, and allows for smooth calculus to be done on it. The Hausdorff space ensures that one can separate points nicely with open sets. This avoids weird pathological cases and makes limits and continuity well-behaved. Locally Euclidean means that one can do calculus as if we were on flat space – even if the whole space is curved. And finally, the compatibility between overlapping charts ensures that one can do calculus consistently across different charts.

B.3.2 Metric tensor

Definition 7 (Metric): A metric g is a rank $(0, 2)$ tensor field that is defined as a symmetric bilinear map that assigns to each $p \in \mathcal{M}$ a positive-definite inner product $g : T_p \mathcal{M} \times T_p \mathcal{M} \rightarrow \mathbb{R}$ such that

- i) $g(v|_p, w|_p) = g(v, w) = g(w, v) \quad \forall v, w \in T_p \mathcal{M}$ (symmetric)
- ii) For any $p \in \mathcal{M}$, $g(v, w) = 0 \quad \forall w|_p \in T_p \mathcal{M}$ implying $v|_p = 0$ (non-degenerate).

Represented in the basis set of the tangent space, the metric components at each point p is given by

$$g_{\mu\nu} = g_{\nu\mu} := g_p \left(\frac{\partial}{\partial x^\mu} \Big|_p, \frac{\partial}{\partial x^\nu} \Big|_p \right) \quad (33)$$

and the metric can be expanded as,

$$g = g_{\mu\nu}(x) dx^\mu \otimes dx^\nu. \quad (34)$$

Geometrically, the metric defined in Equation (34) generalizes the notion of distances and induces a norm $\|\cdot\|_p : T_p \mathcal{M} \rightarrow \mathbb{R}$ for generic coordinates such as curvilinear and/or manifolds possessing geometries that are intrinsically non-Euclidean in nature, for e.g., spaces of constant positive sectional curvature $K = 1$ (e.g., a 2-sphere \mathbb{S}^2 embedded in \mathbb{R}^3), spaces of constant sectional curvature $K = -1$ such as hyperbolic geometry (Bolyai-Lobachevsky spaces \mathbb{H}^2).

The distance between two points in such cases is called the *line element*, which is defined as,

$$ds^2 = g_{\mu\nu}(x) dx^\mu dx^\nu. \quad (35)$$

For an n -dimensional manifold \mathcal{M} , the metric tensor $g_{\mu\nu}$ is a $n \times n$ symmetric matrix, $g(\phi_\mu, \phi_\nu) := \langle \phi_\mu, \phi_\nu \rangle$, with $\frac{n(n+1)}{2}$ independent components (not necessarily expanded in the coordinate basis):

$$g_{\mu\nu} = \begin{pmatrix} \langle \phi_0, \phi_0 \rangle & \langle \phi_0, \phi_1 \rangle & \cdots & \langle \phi_0, \phi_{n-1} \rangle \\ \langle \phi_1, \phi_0 \rangle & \langle \phi_1, \phi_1 \rangle & \cdots & \langle \phi_1, \phi_{n-1} \rangle \\ \vdots & \vdots & \ddots & \vdots \\ \langle \phi_{n-1}, \phi_0 \rangle & \langle \phi_{n-1}, \phi_1 \rangle & \cdots & \langle \phi_{n-1}, \phi_{n-1} \rangle \end{pmatrix}. \quad (36)$$

Definition 8 (Metric bundle): Let \mathcal{M} be a smooth manifold and (x_0, \dots, x_n) be local coordinates on $\mathcal{U} \subset \mathcal{M}$. The bundle of symmetric $(0, 2)$ -tensors on \mathcal{M} is the subbundle $\text{Sym}^2(T^*\mathcal{M}) \subset T^{0,2}\mathcal{M} = T^*\mathcal{M} \times T^*\mathcal{M}$.

In fact, sections of $\text{Sym}^2(T^*\mathcal{M})$ contains all the symmetric bilinear forms, i.e. symmetric $(0, 2)$ -tensor fields, and includes the pseudo-Riemannian metrics on \mathcal{M} .

Riemannian manifolds. A metric g where all diagonal entries of the metric are positive, i.e., $g_{\mu\mu} > 0, \mu = 0, \dots, \dim(\mathcal{M}) - 1$ is called a *Riemannian* metric. Thus, a manifold \mathcal{M} endowed with a Riemannian metric g is known as a *Riemannian manifold* denoted as a tuple (\mathcal{M}, g) [19].

For the Euclidean space \mathbb{R}^n with Cartesian coordinates representation

$$g = dx^1 \otimes dx^1 + \dots + dx^n \otimes dx^n \quad (37)$$

the metric tensor amounts to $g_{ij} = \delta_{ij}$, and boils down to Pythagoras' theorem. A general Riemannian metric prescribes a method to measure the norm of a vector v as $\sqrt{g(v, v)} = \|v\|$ and also allows for measuring angles between any two vectors v, w at each point $\cos\theta = \frac{g(v, w)}{\sqrt{g(v, v)g(w, w)}}$. Like any other tensor, the components of the metric tensor transform under a coordinate change according to Equation (20):

$$\bar{g}_{\alpha\beta}(\bar{x}) = [(\mathcal{J}^{-1})_\alpha^\mu]^\top g_{\mu\nu}(x) (\mathcal{J}^{-1})_\beta^\nu. \quad (38)$$

Definition 9 (Arc length): Let $\gamma : [0, 1] \rightarrow \mathcal{M}$ be a piecewise smooth curve on a differentiable manifold \mathcal{M} , with $\gamma(0) = p$ and $\gamma(1) = q$. The velocity vector along the curve is denoted by $\dot{\gamma}(t)$, which lives in the tangent space $T_{\gamma(t)}\mathcal{M}$. If the curve is expressed in local coordinates $x^\mu(t)$, then the components of the tangent vector $\dot{\gamma}(t)$ are given by $\frac{dx^\mu(t)}{dt}$. The arc length $\mathcal{L}(\gamma)$ (distance) of the curve is then defined by

$$\mathcal{L}(\gamma) = \int_0^1 \|\dot{\gamma}(t)\|_{\gamma(t)} dt = \int_0^1 \sqrt{g_{\mu\nu}(x(t)) \frac{dx^\mu(t)}{dt} \frac{dx^\nu(t)}{dt}} dt. \quad (39)$$

This arc length⁵ is reparameterization invariant, i.e., it does not depend on the choice of parameterization of the curve $\gamma(t)$. It is a very important result that every smooth manifold admits a Riemannian metric.

Lorentzian manifolds. Unlike Riemannian manifolds, spacetime is actually a *pseudo-Riemannian* manifold⁶, that is, the metric is not positive definite. Thus, the underlying metric carries a signature $(-, +, +, +)$, meaning, $g_{tt} < 0$. Consequently, spacetime is a Lorentzian manifold \mathcal{M} , and, forms the basis for electromagnetism and special relativity. The simplest example of a Lorentzian manifold of arbitrary dimension is the *Minkowski* metric, which is flat (meaning no curvature):

$$\eta = -dx^0 \otimes dx^0 + dx^1 \otimes dx^1 + \dots + dx^{n-1} \otimes dx^{n-1}, \quad (40)$$

where, the components of the Minkowski metric are $\eta_{\mu\nu} = \text{diag}(-1, +1, \dots, +1)$. It is possible to find an orthonormal basis $\{e_\mu\}$ of $T_p\mathcal{M}$ around a small neighborhood of point p of a Lorentzian manifold such that, “locally”, the metric resembles the Minkowski metric

$$g_{\mu\nu}|_p = \eta_{\mu\nu}. \quad (41)$$

In the case of Lorentzian manifolds \mathcal{M} , the arc length $\mathcal{L}(\gamma)$ in Eq.(39) is modified due to non positive-definiteness

$$\tau(\sigma) = \int_0^\sigma \sqrt{-g_{\mu\nu}(x) \frac{dx^\mu(\sigma')}{d\sigma'} \frac{dx^\nu(\sigma')}{d\sigma'}} d\sigma', \quad (42)$$

and is sometimes τ is referred to as *proper-time*. The minus sign under the square root ensures the integrand is positive for timelike paths, since for timelike intervals, the inner product of the velocity vector with itself (under the Lorentzian metric) is negative, i.e.,

$$ds^2 = g_{\mu\nu} dx^\mu dx^\nu. \quad (43)$$

Natural isomorphism between vector spaces and dual spaces. The metric provides a natural *isomorphism* between vector spaces and dual spaces and allows the switch between contravariant and covariant components⁷. This is done via the following mapping $g : T_p\mathcal{M} \rightarrow T_p^*\mathcal{M}$, where at each point p , a one-form (covectors) is obtained via contraction operation of a vector field $v|_p$ with the metric g .

⁵It is also called an action in physics.

⁶In general, a pseudo-Riemannian manifold has a signature $(\underbrace{-, \dots, -}_m, \underbrace{+, \dots, +}_n)$.

⁷In the context of numerical relativity the switch between contravariant and covariant components is called “raising and lowering indices”.

For a vector $v|_p = v^\mu \frac{\partial}{\partial x^\mu}$ and the covector $v^*|_p = v_\mu dx^\mu$, the components are related by

$$v_\mu = g_{\mu\nu} v^\nu .$$

Since g is non-degenerate, it is invertible. We denote the inverse metric as $g^{\mu\nu}$, such that $g^{\mu\sigma} g_{\sigma\nu} = \delta_\nu^\mu$. This is a rank $(2, 0)$ tensor of the form $\hat{g} = g^{\mu\nu} \frac{\partial}{\partial x^\mu} \otimes \frac{\partial}{\partial x^\nu}$. Through the inverse metric indices can be raised, e.g. $x^\mu = g^{\mu\nu} x_\nu$.

Such index contraction rules with the metric apply to tensors of rank (r, s) or even quantities that are not tensors:

$$S^{\beta_1 \dots \beta_s}_{\alpha_1 \dots \alpha_r} = \left(\prod_{i=1}^s g^{\beta_i \gamma_i} \right) \left(\prod_{i=1}^r g_{\alpha_i \delta_i} \right) S^{\delta_1 \dots \delta_r}_{\gamma_1 \dots \gamma_s} . \quad (44)$$

B.3.3 Connections & covariant derivative

Transporting vector and tensor fields systematically on manifolds requires mapping vector spaces at one point to vector spaces at another. While this can be done trivially in the Euclidean setting, for Riemannian and Lorentzian manifolds this is a non-trivial since these vector fields and tensor fields live in different vector spaces. This necessitates a geometric object that behaves as a “connector” between vector spaces. This is achieved via a geometric entity called the *affine-connection*, which is a vector-valued one-form.

Definition 10 (Affine connection): Let \mathcal{M} be a smooth manifold and $\Gamma(T\mathcal{M})$ be the space of vector fields on \mathcal{M} , that is the space of smooth sections of the tangent bundle (i.e., the collection of all tangent spaces). An affine connection is a bilinear map

$$\begin{aligned} \nabla : \Gamma(T\mathcal{M}) \times \Gamma(T\mathcal{M}) &\rightarrow \Gamma(T\mathcal{M}) \\ (v, w) &\mapsto \nabla_v w . \end{aligned}$$

The differential operator ∇_v is the covariant derivative satisfying the following for tangent vectors v, w (short for $v|_p, w|_p$):

- i) $\nabla_v(w + z) = \nabla_v w + \nabla_v z$
- ii) $\nabla_{fv} w = f \nabla_v w \quad \forall f \in C^\infty(\mathcal{M}, \mathbb{R})$
- iii) $\nabla_v(fw) = (\mathcal{D}_v f)w + f \nabla_v w \quad \forall f \in C^\infty(\mathcal{M}, \mathbb{R}), \quad \mathcal{D}_v f = v(f)$ is the directional derivative.

The affine connection is completely independent of the metric. However, if a manifold is endowed with a metric, this enables expressing the connection in terms of the metric. In GR, one looks at a special subclass of affine connections called *Levi-Civita connection*, due to the symmetry property of the metric tensor.

Definition 11 (Levi-Civita connection): An affine connection is a Levi-Civita connection for tangent vectors v, w (short for $v|_p, w|_p$) if:

$$\nabla_v g = 0 \quad \forall v \in \Gamma(T\mathcal{M}) \quad (\text{metricity condition}) \quad (45a)$$

$$\nabla_v w - \nabla_w v = [v, w] \quad \forall v, w \in \Gamma(T\mathcal{M}) \quad (\text{torsion-free condition}), \quad (45b)$$

where, $[v, w] = (v^\mu \partial_\mu w^\nu - w^\mu \partial_\mu v^\nu) \partial_\nu$ is the Lie-bracket of vector fields [38].

Intuition behind the torsion-free condition. Imagine you are moving on a smooth surface (like walking on a hill), and you have two “directions” $v|_p$ and $w|_p$ at a point p . Now: First move along v a tiny bit, then subsequently along w . Alternatively, move along w first, then along v , akin to constructing a parallelogram. In flat, Euclidean space, doing these two moves would land you at the same final point, because partial derivatives commute. On a curved surface (a manifold \mathcal{M}), they don’t generally commute – you end up slightly shifted. The Lie bracket $[v, w]$ measures how far off (deficit) you are after moving in v and then w , compared to w and then v . It captures the “non-commutativity” of the vector transport along the two distinct directions, which leads to a non-closure of the parallelogram. Thus, the Lie bracket is intrinsic to the manifold, and shows how the transport of v and w interact. In torsion-free connections, the “commutation failure” is purely due to the manifold’s structure – not any extra “twisting” introduced by the connection itself.

Definition 12 (Parallel transport): Let $\gamma : [0, 1] \rightarrow \mathcal{M}$ be a smooth curve on the manifold, and let T be a smooth (r, s) -rank tensor field defined along the curve γ . The parallel transport of T along the curve $\gamma(\tau)$ is defined by the condition that its directional covariant derivative along the curve’s tangent vector vanishes:

$$\nabla_{\dot{\gamma}(\tau)} T = 0, \quad \forall \tau \in [0, 1], \quad \dot{\gamma}(t) \in T_p \mathcal{M} . \quad (46)$$

In local coordinates $\{x^\mu(\tau)\}$, the parallel transport condition for the components of the tensor field $T_{\nu_1 \dots \nu_s}^{\mu_1 \dots \mu_r}(\tau)$ along the curve $\gamma(t)$ is:

$$\frac{d}{d\tau} T_{\nu_1 \dots \nu_s}^{\mu_1 \dots \mu_r}(\tau) + \sum_{i=1}^r \Gamma_{\lambda\rho}^{\mu_i} \dot{x}^\rho(\tau) T_{\nu_1 \dots \nu_s}^{\mu_1 \dots \lambda \dots \mu_r}(\tau) - \sum_{j=1}^s \Gamma_{\nu_j \rho}^{\lambda} \dot{x}^\rho(\tau) T_{\nu_1 \dots \lambda \dots \nu_s}^{\mu_1 \dots \mu_r}(\tau) = 0. \quad (47)$$

These equations are a set of coupled ODEs, and can be solved uniquely for an initial condition to find a unique vector at each point along the curve $\gamma(\tau)$. This ensures that as the tensor is transported along the curve, its components change in such a way that their covariant rate of change along the curve vanishes.

B.3.4 Christoffel symbols

The Levi-Civita covariant derivative contains, apart from the partial derivative term, a correction field that calibrates the deficit between vector (tensor) fields transported along a path on the manifold. For a basis $\{e_\mu\}$ that is transported the covariant derivative is given by

$$\nabla_{e_\nu} e_\mu(x) = \Gamma_{\mu\nu}^\sigma(x) e_\sigma(x). \quad (48)$$

The *covariant derivative*, denoted by $\nabla_{e_\nu} \equiv \nabla_\nu = \partial_\nu + \Gamma_\nu$, defines a “modified” differentiation operator that preserves tensorial character under general coordinate transformations. The quantities $\Gamma_{\mu\nu}^\sigma$, known as the *Christoffel symbols*, represent the components of the *Levi-Civita connection*, which is uniquely determined by the requirement that the connection is torsion-free and compatible with the metric. Notably, these symbols are symmetric in their lower two indices, i.e., $\Gamma_{\mu\nu}^\sigma = \Gamma_{\nu\mu}^\sigma$. The action of the covariant derivative on a general tensor field of type (r, s) ensures that derivatives of tensors transform covariantly, thereby extending the notion of differentiation from vector calculus to curved manifolds.

$$\begin{aligned} \nabla_\mu T_{\beta_1 \dots \beta_s}^{\alpha_1 \dots \alpha_r}(x) &= \frac{\partial}{\partial x^\mu} T_{\beta_1 \dots \beta_s}^{\alpha_1 \dots \alpha_r}(x) + \sum_{i=1}^r \Gamma_{\mu\sigma}^{\alpha_i}(x) T_{\beta_1 \dots \beta_s}^{\alpha_1 \dots \sigma \dots \alpha_r}(x) \\ &\quad - \sum_{j=1}^s \Gamma_{\mu\beta_j}^\sigma(x) T_{\beta_1 \dots \sigma \dots \beta_s}^{\alpha_1 \dots \alpha_r}(x). \end{aligned} \quad (49)$$

The action of the covariant derivative on a scalar field, simply reduces to a partial derivative

$$\nabla_\mu \phi(x) = \frac{\partial \phi(x)}{\partial x^\mu}.$$

Christoffel symbols can be solely expressed in terms of the metric and its partial derivatives:

$$\Gamma_{\mu\nu}^\rho(x) := \frac{1}{2} g^{\rho\sigma} (\partial_\mu g_{\sigma\nu}(x) + \partial_\nu g_{\sigma\mu}(x) - \partial_\sigma g_{\mu\nu}(x)) = \Gamma_{\nu\mu}^\rho(x). \quad (50)$$

A crucial feature of any connection is that it is **not** a tensorial quantity. Connections don't obey the transformation law in Equation (20) under coordinate changes. This can be easily seen through the components of the Christoffel symbols in the coordinate basis:

$$\bar{\Gamma}_{\mu\nu}^\rho(\bar{x}) = \underbrace{\frac{\partial \bar{x}^\rho}{\partial x^\gamma} \frac{\partial x^\alpha}{\partial \bar{x}^\mu} \frac{\partial x^\beta}{\partial \bar{x}^\nu} \Gamma_{\alpha\beta}^\gamma(x)}_{\text{tensorial contribution}} + \underbrace{\frac{\partial^2 x^\sigma}{\partial \bar{x}^\mu \partial \bar{x}^\nu} \frac{\partial \bar{x}^\rho}{\partial x^\sigma}}_{\text{non-tensorial contribution}}. \quad (51)$$

Christoffel symbols play a significant role in defining most stationary trajectories (shortest or longest) in the non-Euclidean setting.

Lie derivatives revisited: Levi-Civita connection included. In case of a nonzero Levi-civita connection, the partial derivatives of an ordinary Lie derivative in Equation(31) is replaced by the covariant derivatives:

$$(\mathcal{L}_v T)^{\mu_1 \dots \mu_r}_{\nu_1 \dots \nu_s} = v^\sigma \nabla_\sigma T^{\mu_1 \dots \mu_r}_{\nu_1 \dots \nu_s} - \sum_{i=1}^r T^{\mu_1 \dots \sigma \dots \mu_r}_{\nu_1 \dots \nu_s} \nabla_\sigma v^{\mu_i} + \sum_{j=1}^s T^{\mu_1 \dots \mu_r}_{\nu_1 \dots \sigma \dots \nu_s} \nabla_{\nu_j} v^\sigma. \quad (52)$$

The first term advects (drags) the tensor along the flow of v , i.e., this is the “naive” directional derivative part. The second and third terms account for how the basis vectors themselves are changing, due to curvature and due to the vector field v , respectively. It is easy to show that the three terms lead to pair-wise cancellations between the Christoffel symbols present in the three different covariant derivative terms of Equation(52). Due to this, the whole expression boils down to Equation(31), thus corroborating the connection independence of this derivative operator. Differently put, in the covariant derivatives, the Christoffel symbols introduce extra terms. However, the extra Christoffel terms cancel out between the different contributions (first, second, and third terms). One ends up getting exactly the same final expression for the Lie derivative as if only partial derivatives had been used – this is what is meant by “connection independence”.

B.3.5 Geodesic equation

Geodesics are paths that correspond to the most stationary trajectories (shortest or longest distance) that connect two points p and q on a manifold. Often, we only consider locally distance minimizing curves, and refer to them as *geodesics*. Geodesics are obtained by solving a calculus of variations problem on the distance metric $\mathcal{L}(\gamma)$ in Equation (39), i.e.,

$$\delta\mathcal{L}(\gamma) := 0 , \quad (53)$$

(or alternatively on $\tau(\sigma)$ in the Lorentzian setting of Equation (42)). Solving the calculus of variations problem boils down to solving the Euler-Lagrange equations, which mathematically is equivalent to the condition

$$\nabla_{\dot{\gamma}(t)}\dot{\gamma}(t) = 0 , \quad (54)$$

where $\gamma(t)$ is the curve (path) on the manifold, $\dot{\gamma}(t)$ the tangent vector (velocity vector), and ∇ the covariant derivative. Equation (54) intuitively says that the tangent vector is parallel transported along itself – meaning, one is moving without “acceleration” relative to the curved space. Thus, parallel transporting the tangent vector along the curve preserves the tangent vector. In numerical relativity, these corresponds to the equations of motion, i.e. a generalization of the Newton’s acceleration equation $\frac{d^2x^\mu}{d\tau^2} = F^\mu/m$. For full derivations, we direct the readers to refer to [41, 17, 18].

We shall present the final form of a very central second-order ODE describing motion (acceleration) of objects executing geodesic paths around heavy gravitating bodies, namely, the *geodesic equation*

$$\frac{d^2x^\mu}{d\tau^2} + \Gamma_{\rho\sigma}^\mu(x) \frac{dx^\rho}{d\tau} \frac{dx^\sigma}{d\tau} = 0 , \quad (55)$$

where, τ is some affine parameter (typically, chosen to be the proper-time in Equation (42)), $d^2x^\mu/d\tau^2$ is the four-acceleration vector, $dx^\rho/d\tau$ is the four-velocity and $\Gamma_{\rho\sigma}^\mu$ is the Christoffel symbols as seen in Equation (50)).

Importantly, Equation (54) is the geometric statement of the geodesic equation. It’s coordinate-free, i.e., it’s expressed entirely in terms of geometric objects. Equation (55) is the coordinate version of the same idea. Here, one chooses a coordinate system x^μ on the manifold, and the covariant derivative ∇ acting on a vector becomes the partial derivative plus correction terms involving the Christoffel symbols⁸.

B.3.6 Curvature tensors and scalars

Curvature tensors arise naturally in differential geometry as tensorial objects that capture the intrinsic and, where appropriate, extrinsic geometric properties of a manifold. They provide a coordinate-independent way to quantify the curvature of space or spacetime by encoding how the geometry deviates from flatness through the second derivatives, constructed out of Hessians of the metric tensor. Unlike artifacts that may arise from curvilinear coordinate choices on flat manifolds, curvature tensors reflect the true geometric content of a space. These generalize classical notions such as *Gaussian curvature* to higher dimensions and arbitrary signature. Being multilinear objects containing several tensor components, curvature tensors systematically characterize the variation of the metric across different directions. We shall introduce the key curvature related quantities, which include the Riemann relevant ones used in our paper in the following section.

Riemann curvature tensor The *Riemann curvature tensor* $R_{\gamma\alpha\beta}^\mu(x) e_\mu \otimes \vartheta^\gamma \otimes \vartheta^\alpha \otimes \vartheta^\beta$ is a rank $(1, 3)$ tensor, which quantifies the measure to which a vector that is transported along a small loop (also called *holonomy*) fails to return to its original orientation – due to the effect of the intrinsic curvature that the vector field picks up during the transport. The Riemann curvature tensor is defined via the commutators of covariant derivatives acting on components of a vector field v :

$$[\nabla_\alpha, \nabla_\beta]v^\delta(x) = (\nabla_\alpha \nabla_\beta - \nabla_\beta \nabla_\alpha)v^\delta(x) = R_{\alpha\beta\gamma}^\delta(x)v^\gamma(x) . \quad (56)$$

The components of the Riemann curvature tensor are expressed in terms of the Christoffel symbols

$$R_{\alpha\beta\gamma}^\delta(x) = \frac{\partial \Gamma_{\alpha\gamma}^\delta(x)}{\partial x^\beta} - \frac{\partial \Gamma_{\beta\gamma}^\delta(x)}{\partial x^\alpha} + \Gamma_{\gamma\alpha}^\sigma(x)\Gamma_{\beta\sigma}^\delta(x) - \Gamma_{\beta\gamma}^\sigma(x)\Gamma_{\sigma\alpha}^\delta(x) . \quad (57)$$

The Riemann tensor $R_{\alpha\beta\gamma\delta} = g_{\alpha\sigma} R_{\beta\gamma\delta}^\sigma$ obeys the following identities:

$$\begin{aligned} R_{\alpha\beta\gamma\delta} &= -R_{\alpha\beta\delta\gamma} , \\ R_{\alpha\beta\gamma\delta} &= -R_{\beta\alpha\gamma\delta} , \\ R_{\alpha\beta\gamma\delta} &= -R_{\gamma\delta\alpha\beta} . \end{aligned}$$

⁸Ideally, concepts such as connections, parallel transport and covariant derivatives are metric-independent formulation

The Riemann tensor in a n -dimensional manifold has $n^2(n^2 - 1)/12$ independent components. Importantly, it satisfies two additional identities, called the *Bianchi identities*

$$R_{\alpha\beta\gamma\delta} + R_{\alpha\gamma\delta\beta} + R_{\alpha\delta\beta\gamma} = 0 \text{ (Bianchi Identity I),} \quad (58a)$$

$$\nabla_\alpha R_{\beta\gamma\delta\sigma} + \nabla_\beta R_{\gamma\alpha\delta\sigma} + \nabla_\gamma R_{\alpha\beta\delta\sigma} = 0 \text{ (Bianchi Identity II).} \quad (58b)$$

Unlike the Christoffel symbols, which may be non-zero purely due to the choice of coordinates – e.g., when imposing curvilinear coordinates such as polar coordinates (r, ϑ) on the flat Cartesian plane – the Riemann curvature tensor encapsulates the true geometric curvature of a manifold. Since Christoffel symbols represent connection coefficients rather than tensorial objects, their non-vanishing components can give the false impression of intrinsic curvature, even on a flat manifold. In contrast, the Riemann tensor is a bona fide tensor and its vanishing is a coordinate-invariant statement: if the Riemann tensor vanishes in one coordinate system, it vanishes in all coordinate systems. Thus, it provides a definitive criterion for distinguishing truly curved spaces from flat ones, independent of coordinate artifacts.

Geodesic deviation. An important consequence of the existence of a non-zero Riemann tensor is that it encapsulates directional information about how geodesics path converge or diverge. Intuitively, it implies that in Euclidean space \mathbb{R}^d , parallel lines always remain parallel, but in the case of spherical geometry, say \mathbb{S}^{d-1} (constant positive curvature) the parallel lines converge at a point, while for hyperbolic spaces \mathbb{H}^d , the parallel lines continue diverging. This is captured by the *geodesic deviation equation* (sometimes referred to as *Jacobi equation*) [39, 19, 18], which shows how an infinitesimal neighborhood of a given geodesics diverge or converge. Here, we shall give the equation with a brief sketch.

Theorem 2 (Jacobi equation): Let $\gamma_s(\tau)$ be a family of closely spaced geodesics indexed by a smooth one-parameter family s and $\tau \in \mathbb{R}$ the affine parameter. Let $x^\mu(s, \tau)$ be the coordinates of the geodesics $\gamma_s(\tau)$, then the tangent vector field is a directional derivative expressed in these coordinates as $X^\mu = \frac{dx^\mu(s, \tau)}{d\tau}$. Let the set of deviation vector fields $S^\mu = \frac{\partial x^\mu(\tau, s)}{\partial s}|_\tau$. Then, the deviation vector fields that satisfy the acceleration equation are called (Jacobi fields) and read

$$\frac{D^2 S^\mu}{D\tau^2} = R_{\alpha\beta\gamma}^\mu X^\alpha X^\beta S^\gamma, \quad (59)$$

where, $\frac{D}{D\tau} = X^\alpha \nabla_\alpha$ is the directional covariant derivative, i.e., the derivative of a vector field along a given direction on a manifold, while accounting for the manifold's curvature.

Contracted curvature tensors, scalars and invariants

Ricci tensor. From the rank $(1, 3)$ Riemann tensor, one can construct a traced (contracted) symmetric curvature tensor of rank $(0, 2)$, called the *Ricci tensor* $R_{\alpha\beta} \vartheta^\alpha \otimes \vartheta^\beta$,

$$R_{\alpha\gamma\beta}^\gamma = \text{Tr}_g(R_{\alpha\delta\beta}^\gamma) := R_{\alpha\beta}. \quad (60)$$

Mathematically, the Ricci tensor aggregates directional curvature along orthogonal planes. Thus, it can be considered as a curvature average of the Riemann tensor. It is closely related to the concept of sectional curvature and reflects how volume deformations occurs as one evolve under geodesic flow.

Ricci scalar. The traced (contracted) Ricci tensor yields a scalar field called the scalar curvature, also called the *Ricci scalar*. It is defined as

$$R_\alpha^\alpha = \text{Tr}_g(R_{\alpha\beta}) := R. \quad (61)$$

Mathematically, the scalar curvature corresponds to the sum/average over all sectional curvatures, i.e., $R(p) = \sum_{\alpha \neq \beta} \text{Sec}(e_\alpha, e_\beta)|_p \forall p \in \mathcal{M}$. For a point p , in an n -dimensional Riemannian manifold (\mathcal{M}, g) , it characterizes the volume of an ϵ -radius ball in the manifold to the corresponding ball in Euclidean space, given by,

$$\text{Vol}(B_\epsilon(p)) \subset \mathcal{M} = \text{Vol}(B_\epsilon(0) \subset \mathbb{R}^n) \left(1 - \frac{R}{6(n+2)} \epsilon^2 + \mathcal{O}(\epsilon^3) \right).$$

Weyl tensor. Another important tensor field of rank $(0, 4)$ is the Weyl tensor, which is obtained as the “trace-free” part of the Riemann tensor. Physically, the Weyl tensor describes the tidal force experienced by a body when moving along geodesics, and quantifies the shape distortion a body experiences due to tidal forces (e.g., water tides caused by the gravitational pull of the moon). In an n -dimensional manifold it is defined as:

$$\begin{aligned} C_{\alpha\beta\gamma\delta} &= R_{\alpha\beta\gamma\delta} - \frac{1}{(n-2)} \left(R_{\alpha\delta} g_{\beta\gamma} - R_{\alpha\gamma} g_{\beta\delta} + R_{\beta\gamma} g_{\alpha\delta} - R_{\beta\delta} g_{\alpha\gamma} \right) \\ &+ \frac{1}{(n-1)(n-2)} R (g_{\alpha\gamma} g_{\beta\delta} - g_{\alpha\delta} g_{\beta\gamma}). \end{aligned} \quad (62)$$

Mathematically, the Weyl tensor corresponds to the only non-zero components of the Riemann tensor when looking at *Ricci-flat* manifolds, i.e. $R_{\alpha\beta} = 0$. This becomes relevant for e.g., vacuum solutions, a class of exact solutions where $R_{\alpha\beta} = 0$ of the Einstein equations in the absence of matter distribution.

Curvature invariants. Curvature invariants play a central role in the analysis of spacetime geometries in general relativity. These scalar quantities are constructed from contractions of curvature tensors and are manifestly invariant under general coordinate transformations. As such, they serve as powerful diagnostic tools for characterizing the local and global geometric and physical properties of spacetime, which includes the identification of “true” (genuine spacetime singularities) and “false” singularities (artifact of choice of coordinate charts).

Among the most prominent quadratic curvature invariants that is relevant to our simulations and features in our paper is the *Kretschmann scalar*, defined as the full contraction of the Riemann curvature tensor with itself:

$$\mathcal{K}(x) := R^{\alpha\beta\gamma\delta}(x)R_{\alpha\beta\gamma\delta}(x) = g^{\alpha\rho}(x)g^{\beta\sigma}(x)g^{\gamma\zeta}(x)g^{\delta\eta}(x)R_{\rho\sigma\zeta\eta}(x)R_{\alpha\beta\gamma\delta}(x). \quad (63)$$

The Kretschmann scalar provides a coordinate-independent measure of the magnitude of the curvature of spacetime and the singularity becomes blows-up, due to infinite curvature. Examples are Kretschmann scalars \mathcal{K} for blackholes, and Weyl scalars Ψ_4 for gravitational wave astrophysics. They capture the presence of intrinsic curvatures even when the Ricci tensor itself vanishes. Thus, the Kretschmann scalar encodes geometric information in a frame-independent manner.

B.3.7 Stress-energy-momentum tensor

The stress-energy-momentum tensor (or simply called the energy-momentum tensor) is a symmetric rank $(2, 0)$ tensor

$$T^{\alpha\beta} = T^{\alpha\beta}e_\alpha \otimes e_\beta. \quad (64)$$

Physically, $T^{\alpha\beta}$ is a generalization of the stress tensor in continuum and fluid mechanics. It stores the information of distribution of matter fields, i.e., sources or sinks as a 4×4 tensor, such as energy-density, energy-flux, momentum density, and momentum flux.

These matter fields satisfy the conservation laws, i.e., conservation of mass and energy via the four-dimensional *continuity equation* and corresponds to the *divergence-free* condition of the energy-momentum tensor

$$\nabla_\alpha T^{\alpha\beta}(x) = 0. \quad (65)$$

The stress-energy-momentum tensor features on the right hand side of the Einstein field equations, and influences spacetime geometry by causing distortions on it.

B.4 Einstein field equations

The Einstein field equations (EFEs) are a set of second-order non-linear PDEs containing geometry on the left hand side and the source on the right hand side. EFEs are obtained by combining all the differential geometric quantities from Equations ((36), (60), (61), (64)), together with the conservation laws for matter distribution of Equation (65), resulting in

$$G_{\alpha\beta} = 8\pi G T_{\alpha\beta}. \quad (66)$$

Here, $G_{\alpha\beta} := R_{\alpha\beta} - \frac{1}{2}g_{\alpha\beta}R + \Lambda g_{\alpha\beta}$ is called the *Einstein tensor* and also satisfies the divergence-free condition $\nabla_\alpha G^{\alpha\beta} = 0$, which, is a consequence of the IIInd Bianchi identity of Equation (58b).

B.4.1 Coordinate-independence of GR

Fundamentally, GR posits a deeper symmetry class: *diffeomorphism covariance* [17]. It asserts that the laws of physics are independent of any particular choice of coordinates or parametrization of the underlying smooth manifold. For example, the metric around the star, say sun, can be expressed in terms of the Schwarzschild metric (introduced in Section C.1). Here, the diffeomorphism acts as a gauge transformation [45] between two sets of metrics defined on the Lorentzian manifold \mathcal{M} , in this case an equivalence class of Lorentzian metrics $\text{Riem}(\mathcal{M})$ describing the same spacetime geometry. This makes sure equations of motion, conservation laws, physical fields, etc. remain intact, hence, the term “covariance”. In mathematical terms, Let, $\Phi \in \text{Diff}(\mathcal{M})$ be a smooth, invertible map between \mathcal{M} with a smooth inverse, $\Phi : \mathcal{M} \xrightarrow{\cong} \mathcal{M}$ such that:

$$(\Phi^* g)(v, w) := g(\Phi_*(v), \Phi_*(w)). \quad (67)$$

Here, $\Phi_* : T\mathcal{M} \rightarrow T\mathcal{M}$, is the pushforward map defined on the tangent bundles. This means under diffeomorphisms the metric transforms via a pullback operation $\Phi^* g = g'$. I.e., $\bar{g}_{\alpha\beta}(\bar{x}) = \frac{\partial x^\mu}{\partial \bar{x}^\alpha} \frac{\partial x^\nu}{\partial \bar{x}^\beta} g_{\mu\nu}(x)$ are gauge equivalent. Additionally, GR also admits changes of local frames or bases (external symmetries) via the *general linear group* $GL(4, \mathbb{R})$, i.e., invertible linear transformations at each point $p \in \mathcal{M}$. Thus, GR enjoys coordinate independence from two symmetry transformations, i.e., (i) between any particular choice of coordinates or parameterization of the underlying smooth manifold \mathcal{M} , and (ii) general linear group transformations that locally change frames of reference.

C Exact Solutions of the Einstein Field Equations

This Appendix contains a detailed description of the exact solutions of EFEs corresponding to a class of metrics $g_{\mu\nu}$ that are solutions of Equation (66). While there exist several geometries that satisfy the EFEs, we shall consider three prominent geometries: the Schwarzschild metric, the Kerr metric, and gravitational waves. These solutions not only have a high theoretical and historical relevance, but are also of great interest in computational black hole astrophysics and gravitational wave and multi-messenger astronomy. From here on, we work in naturalized units by setting $c = G = 1$.

Our work predominantly uses the exact solutions for generating synthetic training data, which are analytic expressions for (i) Schwarzschild, (ii) Kerr, and (iii) linearized gravity metrics, on which we fit the NeFs.

C.1 Schwarzschild metric

The Schwarzschild metric is the simplest non-trivial solution to the EFEs. It describes the geometry around a non-rotating spherical body, such as a star or a black hole, constituting spherically symmetric vacuum solutions, i.e., $T_{\mu\nu} = 0$. A famous result of GR called the Birkhoff's theorem [46] proves that any spherically symmetric vacuum solution corresponds to a static (non-rotating), time-independent (stationary), and asymptotically flat metric (i.e., for $r \rightarrow \infty$ the metric converges to the flat Minkowski spacetime), and must essentially be equivalent to the Schwarzschild solution.

C.1.1 Coordinate systems for Schwarzschild metrics

Spherical polar coordinates. Schwarzschild solution is typically written in the conventional spherical polar coordinates (t, r, θ, ϕ) where $t \in \mathbb{R}$, $r \in \mathbb{R}^+$, $\theta \in (0, \pi)$, and $\phi \in [0, 2\pi)$. The metric can be written either using the quadratic line element

$$ds^2 = -\left(1 - \frac{2M}{r}\right)dt^2 + \left(1 - \frac{2M}{r}\right)^{-1}dr^2 + r^2(d\theta^2 + \sin^2\theta d\phi^2). \quad (68)$$

or in the equivalent matrix notation

$$g_{\mu\nu}^{\text{Sph}} = \begin{pmatrix} -\left(1 - \frac{2M}{r}\right) & 0 & 0 & 0 \\ 0 & \left(1 - \frac{2M}{r}\right)^{-1} & 0 & 0 \\ 0 & 0 & r^2 & 0 \\ 0 & 0 & 0 & r^2 \sin^2\theta \end{pmatrix}. \quad (69)$$

The true singularity of the Schwarzschild metric is at the origin and can be identified from the divergent Kretschmann scalar (Eq. (63)):

$$\mathcal{K}(r) = \frac{48M^2}{r^6} \xrightarrow{r \rightarrow 0} \infty. \quad (70)$$

Although a (fake) coordinate singularity exists at $r = r_s = 2M$, where the Kretschmann scalar is well defined. This special radius r_s is called the Schwarzschild radius. It demarcates the location of the *event horizon* of a non-rotating black hole and delineates a region from which no causal signal can escape to asymptotic infinity, meaning, it is a point of no return for any body (including light) once it crosses this critical radius.

Cartesian Kerr-Schild coordinates. The Kerr-Schild (KS) form is a beneficial representation for finding exact solutions to the EFEs. These are perturbative corrections to a spacetime metric only upto the linear order [47]. The KS form enables the following simplifications to the nonlinear field equations : (i) It expresses the resultant metric as a linearized perturbation to the background metric, and (ii) gets rid of the coordinate singularities, which are mere artifacts of an unsuitable choice of coordinate systems. The corresponding line element expressed in the KS form reads

$$ds^2 = (\bar{g}_{\alpha\beta} + V(x)\ell_\alpha\ell_\beta)dx^\alpha dx^\beta, \quad (71)$$

where $\bar{g}_{\alpha\beta}$ is some background metric, l_α are the components of a null vector ℓ with respect to the background metric and $V(x)$ is a scalar.

For a spherically symmetric non-rotating blackhole such as Schwarzschild, the Cartesian Kerr-Schild line element is obtained by setting $\bar{g}_{\alpha\beta} = \eta_{\alpha\beta}$, $\ell = \left(1, \frac{x}{r}, \frac{y}{r}, \frac{z}{r}\right)$ and $V = \frac{2M}{r}$:

$$ds^2 = -dt^2 + dx^2 + dy^2 + dz^2 + \frac{2M}{r} \left[dt + \frac{x}{r} dx + \frac{y}{r} dy + \frac{z}{r} dz \right]^2. \quad (72)$$

Unlike the spherical coordinate form in Equation (68), $r = 2M$ is not singular, hence removing the coordinate singularities. The metric tensor components read:

$$g_{\mu\nu}^{\text{KS}} = \begin{pmatrix} -1 + 2M/r & \frac{2Mx}{r^2} & \frac{2My}{r^2} & \frac{2Mz}{r^2} \\ \frac{2Mx}{r^2} & 1 + \frac{2Mx^2}{r^3} & \frac{2Mxy}{r^3} & \frac{2Mxz}{r^3} \\ \frac{2My}{r^2} & \frac{2Mxy}{r^3} & 1 + \frac{2My^2}{r^3} & \frac{2Myz}{r^3} \\ \frac{2Mz}{r^2} & \frac{2Mxz}{r^3} & \frac{2Myz}{r^3} & 1 + \frac{2Mz^2}{r^3} \end{pmatrix}. \quad (73)$$

(74)

Ingoing (advanced) Eddington-Finkelstein coordinates The ingoing version of the Eddington-Finkelstein (EF) coordinates is obtained by replacing time t with an advanced time coordinate $v = t + r_*(r)$, where $r_* = r + M \log \left| \frac{r-2M}{2M} \right|$. Thus, dt in these transformed coordinates amounts to:

$$dt = dv - dr_* = dv - \left(1 - \frac{2M}{r}\right)^{-1} dr$$

The ingoing EF version of the Schwarzschild metric reads:

$$ds^2 = -\left(1 - \frac{2M}{r}\right) dv^2 + 2dv dr + r^2 (d\theta^2 + \sin^2\theta d\phi^2), \quad (75)$$

With the metric tensor being:

$$g_{\mu\nu}^{\text{EF}} = \begin{pmatrix} -\left(1 - \frac{2M}{r}\right) & 1 & 0 & 0 \\ 1 & 0 & 0 & 0 \\ 0 & 0 & r^2 & 0 \\ 0 & 0 & 0 & r^2 \sin^2\theta \end{pmatrix}. \quad (76)$$

This metric is smooth (and non-degenerate), devoid of coordinate singularities at the event horizon $r = r_s = 2M$, and can be continued down to the curvature singularity at $r = 0$ [41, 48, 49].

C.2 Kerr metric

The Kerr solution describes a massive gravitating body rotating with an angular momentum J . From the physics perspective, it is not symmetric under time-reversal symmetry, i.e., $t \rightarrow -t$, hence corresponds to a stationary but a non-static solution [50]. Due to a finite angular momentum J , or equivalently, rotation parameter $a = \frac{J}{M} > 0$, the Kerr metric introduces an asymmetry, and is oblate. Thus, the Kerr metric corresponds to an oblate spheroid geometry.

C.2.1 Coordinate systems for Kerr metric

Boyer-Lindquist coordinates. The Boyer-Lindquist (BL) coordinates are a special and convenient representation for the Kerr metric [51, 52, 50]. The BL form (t, r, ϑ, ϕ) is described by oblate spheroidal coordinates [53]:

$$x = \sqrt{r^2 + a^2} \sin\vartheta \cos\phi \quad (77a)$$

$$y = \sqrt{r^2 + a^2} \sin\vartheta \sin\phi \quad (77b)$$

$$z = r \cos\vartheta. \quad (77c)$$

Notice that the zenith angle $\vartheta \neq \theta$ differs from the Schwarzschild case, while the azimuthal angle ϕ is the same in both. As $a \rightarrow 0$, the Kerr metric boils down to the non-rotating spherical case of the Schwarzschild metric.

$$ds^2 = -\left(1 - \frac{2Mr}{\Sigma}\right)dt^2 - \frac{4Mars\sin^2\vartheta}{\Sigma}dtd\phi + \frac{\Sigma}{\Delta}dr^2 + \Sigma d\vartheta^2 + \left(r^2 + a^2 + \frac{2Mra^2\sin^2\vartheta}{\Sigma}\right)\sin^2\vartheta d\phi^2, \quad (78)$$

where the length scales are $a = \frac{J}{M}$ (angular momentum per unit mass), $\Sigma \equiv r^2 + a^2\cos^2\vartheta$, and $\Delta \equiv r^2 - 2Mr + a^2$. The Kerr curvature singularity occurs at $\Sigma := r^2 + a^2\cos^2\vartheta = 0$, implying $r = 0$ and $\vartheta = \frac{\pi}{2}$. The metric tensor of Equation (78) is:

$$g_{\mu\nu}^{\text{BL}} = \begin{pmatrix} -\left(1 - \frac{2Mr}{\Sigma}\right) & 0 & 0 & -\frac{2Mar\sin^2\vartheta}{\Sigma} \\ 0 & \frac{\Sigma}{\Delta} & 0 & 0 \\ 0 & 0 & \Sigma & 0 \\ -\frac{2Mar\sin^2\vartheta}{\Sigma} & 0 & 0 & \left(r^2 + a^2 + \frac{2Ma^2r\sin^2\vartheta}{\Sigma}\right)\sin^2\vartheta \end{pmatrix}. \quad (79)$$

In the Boyer-Lindquist form of the metric, there also exist coordinate singularities at $\Delta = r^2 - 2Mr + a^2 = 0$. Thus, the roots of $\Delta = 0$ are $r_{\pm} = M \pm \sqrt{M^2 - a^2}$, which demarcate the outer and inner horizons.

It is easy to see the existence of a curvature singularity at $r = 0$ on the equatorial plane corresponding to the zenith angle $\vartheta = \frac{\pi}{2}$. Thus, unlike Schwarzschild, the singularity in Kerr geometry takes the form of a ring, also known as a *ring singularity*.

Cartesian Kerr-Schild coordinates. The Cartesian KS form of the Kerr metric is obtained by setting in Equation (71) $\ell = \left(1, \frac{rx+ay}{r^2+a^2}, \frac{ry-ax}{r^2+a^2}, \frac{z}{r}\right)$ and $V = \frac{mr^3}{r^4+a^2z^2}$ in Equation (71). The Kerr metric in Kerr coordinates are often used to write initial data for hydro simulations. The line-element in the Cartesian Kerr-Schild form reads [50]:

$$ds^2 = -dt^2 + dx^2 + dy^2 + dz^2 + \frac{2mr^3}{r^4 + a^2z^2} \left[dt + \frac{r(xdx + ydy)}{a^2 + r^2} + \frac{a(ydx - xdy)}{a^2 + r^2} + \frac{z}{r}dz \right]^2. \quad (80)$$

Here, $r \equiv r(x, y, z)$ is not a coordinate, and is given implicitly by solving the quadratic equation $\frac{x^2+y^2}{r^2+a^2} + \frac{z^2}{r^2} = 1$: The solution for the implicit function r is given by the discriminant [52]:

$$r^2(x, y, z) = \frac{x^2 + y^2 + z^2 - a^2}{2} + \sqrt{\frac{(x^2 + y^2 + z^2 - a^2)^2 + 4a^2z^2}{4}}.$$

The corresponding Cartesian coordinates are expressed as:

$$\begin{aligned} x &= (r \cos\varphi - a \sin\varphi)\sin\theta = \sqrt{r^2 + a^2} \sin\theta \cos(\varphi + \tan^{-1}(a/r)), \\ y &= (r \sin\varphi + a \cos\varphi)\sin\theta = \sqrt{r^2 + a^2} \sin\theta \sin(\varphi + \tan^{-1}(a/r)), \\ z &= r \cos\theta. \end{aligned}$$

In the BL coordinates the ring singularity for Kerr exists at $r = 0$ & $\vartheta = \frac{\pi}{2}$, translating to $z = 0$ (equatorial-plane), and the ring occurring at $x^2 + y^2 = a^2$. In contrast, the KS representation is devoid of *coordinate singularities*, making it suitable to work in numerics, especially around the event-horizons.

Ingoing Eddington-Finkelstein coordinates. In the original formulation, the Kerr metric is written in the advanced time coordinates/ingoing EF coordinates v . The line element in this representation reads [50]:

$$\begin{aligned} ds^2 = & -\left(1 - \frac{2Mr}{r^2 + a^2\cos^2\theta}\right)(dv + a \sin^2\theta d\tilde{\phi})^2 \\ & + 2(dv + a \sin^2\theta d\tilde{\phi})(dr + a \sin^2\theta d\tilde{\phi}) \\ & + (r^2 + a^2\cos^2\theta)(d\theta^2 + \sin^2\theta d\tilde{\phi}^2), \end{aligned} \quad (81)$$

where the ingoing EF coordinates are related to the Boyer-Lindquist coordinates Equation (77) by the following transformation:

$$v = t + \int \frac{(r^2 + a^2)}{\Delta} dr ,$$

$$\tilde{\phi} = \phi + a \int \frac{dr}{\Delta} ,$$

where, $\Delta \equiv r^2 - 2Mr + a^2$. and the metric tensor components corresponding to the line element is given by

$$g_{\mu\nu}^{\text{EF}} = \begin{pmatrix} -\left(1 - \frac{2Mr}{\Sigma}\right) & 1 & 0 & \frac{2Mar \sin^2 \theta}{\Sigma} \\ 1 & 0 & 0 & a \sin^2 \theta \\ 0 & 0 & \Sigma & 0 \\ \frac{2Mar \sin^2 \theta}{\Sigma} & a \sin^2 \theta & 0 & \left(r^2 + a^2 + \frac{2Ma^2r \sin^2 \theta}{\Sigma}\right) \sin^2 \theta \end{pmatrix} . \quad (82)$$

The coordinate (fake) singularities ($\mathcal{K} < \infty$) of the Kerr metric is given by the zeros of $\Delta \equiv r^2 - 2Mr + a^2 = 0$. Solving for the zeros, one finds

$$r_{\pm} = M \pm \sqrt{M^2 - a^2} ,$$

where, r_+ is the outer event horizon, while r_- demarcates the inner event horizon.

Apart from that, rotating metrics also possess a highly interesting region known as the *ergosphere*, which fundamentally captures the non-Euclidean and non-inertial nature of general relativistic effects induced by rotation. This domain is situated outside the outer event horizon r_+ , and is created owing to the frame-dragging (Lense-Thirring) effect. Consequently, no physical observer (test body) can remain static within the ergosphere and is compelled to co-rotate with the black hole depending on the value of a . The location of the ergosphere is given by

$$r_{\pm}^{\text{ergo}}(\vartheta) = M \pm \sqrt{M^2 - a^2 \cos^2 \vartheta} ,$$

where, r_+^{ergo} is the outer ergosphere, while r_-^{ergo} demarcates the inner ergosphere. In Figure (5), the following regions of the Kerr metric are demarcated:

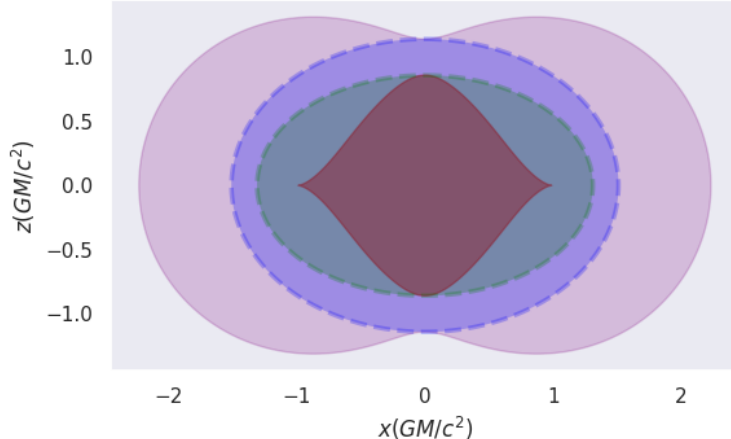


Figure 5: Kerr metric 2D slice in the x-z plane ($y = 0$) for a spin parameter $a = 0.99$. The following regions plotted are: i) inner ergosphere r_-^{ergo} : red region, ii) inner event-horizon r_- : green region, iii) outer event-horizon r_+ : blue region and iv) outer Ergosphere r_+^{ergo} : purple region.

C.2.2 Kretschmann scalar associated with Kerr solution

The nontrivial part of the Kretschmann invariant – refer Equation (63) for the Kerr metric reads:

$$R_{\alpha\beta\gamma\delta} R^{\alpha\beta\gamma\delta} = C_{\alpha\beta\gamma\delta} C^{\alpha\beta\gamma\delta} = \frac{48M^2(r^2 - a^2 \cos^2 \vartheta) [(r^2 + a^2 \cos^2 \vartheta)^2 - 16r^2 a^2 \cos^2 \vartheta]}{(r^2 + a^2 \cos^2 \vartheta)^6} . \quad (83)$$

This guarantees that the curvature singularity ($\mathcal{K} \rightarrow \infty$) occurs at the ring $\Sigma \equiv r^2 + a^2 \cos^2 \vartheta = 0$, with zeros at:

$$r = 0 , \text{ and, } \vartheta = \frac{\pi}{2} .$$

C.3 Gravitational waves

Linearized gravity models the metric as tiny fluctuations or *perturbations* $h_{\alpha\beta}$ of the flat background metric $\eta_{\alpha\beta}$:

$$g_{\alpha\beta} \approx \eta_{\alpha\beta} + h_{\alpha\beta} + \mathcal{O}(h_{\alpha\beta})^2,$$

where $|h_{\alpha\beta}| \ll 1$. To describe gravitational wave propagation, it is often convenient to reduce the linearized field equations into a simplified form via two *gauge fixing* conditions, namely, a) *harmonic gauge*, and b) *transverse-traceless* (TT) gauge. Thus, the Einstein field equations for gravitational waves assume a succinct wave equation type form:

$$\square \bar{h}_{\alpha\beta}^{(\epsilon)} = -16\pi T_{\alpha\beta}.$$

Here, $\bar{h}_{\alpha\beta}^{(\epsilon)} = h_{\alpha\beta}^{(\epsilon)} - \frac{1}{2}h^{(\epsilon)}\eta_{\alpha\beta}$ and $\square \equiv \eta^{\alpha\beta}\partial_\alpha\partial_\beta$ is the d'Alembert operator (wave operator). It can be shown that the PDEs in Equation (C.3) produce gravitational wave solutions.

The transverse-traceless (TT) perturbation (we drop the superscript (ϵ) for the sake of ease) satisfies the following conditions:

Transverse: $\partial_\beta h^{\text{TT}\alpha\beta} = 0$, i.e., wave propagates perpendicular to perturbation direction,

Traceless: $h^{\text{TT}\alpha\alpha} = 0$,

Purely spatial: $h_{0\alpha}^{\text{TT}} = 0$, i.e., no time components.

Thus, a gravitational wave propagating in the z -direction with frequency ω is given in the TT gauge as:

$$h_{\alpha\beta}^{\text{TT}} = \begin{pmatrix} 0 & 0 & 0 & 0 \\ 0 & h_+ & h_\times & 0 \\ 0 & h_\times & h_+ & 0 \\ 0 & 0 & 0 & 0 \end{pmatrix} \cos(\omega(t-z)). \quad (84)$$

h_+ and h_\times are the amplitudes of the “+” (plus) polarization and “ \times ” (cross) polarization.

The complete metric tensor in the linearized gravity setting is given by:

$$g_{\alpha\beta} = \eta_{\alpha\beta} + h_{\alpha\beta}^{\text{TT}} = \begin{pmatrix} -1 & 0 & 0 & 0 \\ 0 & 1 + h_+ \cos(\omega(t-z)) & h_\times \cos(\omega(t-z)) & 0 \\ 0 & h_\times \cos(\omega(t-z)) & 1 + h_+ \cos(\omega(t-z)) & 0 \\ 0 & 0 & 0 & 1 \end{pmatrix}. \quad (85)$$

The corresponding line-element in the linearized gravity setting reads:

$$ds^2 = -dt^2 + [1 + h_+ \cos(\omega(t-z))] dx^2 + [1 - h_+ \cos(\omega(t-z))] dy^2 + 2h_\times \cos(\omega(t-z)) dx dy \quad (86)$$

Spin-weighted spherical harmonics (SWSH) metric representation. We start from the decomposition of the complex gravitational wave strain with the spherical harmonic basis-set expansion [54]. With the expansion in mode weights $h^{\ell m}(t, r)$, one can ignore (remove) the angular dependence:

$$h(t, r, \theta, \phi) = h_+(t, r, \theta, \phi) - i h_\times(t, r, \theta, \phi) = \frac{M}{r} \sum_{\ell=|s|}^{\infty} \sum_{|m| \leq \ell} h^{\ell m}(t) {}_{-2}Y_{\ell m}(\theta, \phi), \quad (87)$$

where, $h(t, r, \theta, \phi) = h_+(t, r, \theta, \phi) - i h_\times(t, r, \theta, \phi)$ is the complex strain. Thus, for each orbital and azimuthal indices (ℓ, m) , one can extract the mode $h^{\ell m}(t)$ at a fixed radius r , one uses the orthogonality of the spin-weighted spherical harmonics (SWSHs) elements:

$$\frac{r}{M} h^{\ell m}(t) = \int_0^{2\pi} \int_0^\pi h(t, r, \theta, \phi) {}_{-2}\bar{Y}_{\ell m}(\theta, \phi) d\Omega \quad (88)$$

where, $d\Omega = \sin\theta d\theta d\phi$ is the spherical volume element and ${}_{-2}\bar{Y}_{\ell m}$ denotes the complex conjugate of the $s = 2 - n = -2$ where ($n = 4$ for Ψ_4) spin-weighted spherical harmonics. One typically carries out the integral over the 2-sphere \mathbb{S}^2 numerically on a finite angular grid.

The general formula for SWSHs is:

$${}_s Y_{\ell m}(\theta, \phi) = (-1)^{l+m-s} \left[\frac{2\ell+1}{4\pi} \frac{(\ell+m)!(\ell-m)!}{(\ell+s)!(\ell-s)!} \right]^{1/2} \sin^{2\ell} \left(\frac{\theta}{2} \right) e^{im\phi} \sum_{r=0}^{\ell-s} (-1)^r \binom{\ell-s}{r} \binom{\ell+s}{r+s-m} \cot^{2r+s-m} \left(\frac{\theta}{2} \right). \quad (89)$$

where the parameters ℓ, m are the familiar Laplace spherical harmonics (orbital-angular momentum and azimuthal indices), while s is the additional spin-weight introduced by some underlying gauge group such as $U(1)$. We especially plot for the integers $s = -2, l = m = 2$, since they are relevant for GWs and are depicted in Figure 6.

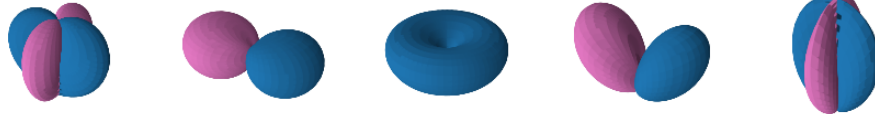


Figure 6: Spin weighted spherical harmonics for $s = -2$, and $l = 2$ for $|m| \leq l$. The dominant contributions for the Weyl scalar Ψ_4 and the associated metric coefficients in the spherical harmonic basis $h^{2,\pm 2}(t)$ are shown.

C.4 Minkowski metric

C.4.1 Coordinate systems for Minkowski metric

The flat Minkowski metric, which is a spacetime that has no curvature ($M \rightarrow 0$) can be expressed in other coordinate systems as well.

Spherical polar coordinates. In spherical coordinates $(t, r, \vartheta, \varphi)$, the Minkowski metric is described by the quadratic line element,

$$ds^2 = -c^2 dt^2 + dr^2 + r^2(d\vartheta^2 + \sin^2 d\varphi^2) \quad (90)$$

here, $r \in \mathbb{R}^+$, $\vartheta \in (0, \pi)$, and, $\phi \in [0, 2\pi)$ are the usual spherical polar coordinates. Thus, the metric tensor describing the Schwarzschild solution reads:

$$\eta_{\mu\nu}^{\text{Sph}} = \begin{pmatrix} -1 & 0 & 0 & 0 \\ 0 & 1 & 0 & 0 \\ 0 & 0 & r^2 & 0 \\ 0 & 0 & 0 & r^2 \sin^2 \theta \end{pmatrix} \quad (91)$$

Boyer-Lindquist coordinates. Setting $M \rightarrow 0$ in the Boyer-Lindquist form of the Kerr metric (78), the corresponding line element reduces to an unfamiliar “oblate-spheroidal” representation:

$$ds^2 = -dt^2 + \frac{r^2 + a^2 \cos^2 \vartheta}{r^2 + a^2} dr^2 + (r^2 + a^2 \cos^2 \vartheta) d\vartheta^2 + (r^2 + a^2) \sin^2 \vartheta d\varphi^2, \quad (92)$$

and the components of the

$$\eta_{\mu\nu}^{\text{BL}} = \begin{pmatrix} -1 & 0 & 0 & 0 \\ 0 & \frac{r^2 + a^2 \cos^2 \vartheta}{r^2 + a^2} & 0 & 0 \\ 0 & 0 & r^2 + a^2 \cos^2 \vartheta & 0 \\ 0 & 0 & 0 & (r^2 + a^2) \sin^2 \vartheta \end{pmatrix}. \quad (93)$$

The usual Cartesian coordinates can be related to the oblate spheroid ones via:

$$\begin{aligned} x &= \sqrt{r^2 + a^2} \sin \vartheta \cos \phi \\ y &= \sqrt{r^2 + a^2} \sin \vartheta \sin \phi \\ z &= r \cos \vartheta. \end{aligned}$$

Eddington-Finkelstein coordinates. The Minkowski metric can be written in the ingoing (advanced) Eddington-Finkelstein form in two different cases, namely for the non-rotating and the rotating case.

- i) non-rotating, $a \rightarrow 0$ (Schwarzschild): :

$$ds^2 = -dv^2 + 2dv\,dr + r^2(d\theta^2 + \sin^2\theta\,d\phi^2),$$

and the metric tensor reads:

$$\eta_{\mu\nu}^{\text{EF}} = \begin{pmatrix} -1 & 1 & 0 & 0 \\ 1 & 0 & 0 & 0 \\ 0 & 0 & r^2 & 0 \\ 0 & 0 & 0 & r^2 \sin^2\theta \end{pmatrix}. \quad (94)$$

- ii) rotating: $a > 0$ (Kerr):

$$\begin{aligned} ds^2 = & -(dv + a \sin^2\theta d\phi)^2 + 2(dv + a \sin^2\theta d\phi)(dr + a \sin^2\theta d\phi) \\ & + (r^2 + a^2 \cos^2\theta)(d\theta^2 + \sin^2\theta d\phi^2), \end{aligned} \quad (95)$$

and the metric tensor reads:

$$\eta_{\mu\nu}^{\text{EF}} = \begin{pmatrix} -1 & 1 & 0 & 0 \\ 1 & 0 & 0 & a \sin^2\theta \\ 0 & 0 & \Sigma & 0 \\ 0 & a \sin^2\theta & 0 & (r^2 + a^2) \sin^2\theta \end{pmatrix}. \quad (96)$$

C.5 Training on non-trivial metric fields (distortions)

Distortion part of Schwarzschild geometry in spherical coordinates:

- **Spherical coordinates:** obtained by subtracting (91) from (69):

$$g_{\mu\nu}^{\text{Sph}} - \eta_{\mu\nu}^{\text{Sph}} = \begin{pmatrix} \frac{r_s}{r} & 0 & 0 & 0 \\ 0 & \frac{r_s}{(r - r_s)} & 0 & 0 \\ 0 & 0 & 0 & 0 \\ 0 & 0 & 0 & 0 \end{pmatrix}. \quad (97)$$

- **Kerr-Schild coordinates** obtained by subtracting $\eta_{\mu\nu} = \text{diag}(-1, +1, +1, +1)$ from (73):

$$g_{\mu\nu}^{\text{KS}} - \eta_{\mu\nu} = \begin{pmatrix} \frac{2M}{r} & \frac{2Mx}{r^2} & \frac{2My}{r^2} & \frac{2Mz}{r^2} \\ \frac{2Mx}{r^2} & \frac{2Mx^2}{r^3} & \frac{2Mxy}{r^3} & \frac{2Mxz}{r^3} \\ \frac{2My}{r^2} & \frac{2Mxy}{r^3} & \frac{2My^2}{r^3} & \frac{2Myz}{r^3} \\ \frac{2Mz}{r^2} & \frac{2Mxz}{r^3} & \frac{2Myz}{r^3} & \frac{2Mz^2}{r^3} \end{pmatrix}. \quad (98)$$

- **Ingoing Eddington-Finkelstein coordinates** obtained by subtracting (94) from (76):

$$g_{\mu\nu}^{\text{EF}} - \eta_{\mu\nu}^{\text{EF}} = \begin{pmatrix} \frac{r_s}{r} & 0 & 0 & 0 \\ 0 & 0 & 0 & 0 \\ 0 & 0 & 0 & 0 \\ 0 & 0 & 0 & 0 \end{pmatrix}. \quad (99)$$

Distortion part of Kerr geometry:

- **Boyer-Lindquist coordinates:** obtained by subtracting (93) from (79):

$$g_{\mu\nu}^{\text{BL}} - \eta_{\mu\nu}^{\text{BL}} = \begin{pmatrix} \frac{2Mr}{\Sigma} & 0 & 0 & \frac{2Mar \sin^2 \theta}{\Sigma} \\ 0 & \frac{2M\Sigma}{r\Delta} & 0 & 0 \\ 0 & 0 & 0 & 0 \\ \frac{2Mar \sin^2 \theta}{\Sigma} & 0 & 0 & \frac{2Ma^2r \sin^4 \vartheta}{\Sigma} \end{pmatrix}. \quad (100)$$

- **Kerr-Schild coordinates:** obtained by subtracting $\eta = \text{diag}(-1, +1, +1, +1)$ from Equation (80):
- **Eddington-Finkelstein coordinates:** obtained by subtracting (96) from (82):

$$g_{\mu\nu}^{\text{EF}} - \eta_{\mu\nu}^{\text{EF}} = \begin{pmatrix} \frac{2Mr}{\Sigma} & 0 & 0 & \frac{2Mar \sin^2 \theta}{\Sigma} \\ 0 & 0 & 0 & 0 \\ 0 & 0 & 0 & 0 \\ \frac{2Mar \sin^2 \theta}{\Sigma} & 0 & 0 & \frac{2Ma^2r \sin^4 \vartheta}{\Sigma} \end{pmatrix}. \quad (101)$$

D Finite-Difference Method (FDM) for Tensor Differentiation

The main concept in this appendix section details numerical differentiation methods for tensor-valued quantities, focusing on the practical use of higher-order finite-difference schemes (in particular, sixth-order stencils). We outline the treatment of discretization errors and the use of neighboring grid collocation points as part of a numerical tensor calculus toolbox.

To compare the performance against automatic differentiation on tensor fields defined on the four dimensional spacetime, throughout the paper we opt for the highly accurate sixth-order order *forward difference* ($n = 6$ accuracy). This scheme queries six neighboring points per evaluation and the general formula of the differential operators are given by:

$$\begin{aligned} [\partial_{x^i} f(\mathbf{x})] \approx & -\frac{49}{20h} f(\mathbf{x}) + \frac{6}{h} f(\mathbf{x} + \mathbf{h}) - \frac{15}{2h} f(\mathbf{x} + 2\mathbf{h}) + \frac{20}{3h} f(\mathbf{x} + 3\mathbf{h}) \\ & - \frac{15}{4h} f(\mathbf{x} + 4\mathbf{h}) + \frac{6}{5h} f(\mathbf{x} + 5\mathbf{h}) - \frac{1}{6h} f(\mathbf{x} + 6\mathbf{h}) + \mathcal{O}(h^7) \end{aligned} \quad (102)$$

Here, $\mathbf{x} = (x_1, \dots, x_d) \in \mathbb{R}^d$ and the $\mathbf{h} = h\mathbf{e}_i$, s.t. $\mathbf{e}_i = (0, \dots, \underbrace{h}_{i\text{-th index}}, \dots, 0)$, depending with respect to the variable x_i the partial derivative is performed over. Thus, this is accurate upto $\mathcal{O}(h^6)$, and the truncation error occurs at seventh-order.

In general, for an n -th order finite-difference approximation, the stencil is constructed by querying n neighboring collocation points on the voxel grid. The resulting truncation error on function evaluated on the grid (gridfunctions) scales as follows [55]:

$$\mathcal{E}_{\text{FD}}^n[f] = \mathcal{O}(h^n |\partial_{\mathbf{x}}^{n+1} f|).$$

Thus, higher order stencils enable larger step size h choices since the error scales exponential to the stencil order, i.e, $\mathcal{E} \propto h^n$. This results in not only better accuracy, but also lesser memory consumption due to lower grid resolution.

Finite-difference method bottlenecks in NR

- Higher-order finite-difference stencils require a collection of padded grid points exterior to the cube as boundary handling. These are often called ghost cells (zones). For e.g., if n_g ghost cells are required for the n -th order forward difference stencil, the grid size increases of a 3D spatial voxel grid [55] $\mathbb{N}_x \times \mathbb{N}_y \times \mathbb{N}_z \rightarrow (\mathbb{N}_x + n_g) \times (\mathbb{N}_y + n_g) \times (\mathbb{N}_z + n_g)$.
- Sensitive to numerical noise especially for tensor-valued functions defined on multidimensional voxel grids.

Comparing AD vs FD based methods. We quantify the performance of automatic-differentiation operations on the ground truth metric against the 6-th order finite difference stencils. We test it against the Kretschmann scalar $\mathcal{K} = R_{\alpha\beta\gamma\delta}R^{\alpha\beta\gamma\delta}$, which is prone to errors, especially due to floating point errors accumulated in the Riemann curvature tensor:

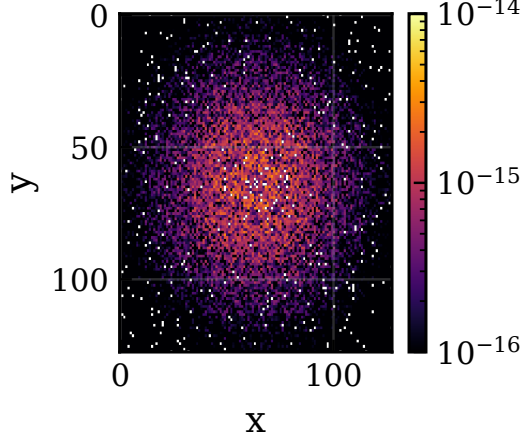


Figure 7: Absolute error $|\mathcal{K}_{\text{analytic}} - \mathcal{K}_{\text{AD}}|$ profile plotted for $z = 0.3$ between the analytic Kretschmann scalar and the ground truth Kretschmann scalar obtained via AD implemented on the ground truth (analytic) metric.

E Implicit neural representations (neural fields)

A *neural field* (NeF), also called an implicit neural representation or coordinate-based network, is a neural network that models a continuous signal over some domain, such as material density in 3D. Typically implemented as multilayer perceptrons [56], NeFs provide memory-efficient, high-fidelity approximations that can be queried at arbitrary resolutions and differentiated via automatic differentiation (AD). Unlike discrete representations (voxels, meshes), NeFs naturally handle sparse or irregular samples and have become central in vision tasks such as scene reconstruction [28, 29], shape modeling [13–15], and compression of images, video, and audio [57, 58]. For surveys see Xie et al. [27], Essakine et al. [59], Papa et al. [60].

Beyond vision, NeFs are increasingly applied in the sciences, including molecular dynamics [61], acoustic inverse problems [62], and PDE forecasting [63]. When combined with physics-informed losses, they serve as PDE solvers, known as physics-informed neural networks (PINNs) [36, 64, 65]. NeFs have also been used in differential geometry to represent smooth implicit surfaces and compute normals or curvatures via AD [66–68].

Applications to gravitational problems are emerging. Izzo and Gómez [69] trained NeFs under Newtonian gravity to infer the interior structure of small bodies from orbital acceleration data. Smith et al. [70] modeled Earth’s gravitational potential field $\phi(x, y, z)$ for geophysics, enabling interpolation of scattered measurements and gradient queries corresponding to gravitational acceleration. In relativistic contexts, PINNs have been explored for solving the Teukolsky equation [71] and for parameter estimation by learning metric components of analytic EFEs [72].

F Succinct Introduction to General Relativity, Equations of Motion and Exact Solutions

Derivative operators. The metric and its partial derivatives can be used to construct the Christoffel symbols

$$\Gamma_{\mu\nu}^\rho(x) := \frac{1}{2}g^{\rho\sigma}(\partial_\mu g_{\sigma\nu}(x) + \partial_\nu g_{\sigma\mu}(x) - \partial_\sigma g_{\mu\nu}(x)).$$

The Christoffel symbols denote how the metric varies across spacetime and define a parallel transport machinery to translate tensor fields around the manifold. With these, it is possible to construct two pivotal modified tensor differentiation operators, namely: (i) The *covariant derivative* (also called the *Levi-Civita connection*), which can be seen as a “calibration” of the partial derivative operator for parallel transportation in the curvilinear

setting:

$$\nabla_\mu T^{\alpha_1 \dots \alpha_r}_{\beta_1 \dots \beta_s} = \frac{\partial}{\partial x^\mu} T^{\alpha_1 \dots \alpha_r}_{\beta_1 \dots \beta_s} + \sum_{i=1}^r \Gamma^{\alpha_i}_{\mu\sigma} T^{\alpha_1 \dots \sigma \dots \alpha_r}_{\beta_1 \dots \beta_s} - \sum_{j=1}^s \Gamma^\sigma_{\mu\beta_j} T^{\alpha_1 \dots \alpha_r}_{\beta_1 \dots \sigma \dots \beta_s},$$

(ii) The *Lie derivative*, which generalizes the notion of a directional derivative that is connection independent (cf. Appendix B.3.4). The Lie derivative captures infinitesimal dragging of the tensor field along the flow generated by the vector field ξ :

$$(\mathcal{L}_\xi T)^{\alpha_1 \dots \alpha_r}_{\beta_1 \dots \beta_s} = \xi^\mu \partial_\mu T^{\alpha_1 \dots \alpha_r}_{\beta_1 \dots \beta_s} - \sum_{i=1}^r T^{\alpha_1 \dots \mu \dots \alpha_r}_{\beta_1 \dots \beta_s} \partial_\mu \xi^{\alpha_i} + \sum_{j=1}^s T^{\alpha_1 \dots \alpha_r}_{\beta_1 \dots \mu \dots \beta_s} \partial_{\beta_j} \xi^\mu.$$

Differential geometric objects. Using the modified derivatives, we can construct a hierarchy of higher-rank differential geometric quantities, such as the Riemannian curvature tensor $R^\delta_{\alpha\beta\gamma}$ or the Ricci tensor $R_{\alpha\beta}$, via a series of derivatives ∂ , covariant derivatives $\nabla := \partial + \Gamma$, and tensor index contractions $\mathcal{C} : \mathcal{V}_{s+1}^{r+1} \rightarrow \mathcal{V}_s^r$ (typically, Tr_g).

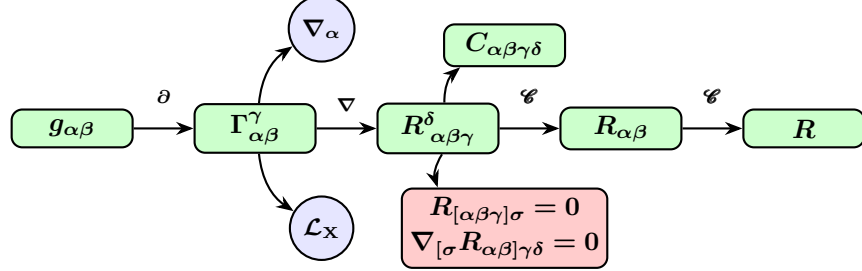


Figure 8: Differential geometry workflow in general relativity (only lhs of Equation (2)): We describe each quantity starting left: The metric tensor $g_{\alpha\beta}$ defines the spacetime geometry. Its partial derivatives ∂ yield the Christoffel symbols $\Gamma_{\alpha\beta}^\gamma$, which describe the notion of parallel transport and defines a covariant derivative operation $\nabla_\alpha = \partial_\alpha + \Gamma_\alpha$. The connection also defines the Lie derivative \mathcal{L}_v along vector fields v . The connection's derivatives ∇ give the Riemann curvature tensor $R_{\alpha\beta\gamma}^\delta$, which encodes tidal forces. The contraction operator $\mathcal{C} = \text{Tr}_g$ contracts with the metric, producing the trace part, i.e., the Ricci tensor $R_{\alpha\beta}$. Its subsequent contraction yields the Ricci scalar R . The Riemann tensor further splits into the Weyl tensor $C_{\alpha\beta\gamma\delta}$ (trace-free curvature part) and satisfies the algebraic and differential Bianchi identities $R_{[\alpha\beta\gamma]\sigma} = 0$ and $\nabla_{[\sigma} R_{\alpha\beta]\gamma\delta} = 0$. Together, these geometric objects form the backbone of general relativity, ultimately entering the Einstein field equations through the Einstein tensor $G_{\alpha\beta}$.

Conservation laws. It follows from the contracted *Bianchi identities*, i.e., cyclic sum of Riemann curvature tensor covariant derivatives (II Bianchi identity – see Equation (58b)) vanishes identically:

$$\nabla_\alpha R_{\beta\gamma\delta\sigma} + \nabla_\beta R_{\gamma\alpha\delta\sigma} + \nabla_\gamma R_{\alpha\beta\delta\sigma} = 0.$$

This is a geometric identity that holds for any (torsion-free) connection compatible with the metric. The identity above consequently leads to the covariant derivative of the stress-energy tensor vanishing, that is, $\nabla_\beta T^{\alpha\beta} := 0$ (see Equation (65)), which corresponds to the energy-momentum conservation in general relativity. If required, conservation laws typically feature as soft constraints in PDEs, and are relevant especially when matter distribution/fields are considered.

Equations of motion. The *geodesic equation* is a central second-order ODE that describes the motion of objects following geodesic paths in the curved spacetime background

$$\frac{d^2 x^\mu}{d\tau^2} + \Gamma^\mu_{\rho\sigma} \frac{dx^\rho}{d\tau} \frac{dx^\sigma}{d\tau} = 0.$$

Here, $\tau \in \mathbb{R}$ is some affine parameter (often the *proper time*; not to be confused with the coordinate time t). The geodesic equation is the general relativistic analogue of Newton's second law and generalizes the concept of a “straight line” to curved spacetime by describing the trajectories of bodies under the influence of a gravitational field. Related, the *geodesic deviation equation* describes

how nearby geodesics diverge or converge due to the intrinsic curvature of the manifold, quantified by the *separation vector* $S^\mu(\tau)$:

$$\frac{D^2 S^\mu}{D\tau^2} = R_{\alpha\beta\gamma}^\mu X^\alpha X^\beta S^\gamma ,$$

where, X^α is a vector field and $\frac{D}{D\tau} = X^\alpha \nabla_\alpha$ denotes the directional covariant derivative (see Definition 2). Thus, it encodes information about the tidal forces of gravitation.

F.0.1 Analytical (exact) solutions

Exact solutions of the EFEs are metric tensor fields $g_{\alpha\beta}$ that satisfy Equation (2). Many exact solutions are known, which can be classified into exterior (vacuum) solutions and interior solutions [17]. While there exist several geometries that satisfy the EFEs, we shall focus on three prominent vacuum solutions: the Schwarzschild metric, the Kerr metric, and gravitational waves. These geometries not only have a high theoretical and historical relevance, but are also of great interest in computational black hole astrophysics and gravitational wave and multi-messenger astronomy. Appendix C discusses these solutions in more detail, including other prominent coordinates, as well as real and fake (coordinate) singularities. From here on, we work in naturalized units by setting $c = G = 1$.

Schwarzschild metric It is the simplest non-trivial solution to the EFEs and describes a static spherically symmetric geometry around spherical non-rotating gravitating bodies, such as stars or black-holes. Although simple, the Schwarzschild metric predicts many phenomena beyond Newtonian gravity, most notably the precession of elliptical orbits and the bending of light rays. Both of these predictions have been experimentally verified in the Solar system, using the motion of Mercury perihelion and in the Eddington experiment during the 1919 Solar eclipse, respectively. The metric is typically written in spherical polar coordinates (t, r, θ, ϕ) where $t \in \mathbb{R}$, $r \in \mathbb{R}^+$, $\theta \in (0, \pi)$, and $\phi \in [0, 2\pi)$:

$$ds^2 = -\left(1 - \frac{2M}{r}\right)dt^2 + \left(1 - \frac{2M}{r}\right)^{-1}dr^2 + r^2(d\theta^2 + \sin^2\theta d\phi^2) .$$

Kerr metric generalizes the Schwarzschild solution to rotating bodies with the angular momentum J or, equivalently, the rotation parameter $a = \frac{J}{M}$. The solution forms a rotating, stationary (but not static) geometry, which is oblate around the rotation axis that breaks spherical symmetry. This geometry again permits new phenomena, notably the geodetic effect and frame dragging, both of which have been experimentally verified in the Earth's orbit by the Gravity Probe B.

The metric can be described in the corresponding *oblate spheroidal coordinates* also known as the *Boyer-Lidquist* (BL) coordinates (t, r, ϑ, ϕ) (see Equation (77)) [51]:

$$ds^2 = -\left(1 - \frac{2Mr}{\Sigma}\right)dt^2 - \frac{4Mr\sin^2\vartheta}{\Sigma}dtd\phi + \frac{\Sigma}{\Delta}dr^2 + \Sigma d\vartheta^2 + \left(r^2 + a^2 + \frac{2Mra^2\sin^2\vartheta}{\Sigma}\right)\sin^2\vartheta d\phi^2 .$$

Linearized gravity models the metric as tiny fluctuations or *perturbations* $h_{\alpha\beta}$, $|h_{\alpha\beta}| \ll 1$ of the flat background metric $\eta_{\alpha\beta}$:

$$g_{\alpha\beta} \approx \eta_{\alpha\beta} + h_{\alpha\beta} + \mathcal{O}(h_{\alpha\beta})^2 .$$

Famously, this model can describe GW propagation using a periodic time-dependent perturbation, which has served as the theoretical basis for the Nobel-prize winning detection of GWs generated by binary black hole mergers [3]. As detailed in Appendix C.3, the choice of a certain *gauge* essentially transforms the vacuum EFEs into the wave equation $\square \bar{h}_{\alpha\beta}^{(\epsilon)} = 0$ where $\square \equiv \eta^{\alpha\beta}\partial_\alpha\partial_\beta$ is the *d'Alembert* or *wave* operator and $\bar{h}_{\alpha\beta}^{(\epsilon)} = h_{\alpha\beta}^{(\epsilon)} - \frac{1}{2}h^{(\epsilon)}\eta_{\alpha\beta}$. This equation admits a family of GW solutions: we will use the plane wave propagating in the z -direction with the angular frequency ω expressed in the Cartesian coordinates:

$$h_{\alpha\beta}^{\text{TT}} = \begin{pmatrix} 0 & 0 & 0 & 0 \\ 0 & h_+ & h_\times & 0 \\ 0 & h_\times & h_+ & 0 \\ 0 & 0 & 0 & 0 \end{pmatrix} \cos(\omega(t - z)) .$$

Here, h_+ and h_\times are the amplitudes of the “+” (plus) polarization and “ \times ” (cross) polarization

G Experimental details

This appendix provides detailed experimental specifics, including: (i) revisiting the concept of Sobolev training and its application `EinFields` (ii) gradient alignment aspects relevant to SOAP optimizers; (iii) error plots for the metric and higher-rank differential geometric quantities, with component-wise tomography where applicable; (iv) training across varied coordinate systems to illustrate the coordinate-choice flexibility of NeFs; (v) the hyperparameter configurations employed; and (vi) the hardware and software environments used for these experiments.

G.1 Data

For our main set of experiments, we overfit `EinFields` against the analytic solutions introduced in Section F.0.1, each having different features and spatio-temporal symmetries:

- Schwarzschild metric in spherical coordinates (Equation (97)),
- Kerr metric in Boyer-Lindquist and Kerr-Schild coordinates (Equations (100, 80)),
- gravitational waves metric (TT gauge) in Cartesian coordinates (Equation (84)).

For each, we compute the distortion after subtracting the flat background metric using the corresponding equations summarized in the Appendix. Detailed information on data specifications is provided in Table 5.

Additionally, in Section ??, we train each geometry in different coordinate systems to investigate how the choice of coordinates impacts NeFs (recall: the physical laws do not depend on the coordinate system).

Metric	Coordinates	Domain	Resolution	Parameters
Schwarzschild	Spherical (t, r, θ, ϕ)	$t = 0$ $r \in [2.5, 150]$ $\theta \in (0, \pi)$ $\phi \in [0, 2\pi]$	1 128 128 128	$M = 1$
Kerr	Boyer- Lindquist (t, r, ϑ, ϕ)	$t = 0$ $r \in [3, 14]$ $\vartheta \in (0, \pi)$ $\phi \in [0, 2\pi]$	1 128 128 128	$M = 1$ $a \in [0.628, 0.95]$
	Kerr-Schild (t, x, y, z)	$t = 0$ $x \in [-3, 3]$ $y \in [-3, 3]$ $z \in [0.1, 3]$	1 128 128 128	$M = 1$ $a = 0.7$
Linearized gravity	Cartesian (t, x, y, z)	$t \in [0, 10]$ $x \in [0, 10]$ $y \in [0, 10]$ $z \in [0, 10]$	140 10 10 140	$\omega = 1$ $\epsilon = 10^{-6}$

Table 5: Training data generation specifications: spacetime metric, coordinate system, domain extent, grid resolution, and physical parameters.

G.2 Sobolev training

This refers to a class of learning paradigms where NNs are trained not only to match target function values but also additionally its derivatives [30]. Formally, given a target function $f : \mathcal{X} \rightarrow \mathbb{R}$, and a NN approximation \hat{f}_θ , Sobolev training minimizes a joint loss involving the functional and its derivatives:

$$\mathcal{L}_{\text{Sob}}(\theta) = \mathbb{E}_x \left[\lambda_0 \|f(x) - \hat{f}_\theta(x)\|^2 + \sum_{j=1}^N \lambda_j \left\| D^{(j)} f(x) - D^{(j)} \hat{f}_\theta(x) \right\|^2 \right], \quad (103)$$

where $D^{(j)}$ denotes the j^{th} derivative operator, which in our case could be the partial derivatives ∂^j or covariant derivatives ∇^j , and λ_j are weighting coefficients. This loss promotes alignment not only in function space but also in the Sobolev space $W^{N,2}(\mathcal{X})$, which encodes both value and derivative information. Sobolev training enhances generalization, stability, and accuracy of NeF derivatives [73].

Algorithm 1: EinField training

```

1: Input: Training dataset  $\{(x^i, g(x^i), \partial_x^{(1)} g(x^i), \partial_x^{(2)} g(x^i))\}_{i=1}^m$ , number of epochs  $N_{\text{epochs}}$ , learning rate  $\eta$ , optimizer  $\mathcal{O}$ , Sobolev order  $N \in \{0, 1, 2\}$ 
2: Initialize neural field parameters  $\theta$  on device  $\mathcal{D}$  (e.g., GPU) in single (FLOAT32) precision
3: for epoch = 1 to  $N_{\text{epochs}}$  do
4:   for each mini-batch  $(x_{\text{batch}}, g_{\text{batch}}, \partial_x^{(1)} g_{\text{batch}}, \partial_x^{(2)} g_{\text{batch}})$  in dataset do
5:     Move  $(x_{\text{batch}}, g_{\text{batch}})$  to device  $\mathcal{D}$ 
6:      $\hat{g}_{\text{batch}} \leftarrow \text{EinFields}(x_{\text{batch}}; \theta)$ 
7:     loss  $\leftarrow \mathcal{L}(g_{\text{batch}}, \hat{g}_{\text{batch}})$ 
8:     if  $N \geq 1$  then {Jacobian supervision}
9:       Compute  $\partial_x^{(1)} \hat{g}_{\text{batch}}$  through AD
10:      loss  $\leftarrow$  loss +  $\lambda_1 \cdot \mathcal{L}(\partial_x^{(1)} g_{\text{batch}}, \partial_x^{(1)} \hat{g}_{\text{batch}})$ 
11:    end if
12:    if  $N \geq 2$  then {Hessian supervision}
13:      Compute  $\partial_x^{(2)} \hat{g}_{\text{batch}}$  through AD
14:      loss  $\leftarrow$  loss +  $\lambda_2 \cdot \mathcal{L}(\partial_x^{(2)} g_{\text{batch}}, \partial_x^{(2)} \hat{g}_{\text{batch}})$ 
15:    end if
16:    Compute gradients:  $\partial_\theta \leftarrow \partial_\theta \text{loss}$ 
17:    Update parameters:  $\theta \leftarrow \mathcal{O}(\theta, \partial_\theta, \eta)$ 
18:    Optionally: synchronize gradients across devices if using distributed training
19:  end for
20:  Optionally: evaluate on validation set, log MAE and memory usage for monitoring
21:  Optionally: checkpoint  $\theta$  for fault tolerance and reproducibility
22: end for
23: return optimized parameters  $\theta$ 

```

The impact of the modified training loss is particularly evident when accurately querying higher-order differential geometric quantities, which include the metric Jacobian, Christoffel symbols, metric Hessian, Riemann tensor, and curvature invariants on an arbitrary set of validation points. We evaluate the improvement in reconstruction quality and fidelity for these quantities on the Kerr metric in Cartesian KS coordinates, which are free of coordinate singularities, using 2D tomographic slices (see Section G.6 for details). Comparative results with and without Sobolev training are explicitly reported in Figures ??–13.

G.3 Evaluation criteria

We flatten the ground truth tensor at point $p \in \mathcal{M}$ with its components indexed by k be denoted by $f_k(p) \in \mathbb{R}^n$, with $1 \leq k \leq n$ and the corresponding *EinFields* parametrized tensors are denoted by $\hat{f}_k(p)$. The dimensionality n depends on the tensor under consideration. For instance, for a symmetric metric tensor $n = 10$, corresponding to its independent components, while for the Riemann curvature tensor, $n = 256$ when considering all components explicitly, or $n = 20$ when accounting only for the independent components under the symmetries inherent to the tensor, respectively.

We evaluated these quantities over a set of $m \approx 125,000$ validation collocation points $\mathcal{D} = \{p_i\}_{1 \leq i \leq m}$ and use standard error criteria in discretized form, which includes double sums: one over the total number of tensor components $\{f_k\}_{1 \leq k \leq n}$, while the other for the total number of collocation points $\{p_i\}_{1 \leq i \leq m}$:

$$\text{Mean-absolute error (MAE)} = \frac{1}{mn} \sum_{i=1}^m \sum_{k=1}^n |\hat{f}_k(p_i) - f_k(p_i)| \quad (104a)$$

$$\text{Relative } \ell_2 \text{ error (Rel. } \ell_2) = \sqrt{\frac{\sum_{i=1}^m \sum_{k=1}^n |\hat{f}_k(p_i) - f_k(p_i)|^2}{\sum_{i=1}^m \sum_{k=1}^n |f_k(p_i)|^2}}. \quad (104b)$$

These are applied to the metric tenors and their derived quantities, illustrated in Figures 8 and 2. Recall that the tensor components are coordinate-dependent (and even more so, the metric Jacobian, metric Hessian, and Christoffel symbols are not even tensors), and, hence, these errors lack an immediate physical meaning. This is improved with the consideration of scalar quantities such as the Ricci scalar, Kretschmann invariants, and Weyl scalars, which by definition are coordinate-independent quantities.

The above error criteria are an aggregation of point-wise, i.e., local quantities. We additionally assess the quality of free-falling trajectories obtained by evolving the geodesic equation (Equation ??) from the same initial condition on the exact and approximate metrics. Even small errors quickly accumulate during the evolution of the trajectory, providing a sensitive assessment of the metric quality. In addition, these trajectories provide a strong physical intuition, e.g., the number of stable orbits.

G.4 Gradient alignment

Competing tasks is a well-known problem in multi-objective learning ([74], [75], [76]), the gradients of the loss functions pull the weights in different directions. In Scientific Machine Learning (SciML), a lot of work emerged in analyzing and mitigating gradient conflicts in the context of PINNs ([34], [77], [78]). Although Sobolev training differs from PINNs, particularly from a supervision perspective, it exhibits the same problem where some loss terms dominate others. In PINNs, the training is highly dependent on first satisfying the initial/boundary conditions, which provide uniqueness to the solution. The different levels of complexity between these and the residual loss create different optimization priorities, but both losses are equally important. Similarly, Sobolev training faces analogous challenges with competing loss components. The Jacobian data serve to constrain the model's derivatives, while the target function outputs determine the integration "constant", both components being equally valuable. However, the sources of complexity differ between these approaches. In PINNs, the primary challenge stems from determining a solution through unsupervised learning on PDE losses, whereas in our Sobolev training specifically, the complexity arises from managing optimization stability in high-dimensional spaces: a 16-dimensional output space, 64-dimensional Jacobian, and 256-dimensional Hessian. Moreover, this complexity is accompanied by the challenge of handling gradient imbalances. Depending on the point in spacetime, the metric or its derivatives dominate in the loss. Generally speaking, an analogy is to think $g_{\mu\nu} \propto \frac{1}{r}, \partial_\rho g_{\mu\nu} \propto \frac{1}{r^2}$ and $\partial_{\sigma\rho} g_{\mu\nu} \propto \frac{1}{r^3}$, making it clear how gradient magnitudes differ depending on the radius.

Mitigating gradient conflicts does not necessarily result in better accuracy, but it explains a possible reason why the loss does not improve further, the optimization being stuck in the local minimum of one of the objectives. The intra-step gradient alignment scores presented in [34] demonstrate SOAP as a far superior alternative compared to other well-established optimizers, or at least for the experiments considered in that study. To provide a direct comparison using the same methodology as in [34], we evaluated both ADAM and SOAP on the Cartesian KS representation of the Kerr metric, chosen as the most complex metric investigated in this work. The Sobolev training contains only two objectives: metric and Jacobian supervision. For our experimental setup, we employed an MLP architecture with 5 hidden layers, 190 hidden units per layer, and SILU activation function to compare gradient conflicts between the two optimizers. The training utilized a cosine decay learning rate schedule, starting from an initial learning rate of 1E-2 and decaying to a final rate of 1E-8 over 200 epochs. For weighting the losses, gradient normalization was used with and without an exponential moving average. As shown in Figure 15, even though Adam is providing twice as much gradient alignment score in almost all epochs, SOAP's second-order and preconditioning capabilities allow for a 100x training loss improvement.

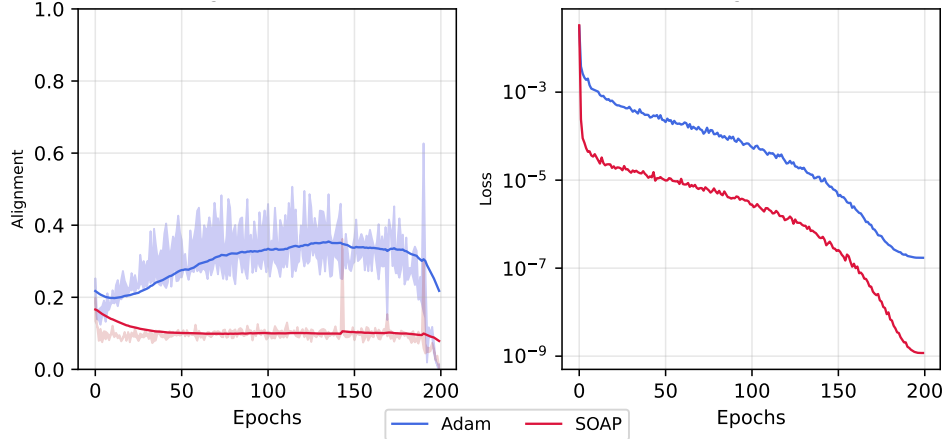


Figure 9: Average gradient alignment per epoch (left) and MSE loss during training for Adam and Soap optimizers (right). The shaded light color in the alignment plot represents a minimum and maximum deviation compared to using an exponential moving average or not for the weights multiplying the gradients.

G.5 Kerr metric error visualization

To quantify the quality of EinFields parametrized metric tensor fields for the Kerr metric with spin parameter $a = 0.7$ ⁹, we report the mean absolute error (MAE) between the ground truth and the NeF-fitted metric tensors in Figure 10. The evaluation is performed on a validation grid with collocation points sampled arbitrarily within the training range but distinct from the training collocation points. Using a model configured with SiLU activations, SOAP optimizer, GradNorm, and without Sobolev regularization, we observe agreement with the ground truth up to six decimal places, achieving an MAE on the order of 1E-6.

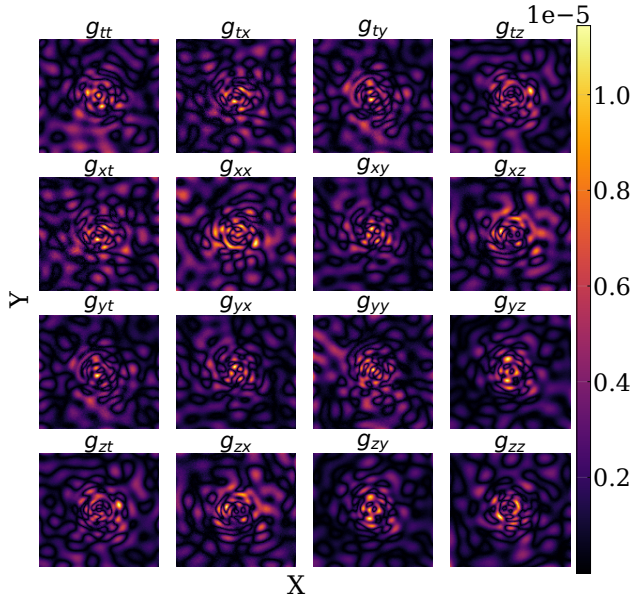


Figure 10: Kerr metric absolute error between ground truth (analytic) metric and the EinFields parametrized metric. The metrics are depicted in the Cartesian Kerr-Schild (KS) representation as presented in Equation (80). The 2D slice of all the metric components captured in the x-y plane at fixed $z = 1.4$ for a spin parameter value $a = 0.7$.

⁹Cartesian Kerr-Schild coordinates are chosen to avoid coordinate singularities, enabling tomography over larger coordinate ranges.

G.6 Tomography: Metric, metric Jacobian and metric Hessian components

The effect of introducing losses pertaining to metric Jacobian and Hessian supervision, apart from the metric loss that EinFields predominantly uses, can be quantified and visualized with the following plots below. Here, for the sake of visualization, we do a tomography (2D cuts) of different metric components along a particular axis for the Kerr metric in Cartesian KS coordinates (Equation (80)).

The first, second, and third columns in each figure correspond to EinFields training without Sobolev supervision, EinFields (+Jac), and EinFields (+Jac + Hess) trained, respectively, for randomly sampled components of differential geometric quantities.

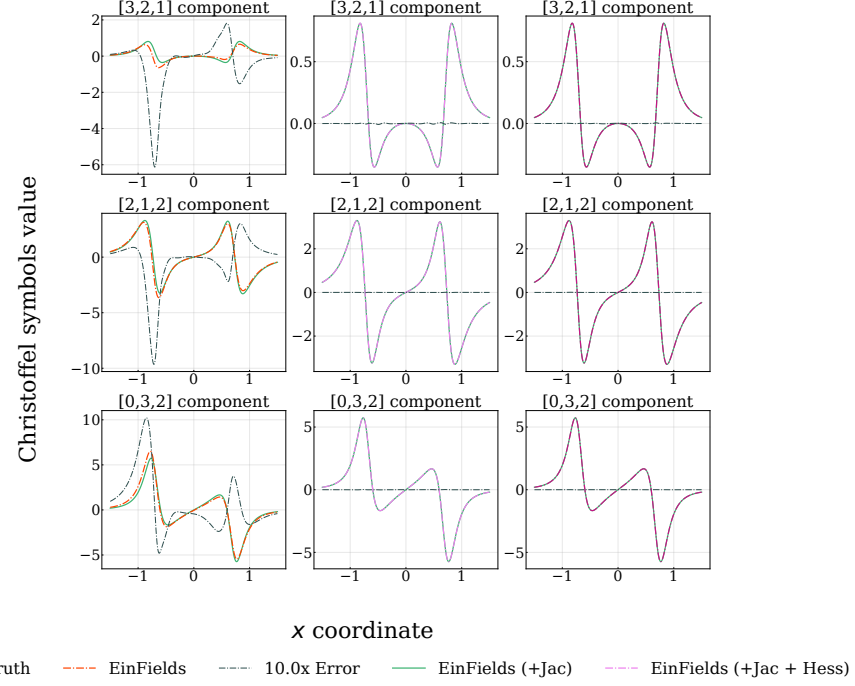


Figure 11: 2D Tomography of Kerr *Christoffel symbols* components in Cartesian KS representation.

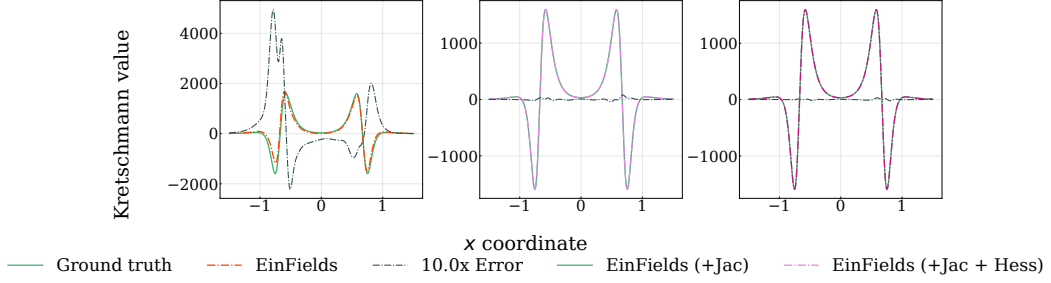


Figure 13: 2D Tomography of Kerr *Kretschmann invariant* in Cartesian KS representation.

G.7 Training on varied coordinate systems

NeFs take physical coordinates as inputs and map them directly to field values. Unlike traditional machine learning architectures that ingest abstract learned feature spaces (such as token embeddings or extracted features), INRs operate directly on the physical coordinate space, enabling them to represent continuous signals in a domain-agnostic manner.

In the context of GR, this implies that a four-dimensional representation of metric tensor fields by an INR explicitly depends on the input coordinate system, or more generally, on the chosen frame of reference. Despite this apparent dependency, GR possesses the fundamental property of diffeomorphism covariance (see Section B.4.1), which asserts that the laws of gravitation remain

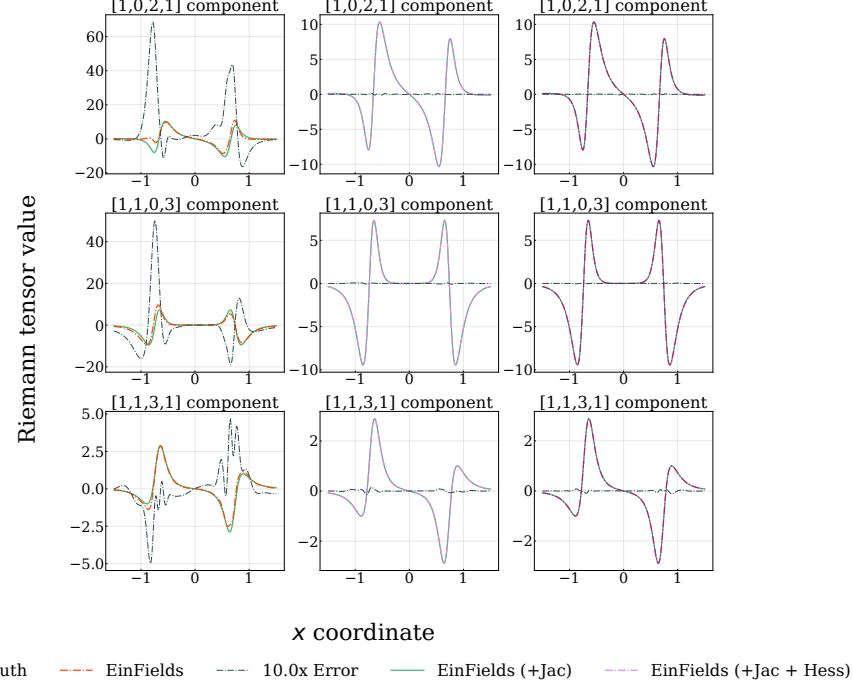


Figure 12: 2D Tomography of Kerr *Riemann tensor* components in Cartesian KS representation.

invariant under smooth coordinate transformations. However, the choice of coordinate system remains an essential practical tool for simplifying the form of the metric tensor. For example, while the Schwarzschild metric is diagonal in spherical coordinates (albeit with a coordinate singularity at the event horizon), transforming to Cartesian KS coordinates produces a dense, off-diagonal metric representation, or, for that matter, moving to Eddington-Finkelstein coordinates, which both remove coordinate-related artifacts (see Paragraph B.3.6).

Understanding this behavior is essential for developing robust INR-based frameworks for representing geometric quantities in numerical relativity, while respecting the underlying diffeomorphism invariance of general relativity.

For the Schwarzschild case, we initiate the training by sampling query spacetime coordinates in spherical representation (t, r, θ, ϕ) . These sampled collocation points are then transformed into their corresponding collocation points in Cartesian coordinates (t, x, y, z) and ingoing Eddington-Finkelstein coordinates $(v, r, \theta, \tilde{\phi})$ (see Section C.1.1 for explicit transformation details). Subsequently, EinFields outputs the metric tensors corresponding to these coordinate systems, yielding Equations ((69), (73), (76)).

For the Kerr metric, which is characterized by its oblate spheroidal geometry, we sample query collocation points in the Boyer-Lindquist coordinates (t, r, ϑ, ϕ) , followed by the collocation points transformed into Cartesian (t, x, y, z) and ingoing Eddington-Finkelstein coordinates $(t, r, \theta, \tilde{\phi})$. EinFields then outputs the Kerr metric tensors in these respective coordinate systems, resulting in Equations ((79), (80), (82)).

Metric	Spherical-like	Cartesian-like	Lightcone-like
Schwarzschild	✓	✓	✓
Kerr	✓	✓	✓

Table 6: Coordinate charts used for NeF training on Schwarzschild and Kerr metrics.

Metric	Representation	Coordinate	Rel. L2
Schwarzschild	EinFields	Spherical	2.26E-7
		Cartesian Kerr-Schild	1.37E-5
		Eddington-Finkelstein	9.21E-9
Schwarzschild	EinFields (+ Jac)	Spherical	1.37E-7
		Cartesian Kerr-Schild	3.00E-6
		Eddington-Finkelstein	6.47E-9
Schwarzschild	EinFields (+ Jac + Hess)	Spherical	1.20E-7
		Cartesian Kerr-Schild	1.53E-6
		Eddington-Finkelstein	9.08E-9
Kerr	EinFields	Boyer-Lindquist	6.95E-8
		Cartesian Kerr-Schild	4.47E-6
		Eddington-Finkelstein	6.44E-8
Kerr	EinFields (+ Jac)	Boyer-Lindquist	4.72E-8
		Cartesian Kerr-Schild	8.83E-7
		Eddington-Finkelstein	4.95E-8
Kerr	EinFields (+ Jac + Hess)	Boyer-Lindquist	4.69E-8
		Cartesian Kerr-Schild	4.95E-7
		Eddington-Finkelstein	4.72E-8

Table 7: Relative L2 error considered on a grid of validation collocation points (i) EinFields, (ii) EinFields (+Jac) and, (iii) EinFields (+Jac + Hess) supervision. As described above in the text, we quantify the effect of inputs queries in varied coordinate charts and how EinFields training generalizes over these different metric (geometry) representations.

This multi coordinate training strategy (shown in Figure (6) and the numbers recorded in Table (7)) ensures that the neural tensor field learns consistent representations across coordinate systems while maintaining geometric and physical consistency under diffeomorphisms, facilitating generalization and stability in downstream geometric learning tasks.

G.7.1 Schwarzschild metric

Geodesics in the Schwarzschild spacetime are of fundamental interest, as they underlie phenomena such as gravitational lensing and the perihelion precession of Mercury, as well as the motion of planets in the solar system more generally.

The initial conditions of the trajectories chosen in the experiments are fully specified by the *initial position*

$$(t, r, \theta, \phi)(t = 0) = (0, a_0 r_s, \pi/2, 0) \quad (105)$$

and the *initial four-velocity*

$$(v^t, v^r, v^\theta, v^\phi)(t = 0) = \left(\frac{1}{\sqrt{(1 - r_s/r_0)(1 - v_0^2)}}, 0, 0, v_0 \frac{\cos \phi_0}{\sqrt{r_0^2(1 - v_0^2)}} \right), \quad (106)$$

Where $v_0 = b_0 \sqrt{1/(r_0 - r_s)}$ and $a_0, b_0 \in \mathbb{R}$ can be chosen freely to select the desired orbit in the $\theta = \pi/2$ plane. The geodesics in Figure 14 demonstrate a good qualitative agreement over several orbits. The error is quantified and discussed further in Section G.8.

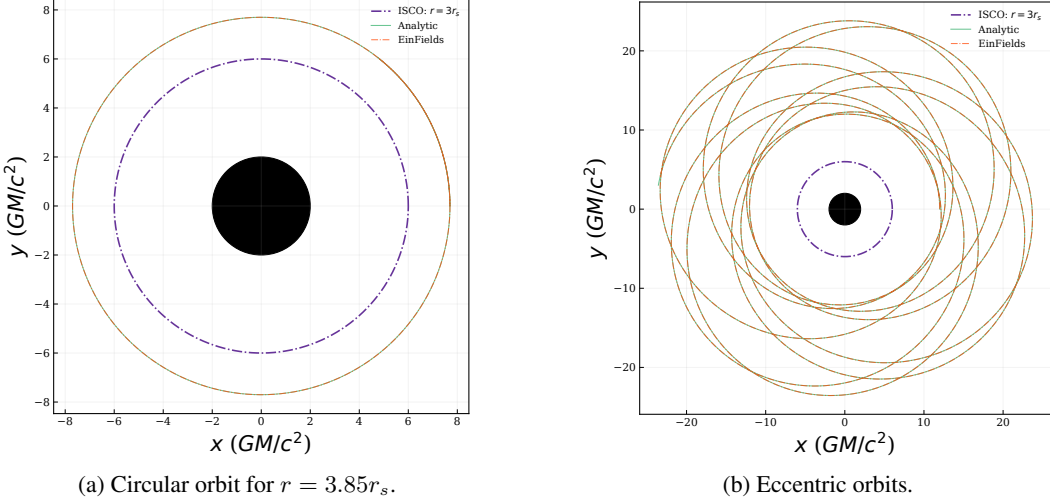


Figure 14: Geodesics in Schwarzschild spacetime simulated in spherical coordinates (Equation (69)). The filled black circle indicates $r \leq r_s = 2M$. The purple dashed line marks the innermost stable circular orbit (ISCO) at $r = 3r_s$. Green solid lines represent the ground-truth geodesics, while the red dotted lines represent EinFields reconstructed ones. We find very close agreement between the orbits up to a chosen time of running the geodesics.

Being able to compute geodesics is sufficient to perform rendering. We use the Schwarzschild EinFields metric to render a black-hole on a celestial background. This requires propagating geodesics from the camera observer via the spacetime terminating at the distant background. The resulting image in Figure 15 provides visual evidence for the global consistency and quality of the metric and the derived Christoffel symbols.

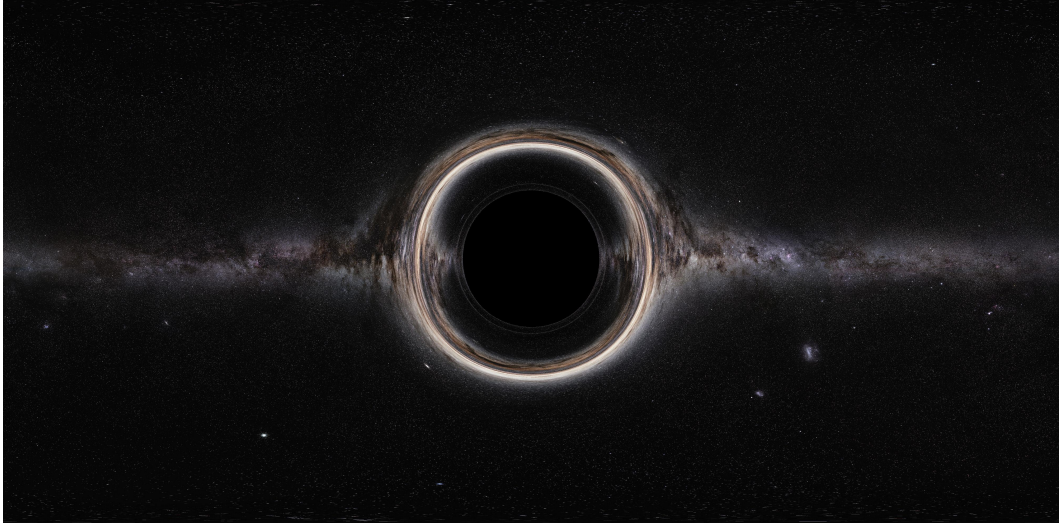


Figure 15: Render of a Schwarzschild black-hole in front of a celestial background constructed from the EinField metric.

G.7.2 Kerr metric

Geodesics in a Kerr spacetime around a rotating body (see details in Appendix C.2) play a central role in several key astrophysical observations and experimental tests of GR. Notably, photon geodesics determine the black hole shadow images captured by the Event Horizon Telescope [79], and frame-dragging (Lense-Thirring) effects [17] are a hallmark of the Kerr geometry. These have been measured experimentally by the Gravity Probe B mission [80] and recently via radio pulses arriving from pulsars [81]. Here we also show the capacity of our model to reproduce prograde orbits (stable geodesics with smaller radii), and arbitrary eccentric orbits, which depend on the initial conditions,

including choice of energy E and angular momentum L_z of the test particle. The geodesics in Figure 16 demonstrate a good qualitative agreement over several orbits.

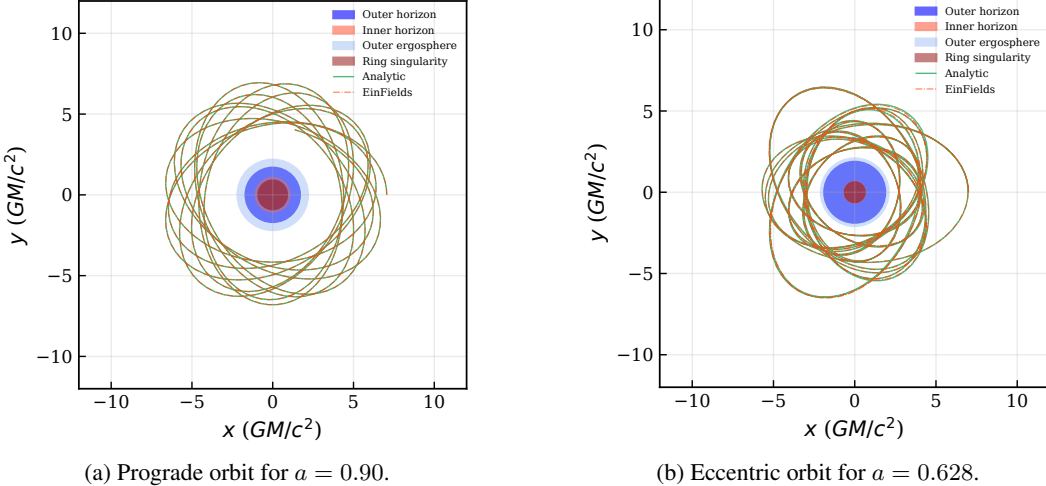


Figure 16: Geodesics in Kerr spacetime simulated in Boyer–Lindquist coordinates (Equation (79)). Distinct regions of the geometry are indicated in solid colors. Green solid lines represent ground truth geodesics, while red dotted lines represent our NeFs reconstructed orbits.

Kretschmann invariant. The Kretschmann invariant (scalar), $\mathcal{K} = R^{\alpha\beta\gamma\delta}(x^\mu)R_{\alpha\beta\gamma\delta}(x^\mu)$, is a key curvature invariant distinguishing true (curvature) singularities from coordinate (apparent) singularities (see Appendix B.3.6). For the Kerr geometry, the rotation parameter a induces a ring singularity at radius a on the equatorial plane $\theta = \pi/2$, where the curvature diverges (see Equation (83) and Section C.2.2). Accurately capturing this geometric structure requires isolating true singularities from coordinate artifacts, which can otherwise lead to incorrect classification of singularities.

We perform training in Cartesian KS coordinates (see Equation (80)) to eliminate coordinate singularities that would otherwise impede convergence. We first train EinFields (+Jac + Hess) on Cartesian KS coordinates, subsequently constructing the Riemann tensor (see Section B.3.6) via successive automatic differentiation steps and raising indices using the parametrized metric \hat{g} (see Equation (83)). The NeF reconstructed \mathcal{K} captures the ring singularity structure and agrees well with the analytical solution, as shown in Figures 17a and 17b. However, the reconstruction remains sensitive to floating-point errors and requires high NeF accuracy for stability (see Limitations, Section ??).

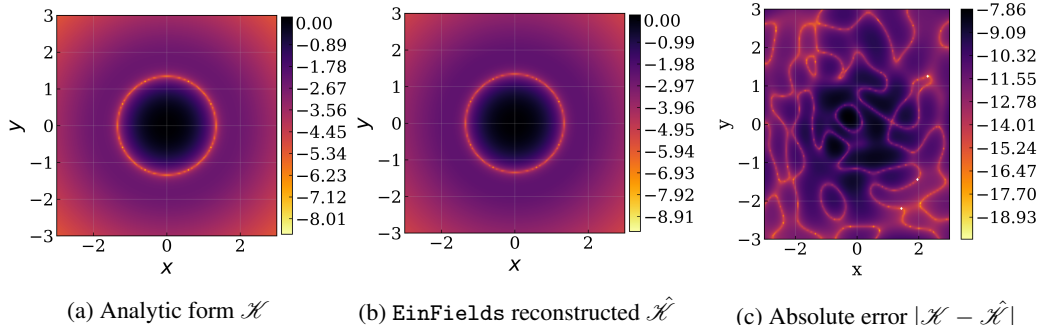


Figure 17: The Kretschmann scalar \mathcal{K} of the Kerr metric computed in Cartesian Kerr-Schild form (Equation (80)) in the x - y plane for $z = 0.3$.

G.8 Accumulation of rollout errors for geodesics

Minute floating-point inaccuracies (around 1E-5 to 1E-6) arising from Christoffel symbols retrieved via EinFields autoregressively accumulate when evolving the equations of motion for test particles along geodesics.

To quantify the inaccuracies between the ground truth and NeF-evolved geodesics, we compute the deviation between the position vectors $r(\tau) \in \mathbb{R}^3$ as a function of the affine parameter (proper time) τ in Cartesian coordinates. Specifically, for the ground truth trajectory, the spatial coordinates corresponding to the position vector are given by $r(\tau) = (x(\tau), y(\tau), z(\tau))$, while for the NeF-evolved trajectory, we denote $\hat{r}(\tau) = (\hat{x}(\tau), \hat{y}(\tau), \hat{z}(\tau))$. The deviation at each proper time τ is then computed as the Euclidean norm,

$$\delta r(\tau) = \|r(\tau) - \hat{r}(\tau)\|_2 = \sqrt{(x(\tau) - \hat{x}(\tau))^2 + (y(\tau) - \hat{y}(\tau))^2 + (z(\tau) - \hat{z}(\tau))^2}. \quad (107)$$

In practice, the geodesic trajectories are computed in (r, ϑ, ϕ) (e.g., Boyer–Lindquist) coordinates and subsequently transformed into Cartesian coordinates before evaluating the deviation using the above expression.

Given the high sensitivity of time-stepped trajectories to such numerical inaccuracies, we quantify this error accumulation by explicitly presenting the deviation as a function of the affine parameter τ , especially for *eccentric orbits* for both Schwarzschild (see Figure 14b) and Kerr metric for $a = 0.628$ (see Figure 16b). These are reported for the Schwarzschild use case in Figure 18a, and Figure 18b for the Kerr metric use case, respectively. For Schwarzschild, the error accumulates stably, while for Kerr it is erratic. We hypothesize this is likely due to the stable versus chaotic nature of orbits in the respective spacetimes. Eventually, orbits diverge significantly, especially when leaving the NeF training domain.

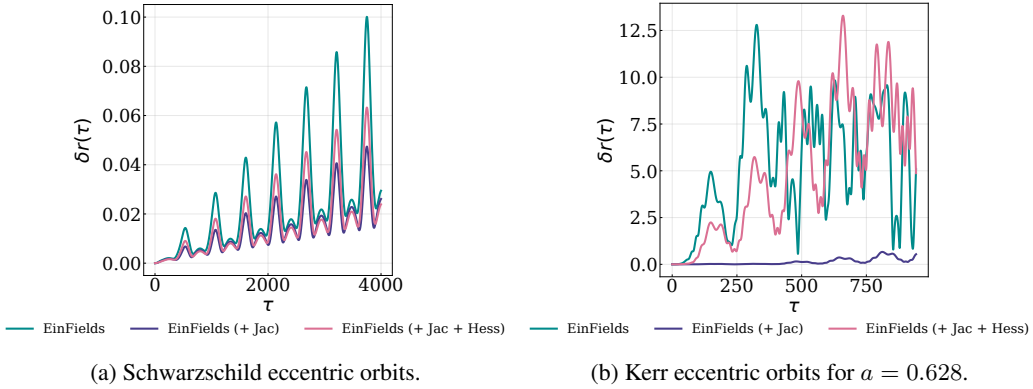


Figure 18: Geodesic rollout deviation δr over proper time τ .

The results suggest that incorporating the Hessian supervision into training may introduce noise that can hinder convergence, performing worse than using metric Jacobian supervision or, for that matter, metric alone. For geodesic equations, supervising second derivatives is often unnecessary, and Jacobians alone provide significant improvements in trajectory reconstruction. However, Hessians become essential when computing Riemann tensors and curvature-related quantities, and are required in applications such as numerically solving the geodesic deviation equation (see Equation (??)), which are typically encountered for solving for the test ring oscillation in linearized gravity use cases.

G.9 Validation problems for GW metric and derivatives quality.

Compared to Schwarzschild and Kerr metrics, a key distinction of the linearized gravity setting describing gravitational waves is its time dependence (see Equation (84)). Although it does not depend on x and y , the temporal dependence motivates us to consider our model trained on a full spacetime grid of size $N_t \times N_x \times N_y \times N_z$.

Distortion of ring of test-particles. When the described gravitational wave interacts with a ring of freely falling test particles initially at rest in the x - y plane, it induces periodic deformations of the ring. For a purely $+$ polarized wave, the resulting motion causes the ring to stretch and squeeze along the x - and y -axes, leading to a characteristic “plus” deformation pattern.

The motion of the test particles under the influence of this gravitational wave is obtained by solving the geodesic deviation equation, up to leading order in the strain amplitude h_+ . As a result, the particle trajectories in the TT gauge are

$$x(t) = \left(1 + \frac{1}{2}h_+ \cos(\omega(t-z))\right)x(0), \quad y(t) = \left(1 - \frac{1}{2}h_+ \cos(\omega(t-z))\right)y(0). \quad (108)$$

Here, $x(0)$ and $y(0)$ denote the initial coordinates of a test particle, and the time-dependent perturbations reflect the tidal nature of gravitational waves. The cosine dependence captures the periodic stretching and squeezing of spacetime caused by the wave as it traverses the particle ring. Figure 4c and Table 8 show how the famous ring oscillation experiment can be reproduced with EinFields. This is done by parametrizing the perturbation $h_{\alpha\beta}^{\text{TT}}$ and captures the famous *stretching and squeezing* effect.

Weyl scalars of gravitational radiation field. The *Weyl scalars* are five complex quantities $\Psi_0, \Psi_1, \Psi_2, \Psi_3, \Psi_4$ that arise in the *Newman–Penrose* formalism of GR [54]. They encode all the independent components of the Weyl tensor $C_{\alpha\beta\gamma\delta}$ (see Equation (62)), representing the “free” gravitational field – the part of spacetime curvature that can propagate as gravitational waves, distinct from the curvature directly caused by matter. In NR and GW modeling, $\Psi_4(t)$ is the primary scalar quantity used to extract observable GW signals from simulations. It is defined as

$$\Psi_4 := C_{\alpha\beta\gamma\delta} n^\alpha \bar{k}^\beta n^\gamma \bar{k}^\delta \quad (109)$$

with n, k being a particular choice of **Newman–Penrose** (NP) tetrads and \bar{k} its complex conjugate¹⁰. The central relation in an asymptotically flat spacetime (cf. Boyle et al. [82] for details) is that $\Psi_4(t)$ is equivalent to the second coordinate-time derivative of the strain $h(t) = h_+(t) + i h_\times(t)$:

$$\Psi_4 \equiv -\ddot{h}_+ + i \ddot{h}_\times. \quad (110)$$

We compute Ψ_4 from the NeF-parameterized strain $h_{\alpha\beta}$ in two distinct ways:

1. *indirectly* via the Weyl tensor obtained with the differential-geometric chain (see also Figures 8 and 2): $h_{\alpha\beta}^{\text{TT}} \xrightarrow{+\eta_{\alpha\beta}} g_{\alpha\beta} \xrightarrow{\partial} \Gamma_{\alpha\beta}^\gamma \xrightarrow{\nabla} R_{\alpha\beta\gamma}^\delta \xrightarrow{\text{Eq. (109)}} \Psi_4$;
2. *directly* via the second time-derivative: $h_{\alpha\beta}^{\text{TT}} \xrightarrow{\text{Eq. (110)}} \Psi_4$.

Spin-weighted spherical harmonic representation for GW extraction. A quantity of central interest in gravitational waveform construction is the *mode decomposition* of the GW strain into its angular components. The complex strain $h(t, r, \theta, \phi) \equiv h_+(t, r, \theta, \phi) - i h_\times(t, r, \theta, \phi)$ can be expanded in terms of *spin-weighted spherical harmonics* (SWSHs) as

$$h(t, r, \theta, \phi) = \frac{M}{r} \sum_{\ell=2}^{\infty} \sum_{m=-\ell}^{\ell} h^{\ell, m}(t) {}_{-2}Y_{\ell m}(\theta, \phi), \quad (111)$$

where ${}_{-2}Y_{\ell m}(\theta, \phi)$ are the SWSHs (see Equation (89)) with spin-weight $s = -2$ reflecting the helicity of GWs in the TT gauge (see Equations (87) and (88)). In practice, the dominant contributions to the strain arise from the quadrupole ($\ell = 2, m = \pm 2$) modes, denoted by $h^{2, \pm 2}(t)$, which capture the leading-order gravitational radiation (detailed in Section C.3). Figure 19

¹⁰Note that the Weyl scalars are not invariant and depend on a particular choice of the tetrad fields.

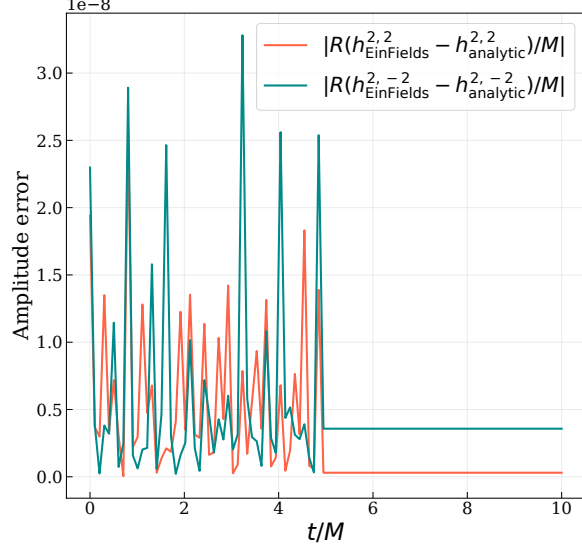


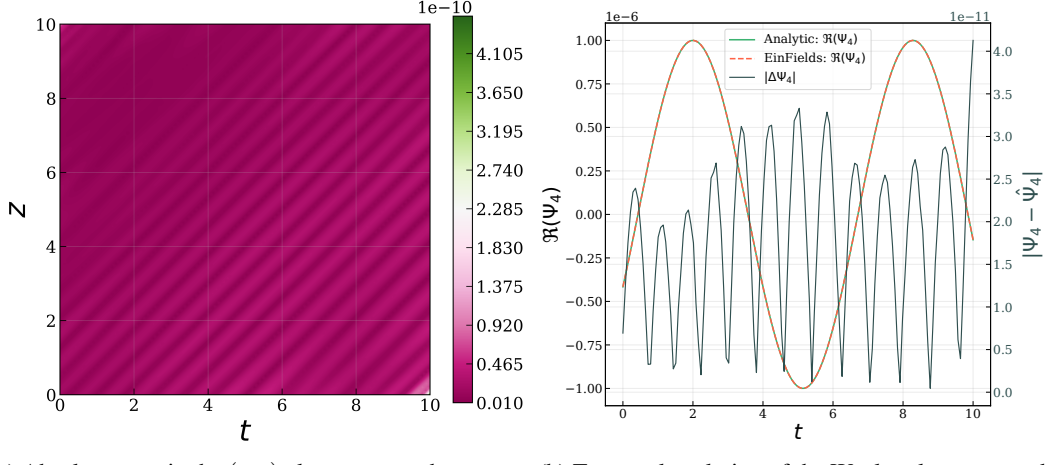
Figure 19: The absolute error of the amplitude between the EinFields and analytic values $|R/Mh^{2,\pm 2}(t)|$ (see Equation (88)) at a fixed radial distance $R = 1$ plotted against t/M . The amplitudes agree to $1E-8$, indicating that EinFields can capture the complex strain h and subsequently $h^{2,\pm 2}(t)$ GW signals.

Radiated power of GWs. Another important physical observable for GWs is the radiated power loss given by the famous *quadrupole* formula [41]. The time-averaged power or *luminosity* radiated by GWs is given by

$$\frac{dE}{dt} = \frac{r^2}{32\pi} \int d\Omega \langle \dot{h}_{ij}^{TT} \dot{h}^{TT\ ij} \rangle = \frac{1}{4} \langle \dot{h}_+^2 + \dot{h}_\times^2 \rangle. \quad (112)$$

The particular perturbation metric in the above experiments (see Equation (84)) has equal amplitude $A = h_+ = h_\times$ for both $+$ and \times polarizations. As a consequence, the radiated power loss simplifies to

$$\frac{dE}{dt} = \frac{\omega^2 A^2}{4}. \quad (113)$$



(a) Absolute error in the (z, t) plane, averaged over $x-y$ slices.
(b) Temporal evolution of the Weyl scalar computed from the analytic and EinFields perturbations (left axis) and their absolute error (right axis) at a fixed position.

Figure 20: Comparison of the real part of the Weyl scalar $\Re(\Psi_4)$ (Equation (109)) computed from the EinFields and the analytic metric. The errors are on the order of E-10 and E-11, respectively, indicating highly accurate gravitational waveform reconstruction capacities of EinFields. Refer to Table 8 for more details.

For GW tasks, we also compare against two other relevant models, which utilize periodic activations functions: (i) WIRE architecture [83] with a continuous real Gabor wavelet activation function $\psi(x; \zeta_0, s_0) = \cos(\zeta_0 x) e^{-(s_0 x)^2}$, with ζ_0 and s_0 controlling the frequency of the wavelet and the spread, respectively (i.e., signal width localized in both the spatial and frequency domains), and (ii) SIREN [58] architecture with the periodic activation function $\sin(\zeta_0 x)$, and ζ_0 being the modulating frequency.

The SiLU activation function exhibits a lower frequency bias and lacks oscillatory behavior in its higher-order derivatives, which directly feature in the Sobolev norms used during training. In contrast, sinusoidal activations employed in SIREN and WIRE architectures inherently possess oscillatory behavior, with their k -th derivatives scaling as ζ_0^k , where ζ_0 denotes the base frequency. This scaling amplifies high-frequency components and can lead to instability when minimizing Sobolev norms, as high-frequency errors become disproportionately emphasized. In practice, the smoothness and non-oscillatory nature of SiLU activations result in more stable training and improved generalization under Sobolev training objectives. These trends are quantitatively reflected in our experiments, as reported in Table 8.

Model	$h_{\alpha\beta}^{TT}$ (+Jac + Hess) (GradNorm)	Ricci scalar R	Weyl scalar $\Re(\Psi_4)$	Luminosity dE/dt
SiLU	8.56E-4	5.90E-13	2.53E-5	2.71E-4
SIREN	3.78E-2	1.08E-12	9.56E-5	3.34E-4
WIRE	1.68E-2	1.55E-13	1.81E-5	3.69E-4

Table 8: Rel. ℓ_2 for key quantities in the linearized gravity case with two different NeF architectures: (i) perturbation metric, (ii) perturbation metric trained with Sobolev loss and gradient normalization, (iii) reconstructed Ricci scalar, and (iv) reconstructed real part of the Weyl scalar Ψ_4 , where $\Psi_4 \propto \ddot{h}_+(t, \mathbf{x})$. The final column reports the absolute difference in the predicted gravitational radiation energy loss, integrated over the unit sphere.

G.10 Training hyperparameters

Table 9: Training configurations for Schwarzschild, Kerr, and GWs used in the geodesics, Kretschmann plots, Table 8, and linearized gravity section.

Parameter	Schwarzschild	Kerr	GWs
Architecture	MLP		
Depth	3 / 3 / 5 / 7	5	5
Width	64 / 128 / 256 / 512	190	128 / 128 / 90
Activation	SiLU	SiLU	SiLU / SIREN / WIRE
Input dimension	4	4	4
Output dimension	10 / 16	16	16
# Parameters	13.5K / 50K / 332K / 1.5M	185K	85K
Optimizer	SOAP		
β_1	0.95		
β_2	0.95		
Precondition frequency	1		
Learning rate schedule			
Initial learning rate	E-2 / E-3		
Decay steps	10^4	$6 \times 10^3 / 2, 4, 6 \times 10^4$	$4 \times 10^3 / 4 \times 10^4$
Final learning rate	E-5 / E-6	E-7 / E-8	E-9
Training			
Epochs	100	200	200
Number of batches	100	30 / 100 / 200 / 300	20 / 200
Gradient weighting scheme	None / GradNorm		

G.11 Hardware

For our primary computational work, we utilize a high-performance CPU system equipped with 2x32-core Intel® Xeon® Platinum 8452Y+ processors, each operating at 4.1 GHz, and 2048 GiB of RAM. All NeF-related training is performed on a single NVIDIA H200 SXM GPU with 144 GiB of HBM3e memory. For prototyping and preliminary experiments, we employ a single NVIDIA Tesla A100 GPU with 40 GiB of memory.